

# **Experimental Studies of High-pressure Gasoline Fuel Sprays for Advanced Internal Combustion Engines**

by

Mario Medina

A dissertation submitted in partial fulfillment  
of the requirements for the degree of  
Doctor of Philosophy  
(Mechanical Engineering)  
in the University of Michigan  
2020

Doctoral Committee:

Professor Margaret Wooldridge, Chair  
Professor Andre Boehman  
Assistant Professor Jesse Capecelatro  
Associate Professor Herek Clack  
Associate Professor Mirko Gamba

Mario Medina

[marmed@umich.edu](mailto:marmed@umich.edu)

ORCID iD: [0000-0003-4439-8324](https://orcid.org/0000-0003-4439-8324)

© Mario Medina 2020

## Acknowledgements

I would like to take a moment to express my gratitude to a community of people who helped make this body of work possible with their continuous support, guidance, and love.

First, I want to offer my appreciation to Margaret Wooldridge for welcoming me into her research group. Margaret has been fundamental towards furthering my success as a scholar. She gave me the liberty and creative freedom to pursue my own research interests. With her encouragement and guidance, I was able to create a positive impact in the scientific community, the UM community, and elsewhere.

I also want to thank my dissertation committee, Prof. Andre Boehman, Prof. Jesse, Capecelatro, Prof. Herek Clack, and Prof. Mirko Gamba. Collectively, all these individuals provided insightful discussion both in and outside of the classroom. Their thoughtful feedback and suggestions helped shape the contents of this dissertation.

I am also extremely thankful to my colleagues, mentors, and friends at Bosch. First, I want to acknowledge Dr. Mohammad Fatouraie for being a part of my journey from the start. He helped recruit me into the Ph.D. program and served a significant role in my research direction. The contents of this thesis stem from constant collaborations with Mohammad. Nonetheless, I also had the opportunity to conduct research as a graduate intern at the Bosch facilities. During the research internship, Dr. Kevin Peterson and Dr. Fahad Alzahrani were instrumental to my research. Their collaboration and discussions led to a scientific contribution that formed part of my doctoral studies. I also want to thank Shraavan Ravindranath for his contribution to our discussion circles. Additionally, I want to acknowledge the generous financial and technical support from Bosch throughout the years.

Furthermore, I would like to recognize my colleagues and friends at Centro Motores Termicos at the Universitat Politecnica de Valencia for their experimental and technical support. Prof. Raul Payri was open and supportive to my research proposal to utilize their state-of-art facilities. Their expertise on fuels sprays were essential to the making of this thesis. I want to recognize Prof. Jaime Gimeno, Maria Martinez, Dr. Alberto Viera, Abian Bautista, Jesus Peraza,

Armando Moreno, Cesar Carvallo, Tomas Montiel, Vincenzo Pagano, Santiago Cardona, Lucas Gonzalez, Mario Belmar, Enrique, and Marco for welcoming me into their group. My gratitude extends to the lab technicians Jose Enrique del Rey and Omar Huerta for their flexibility and knowledge to conduct my experiments.

There is a long list of mentors who have taught me valuable skills and how to think critically. I want to highlight, Prof. Martin Morris, who gave me my first research project, inspiring my natural curiosity, and persuaded me to attend graduate school. I have also been very fortunate to befriend Dr. Mauro Rodriguez, Dr. Hector Perez, and Dr. Orlando Trejo who are role models and have challenged me to become a better version of myself.

I also want to thank the staff and faculty within the College of Engineering at the University of Michigan. Many individuals have helped me along the way with their wisdom, constant support, and guidance. I want to thank Prof. Kevin Pipe, Prof. Susan Montgomery, Prof. Neil Dasgupta, Rachel Casanova, Tiffany Porties, Bryan Enochs, Matthew New, Davon Wheeler, Nick Cantu, and Johnathan Klozik.

To all my friends from Chicago, to Ann Arbor, to Valencia, and everyone else I've met along the way, thank you. There are too many of people to thank individually and I'm sure to miss a few but I will say that I have enjoyed your support and our friendship. Our conversations and interactions provided new perspectives, encouragement, and a community of genuine people. I want to recognize my current and past lab mates: Luis Gutierrez, Rachel Schwind, Ripudaman Singh, Miles Burnett, Cesar Botet, Andrew Mansfield, Dimitris Assanis, Shannon Clancy, Silvia Meng, John Kim, Qingyu Li, Elizabeth Bernhardt, Paola Rioja, and Yichen Zhou.

The last group of people I want to express my eternal gratitude is my family. To my parents who's seemingly never-ending sacrifice and love have motivated me to go beyond the limits. To my siblings, Nazario, Oscar, Nataly, and Carolina, for our abnormal sibling treatment and love that have helped me grow more than they know. To all my primas, primos, tias, tios, and abuelos who probably have no clue about the contents of my work, you are my inspiration.

## Table of Contents

Acknowledgements.....	ii
List of Tables .....	iii
List of Figures.....	iv
List of Appendices .....	xiv
Abstract.....	xv
Chapter 1 Introduction .....	1
Chapter 2 High Speed Imaging Studies of Gasoline Sprays under Non-Evaporative conditions	18
Chapter 3 The Effects of Injector Geometry and Operating Conditions on Spray Mass, Momentum and Development at Evaporative and Non-evaporative Conditions .....	48
Chapter 4 Mechanisms of Fuel Injector Tip Wetting and Tip Drying Based on Experimental Measurements of Engine-Out Particulate Emissions from Gasoline Direct Injection Engines....	73
Chapter 5 Conclusions and Future Outlook.....	105
Appendix 1 Supplemental Material for Non-evaporative Study of High-pressure Sprays .....	111
Appendix 2 Supplemental Material for Particulate Emissions Study.....	115

## **List of Tables**

Table 2.1. Summary of Experimental Conditions .....	20
Table 2.2. Summary of Fuel Properties .....	21
Table 2.3. Injector Orifice Information.....	23
Table 2.4. Summary of Camera Conditions.....	23
Table 2.5. Effects of nozzle internal features on spray development .....	34
Table 3.1 Fuel Properties .....	49
Table 3.2. Summary of Experimental Conditions .....	50
Table 3.3 Summary of camera settings used with the schlieren flow reactor imaging .....	53
Table 4.1: General features of the engines used in the study.....	81
Table 4.2: Category and range of engine operating parameters studied.....	82
Table 4.3: Injector parameters used in the experimental study .....	83
Table 4.4. Summary of the effects of the different operating conditions and fuel injector tip characteristics on engine-out PN emissions.....	96

## List of Figures

Figure 1.1. Effect of injection pressure on particle size distribution for DISI engine at 2000 rpm and mid-load operation [38].....	5
Figure 1.2. Schematics of the (a) general fuel flow leading to injector tip wetting in DISI engines, and (b) the basic internal features of DISI nozzle design [48]. .....	6
Figure 2.1. Top view schematic of experimental setup for diffuse backlit shadowgraph high-speed imaging including constant volume chamber, light source, camera, and injection system	21
Figure 2.2. Schematic of the nozzle orifice configuration of injector B and C. ....	22
Figure 2.3. Greyscale spray image overlaid with the binary spray contour (red), the spray angle reference lines (blue), the one-third maximum penetration length (green circles), and the maximum penetration length (black asterisk). The image represents an injection event for 600 bar injection pressure and 20 bar chamber pressure. The spray angle shown is $12.7^\circ$ and the maximum penetration length is 37.9mm.....	24
Figure 2.4 (a) Average penetration distance, and (b) average penetration rate at 1500 bar injection pressure for different chamber pressures. The spray break-up time is the time of maximum penetration rate. The error bars are the standard deviation of 20 experiments.....	26
Figure 2.5. (a) Average penetration distance, and (b) average penetration rate for 20 bar chamber pressure for different fuel injection pressures. The spray break-up time is the time of maximum penetration rate. The error bars are the standard deviation of 20 experiments.....	27

Figure 2.6. Comparison of all average spray break-up times. The error bars represent the standard deviation of the average of 20 experiments.....	27
Figure 2.7. (a) Average penetration distance and (b) average penetration rate at 20 bar chamber pressure for Injector B Hole 1.....	28
Figure 2.8. (a) Average penetration distance and (b) average penetration rate at 1500 bar injection pressure for Injector B Hole 1.....	29
Figure 2.9. (a) Chamber pressure effects on average spray angle at 1500 bar injection pressure. (b) Injection pressure effects on average spray angle at 20 bar chamber pressures. For both panels, the error bars indicate one standard deviation of the average of 20 experiments.....	29
Figure 2.10. Average spray angle for Injector B Hole 1 for (a) a fixed chamber pressure of 20 bar and (b) fixed injection pressure of 1500 bar. ....	30
Figure 2.11. Comparison of spray development results of Injector A Hole 1 and Injector B Hole 1 at 1200 bar injection pressure and 20 bar chamber pressure. (a) average penetration distance (b) average penetration rate (c) average spray angle.....	32
Figure 2.12. Comparison of spray development at 1500 bar injection pressure and 20 bar chamber pressure as a function of nozzle size where the diameter of Injector B Hole 1 is $\frac{1}{2}$ that of Injector B Hole 2 (a) average penetration distance (b) average penetration rate (c) average spray angle.....	33
Figure 2.13. Comparison of spray development metrics between both holes in injector C for 1500 bar injection pressure and 20 bar chamber pressure (a) average penetration distance, (b) average penetration rate, and (c) average spray angle.....	34



Figure 2.14. Series of greyscale images for a chamber pressure of 20 bar and injection pressure of 600 bar showing (a) anomalous spray images, (b) typical spray images with continuous spray development and red contours, and (c) anomalous images with red contours superimposed .....	36
Figure 2.15. Series of greyscale images for a chamber pressure of 20 bar and injection pressure of 1500 bar showing (a) anomalous spray images, (b) typical spray images with continuous spray development and red contours, and (c) anomalous images with red contours superimposed .....	36
Figure 2.16. Frequency of occurrence of the vapor pre-jets for the conditions investigated in the study.....	37
Figure 2.17. Series of greyscale near nozzle images for 300 bar fuel injection pressure and chamber pressure of 20 bar. ....	38
Figure 2.18. Comparison of single cycle spray angle data with cycle averaged data for Injector C Hole 1 and Injector C Hole 2 .....	40
Figure 2.19. Mean-squared difference in spray angle for all the cycles of 1500 bar injection pressure and 1 bar chamber pressure for (a) Injector C and (b) Injector B .....	40
Figure 2.20. Image sequence of spray development from Injector C Hole 1 (right column) and Injector C Hole 2 (left column) for 1500 bar injection pressure and 1 bar chamber pressure. The red circles highlight observable changes in the size and symmetry of the spray angle from Hole 2.....	41
Figure 3.1. Schematic of injection rate meter including the main components [4] .....	50
Figure 3.2. (a) Side cut plane of the momentum rate meter vessel with color-coded parts. Jets are shown in blue. The injector is shown in green. The sensor impingement surface is shown in red, and the sensor fixture is shown in yellow. (b) A conceptual schematic of the spray momentum measurement principle [8]. ....	51

Figure 3.3. Schematic for the high temperature high pressure test chamber including the gas flow equipment, the heating and cooling system, and the control system [5] .....	52
Figure 3.4. Schematic of the single-pass schlieren optical setup applied to the high-temperature, high-pressure flow reactor imaging studies. The green arrows indicate the light path. Adapted from Payri et al. [14]. .....	53
Figure 3.5. Results for average injection rate for 1500 bar injection pressure and 30 bar back pressure for Injector 2. The data include the mass from both nozzle holes of the injector. The shading represents the total mass per injection event. Vertical dashed lines indicate the region of the ROI data used to determine the hydraulic coefficients for the injector. ....	54
Figure 3.6. Average corrected momentum flux measurement for 1500 bar injection pressure and 10 bar chamber pressure. Vertical dashed lines indicate stabilized region.....	54
Figure 3.7. Schlieren image processing steps for Injector C for an injection pressure of 1500 bar and a chamber density of $8.44 \text{ kg/m}^3$ (corresponding to a chamber temperature of 800 K and a chamber pressure of 20 bar). (a) original image at time step i (b) masking applied to isolate hole 1 (c) summation of images at time step i and i-1 used for background subtraction (d) resulting image from background subtraction at time step i (e) temporal derivative of ith frame, using frames at i -1, and i -2, (e) final image after background subtraction using the two algorithms and conversion from gray scale to binary image. ....	55
Figure 3.8. Average fuel injection rate for two coolant temperatures for Injector C Holes 1 and 2 at 1500 bar injection pressure and 20 bar chamber pressure .....	57
Figure 3.9. Average injection rate for Injector C at $20^\circ \text{C}$ coolant temperature at 1500 bar injection pressure for three chamber pressures .....	58

Figure 3.10. Average injection rate for Injector C at 20° C coolant temperature at 30 bar chamber pressure for four injection pressures .....	59
Figure 3.11. Average mass flux for both injectors. All operating conditions are shown at 90° C coolant temperature.....	60
Figure 3.12. Average momentum flux measurements for Injector C Hole 2 at 90° C coolant temperature at injection pressure of 1200 bar for four chamber pressures.....	60
Figure 3.13. Average momentum flux measurements for Injector C Hole 2 at 90° C coolant temperature at 5 bar chamber pressure for four injection pressures .....	61
Figure 3.14. Average momentum flux for all four orifices. All operating conditions are shown at 90° C coolant temperature. ....	62
Figure 3.15. Momentum coefficient results for the four orifices of Injectors B and C at 90° C coolant temperature as a function of Reynolds number.....	63
Figure 3.16. Momentum coefficient results for the four orifices of (a) Injector B and (b) Injector C at 90° C coolant temperature as a function of cavitation number .....	64
Figure 3.17. Results for spray development for Injector B Hole 2 at 800 K chamber temperature, 30 bar chamber pressure (density 12.63 kg/m <sup>3</sup> ) and 90° C coolant temperature. (a) average penetration distance (b) average penetration rate and (c) average spray angle .....	65
Figure 3.18. (a) Average penetration distance and (b) average spray angle for Injector B Hole 1 at 1500 bar injection pressure and 90° C coolant temperature for 12 chamber density conditions. ....	66
Figure 3.19. Average penetration distance for Injector C Hole 2 at 600 bar injection pressure and 90° C coolant temperature for 12 chamber density conditions.....	67

Figure 3.20. Average penetration distance for all nozzles at 1500 bar injection pressure tested in CPF (top row) and at UM CVC (bottom row). (a) 600 K chamber temperature and 10 bar chamber pressure, density of 5.62 kg/m<sup>3</sup> (b) 600 K chamber temperature and 20 bar chamber pressure, density of 11.2 kg/m<sup>3</sup> (c) 300 K chamber temperature and 5 bar chamber pressure, density of 5.65 kg./m<sup>3</sup> (d) 300 K chamber temperature and 10 bar chamber pressure, density of 11.33 kg/m<sup>3</sup> ..... 68

Figure 4.1 Schematics of the (a) general fuel flow leading to injector tip wetting in GDI engines, and (b) the basic internal features of GDI injector nozzle design. [17] ..... 74

Figure 4.2: Schematic of the wide-plume tip-wetting process caused by fuel impingement on the edge of the pre-hole. Wider plumes ( $\alpha_{large}$ ) lead to increased wetting compared with narrower plumes ( $\alpha_{small}$ ). [17] ..... 78

Figure 4.3: Schematic of the vortex-droplet tip-wetting process where droplets that escape from the shear layer of the fuel spray in the low-pressure zone near the nozzle exit can be deposited on the injector tip. [17]..... 79

Figure 4.4: Schematic of the fuel-dribble tip-wetting process that occurs due to low-momentum, large-size droplets and ligaments depositing on the tip at the end of the fuel injection event. [17] ..... 80

Figure 4.5: Schematic of the tip drying mechanisms based on single-phase evaporation which is a function of the liquid and gas phase fuel pressures ( $p_{v,L}$  and  $p_{v,g}$ , respectively) and the fluid, wall and film temperatures ( $T_g$ ,  $T_w$  and  $T_L$ , respectively) and forced convection which is a function of the local fluid velocity  $u_g$ . [17]..... 81

Figure 4.6: Location of the tip temperature sensor in the instrumented GDI injector tip (Injector J in Table 3) [17] ..... 84

Figure 4.7: Timeline of engine test procedure .....	85
Figure 4.8: Repeatability of PN measurement for (a) the warmup procedure, and (b) the first five hours of the coking procedure, performed using Engine 3 and Injector J for coolant temperature of 90 °C, injection pressure of 200 bar, BMEP of 10 bar and engine speed of 2000 RPM.....	86
Figure 4.9: Typical particulate number (PN) results as a function of load (BMEP) and start of injection (SOI [CAD bTDC]) for Engine 1 (see Table 1) injector B, engine speed of 2000 RPM, fuel rail pressure of 200 bar and coolant temperature of 90 °C .....	87
Figure 4.10: PN measurements for injector L and engine 2 as a function of load and injection timing for $T_c = 90\text{ °C}$ , $p_f = 200\text{ bar}$ and engine speeds of (a) 1000 RPM (b) 2000 RPM and (c) 3000 RPM for Engine 2. The error bars represent 20% error from the mean. ....	88
Figure 4.11: Tip temperature and PN emissions as a function of engine load for Engine 3 and Injector J for (a) 1000 RPM, (b) 2000 RPM and (c) 3000 RPM, and a coolant temperature of 90°C, $p_f = 200\text{ bar}$ , and $SOI = 290\text{ CAD bTDC}$ .....	89
Figure 4.12: Injection pressure effects on PN for Injector L, Engine 2, coolant temperature of 90°C, and engine speed of (a) 1000 RPM (b) 2000 RPM and (c) 3000 RPM. PN results are for a fixed SOI in the tip wetting dominant regime of 260 CAD bTDC.....	90
Figure 4.13: Effect of engine speed and SOI timing on PN emission for Engine 1 for fixed $T_c = 90\text{ °C}$ and $p_f = 200\text{ bar}$ and (a) Injector L and (b) Injector D at $BMEP = 10\text{ bar}$ tested. Time is the absolute time from the end of injection to the time of spark. So, for fixed injection duration and spark timing, shorter times correspond to later SOI and longer times correspond to earlier SOI .....	91

Figure 4.14: Tip temperature and PN emissions as a function of engine speed for Engine 3 and Injector J at and $T_c = 90\text{ }^\circ\text{C}$ , $p_f = 200\text{ bar}$ , and $\text{SOI} = 290\text{ CAD bTDC}$ for (a) $\text{BMEP} = 2\text{ bar}$ and (b) $\text{BMEP} = 6\text{ bar}$ .....	92
Figure 4.15: Coolant temperature effects on PN for Engine 2 and Injector L for an engine speed of 2000 RPM, $\text{SOI} = 260\text{ CAD bTDC}$ , and (a) $p_f = 100\text{ bar}$ and (b) $p_f = 300\text{ bar}$ .....	92
Figure 4.16: Tip temperature and PN emissions as a function of engine-out coolant temperature for Engine 3 and Injector J for 1000 RPM, $\text{BMEP} = 4\text{ bar}$ , $p_f = 200\text{ bar}$ , and $\text{SOI} = 290\text{ CAD bTDC}$ .....	93
Figure 4.17: Effects of hole length on PN at 2000 RPM, 200 bar injection pressure, SOI timing of 260 CAD bTDC for the same engine architecture. (a) Effects are shown for injectors E (blue squares) and F (red circles) with varying hole length (b) Effects are shown injectors G (red circles) and H (blue squares) with varying hole length .....	94
Figure 4.18: Effects of hole conicity on PN at 2000 RPM, 200 bar injection pressure, SOI timing of 260 CAD bTDC for two engine architectures. (a) Effects are shown for injectors B (blue squares) and C (red circles) with varying hole conicity in Engine 1. (b) Effects are shown for injectors I (blue squares) and J (red circles) with varying hole conicity in Engine 3. The negative sign indicates converging nozzle data and the positive sign indicates diverging nozzle data. ....	95
Figure 4.19: Effects of pre-hole bore diameter size on PN at 2000 RPM, 200 bar injection pressure, SOI timing of 260 CAD bTDC for Engine 1 using injectors A (red circles) and D (blue squares) .....	96
Figure A1. (a) Average penetration distance, and (b) average cone angle for 300 bar injection pressure for different chamber pressures.....	111

Figure A2. (a) Average penetration distance, and (b) average cone angle for 900 bar injection pressure for different chamber pressures.....	111
Figure A3. (a) Average penetration distance, and (b) average cone angle for 1200 bar injection pressure for different chamber pressures.....	112
Figure A4. (a) Average penetration distance, and (b) average cone angle for 1 bar chamber pressure for different fuel injection pressures.....	112
Figure A5. (a) Average penetration distance, and (b) average cone angle for 5 bar chamber pressure for different fuel injection pressures.....	112
Figure A6. (a) Average penetration distance, and (b) average cone angle for 10 bar chamber pressure for different fuel injection pressures.....	113
Figure A7. Average spray angle for Injector B hole 1 for fixed injection pressure of (a) 600 bar and (b) 900 bar.....	113
Figure A8. Average spray angle for Injector B hole 2 for fixed injection pressure of (a) 600 bar and (b) 900 bar.....	113
Figure A9. Average spray angle for Injector C hole 1 for fixed injection pressure of (a) 600 bar and (b) 900 bar.....	114
Figure A10. Average spray angle for Injector C hole 2 for fixed injection pressure of (a) 600 bar and (b) 900 bar.....	114
Figure A11. Effect of engine speed and SOI timing on PN emission for Engine 1 for fixed $T_c = 90$ oC and $p_f = 200$ bar and five load conditions for (a) Injector I, (b) Injector J, (c) Injector A, (d) Injector B and (e) Injector C. Time is the absolute time from the end of injection to the time of spark. So, for fixed injection duration and spark timing, shorter times correspond to later SOI and longer times correspond to earlier SOI.....	115

Figure A12. Injection pressure effects on PN for Injector L, Engine 2, coolant temperature of 40 oC, and engine speed of (a) 1000 RPM (b) 2000 RPM and (c) 3000 RPM. PN results are for a fixed SOI in the tip wetting dominant regime of 260 CAD bTDC.....116



## **List of Appendices**

Appendix 1: Supplemental Material for Non-evaporative Study of High-pressure Sprays.....	111
Appendix 2: Supplemental Material for Particulate Emission Study.....	115

## Abstract

While much has been learned about gasoline direct injection sprays, there are still large gaps in the fundamental knowledge of the effects of high-pressure (over 500 bar) on gasoline sprays and on the role of fuel spray/nozzle interactions on particulate emissions. Particulate emissions are a critical concern for direct fuel injection spark-ignited engines, as future regulations may be difficult to meet without after-treatment. The objective of this dissertation was to quantitatively and qualitatively characterize fuel spray development for gasoline under engine-relevant conditions using non-intrusive optical techniques including high fuel injection pressures and canonical studies of the effects of internal flow structures on external spray development. Two experimental facilities were used to study high-pressure gasoline spray development and one experimental facility was used to study injector tip wetting and the effects on engine-out particulate emissions. Experiments were conducted at the University of Michigan with a constant volume chamber and diffuse backlit shadowgraph imaging for a range of chamber pressures (1 – 20 bar), injection pressures (300 – 1500 bar), and for several canonical fuel injector nozzle geometries including different nozzle exit diameters, converging and diverging nozzles, and rounded and abrupt inlet nozzles. The images were used to measure penetration distance and rate and spray angle as a function of time for each injection event, which are compared with results of previous experimental studies and simplified physics-based models that have been proposed in the literature. Trends in fuel spray development were similar to those observed previously for diesel sprays, which was unexpected given the significant differences in thermal-physical properties. Some abnormal spray features were identified and quantified, including spray flutter (i.e., asymmetric variation in spray angle). Injector internal flow characterization and spray development measurements were also performed at Centro Motores Termicos, an engine research division at the Universitat Politecnica de Valencia (UPV). Rate of injection, and momentum flux, were measured using two facilities and spray development was imaged using schlieren in another facility for a range of chamber pressures (5 – 30 bar), and injection pressures (600 – 1500 bar), and included vaporizing and non-vaporizing

chamber temperatures of 400 – 800 K. The work revealed the important effect of internal flow transitions on injector performance, where nozzles with inlet rounding resulted in 20% higher mass flow rate compared with straight cylindrical nozzles. Spray momentum coefficients showed a negative trend with increased pressure differential indicating all nozzles were cavitating under all conditions tested. Lastly, trends in measured engine-out particulate number (PN) emissions were correlated as a function of a large array of fuel injectors, multiple engine architectures, and a large parametric space of operating conditions. PN was measured directly from sampling engine-out exhaust using a laser-scattering condensation particle counting system. The tests were specifically identified as conditions where fuel injector tip wetting is considered a significant source of PN. Five conceptual mechanisms were developed to describe the tip wetting and drying processes and to interpret the effects of fuel injection pressure, engine load, time scales, injector temperature, and injector geometry on PN. Overall, the data provide a better understanding of the effects of operating and hardware parameters on the development of gasoline fuel sprays and on particulate number emissions. The results directly inform strategies for novel combustion concepts, current engine architectures, and fundamental spray theory.

# Chapter 1

## Introduction

### 1.1 Background

From 2017 to 2018, the world consumption of total energy increased by 2.9% or 13.8 billion tonnes oil equivalent [1]. Conservative estimates predict a 36% increase in global energy consumption between 2018 to 2050; from 610 to 830 quadrillion British Thermal Units (qBTU) [2]. Efforts are continuously being made to improve our existing energy infrastructure as well as create new sustainable technologies to meet the global needs. Although renewable energy sources are growing quickly, combustion provides more than 80% of the global supply [2]. Research shows the persistence of combustion systems in our society for at least the next five decades [1–3].

More than a quarter of the energy that is generated in the U.S. is used for the transportation of people and goods. This is a significant portion of energy needed to power our vehicles, planes, ships, and trains domestically. In the transportation sector, 92% of the energy consumption in 2015 was from petroleum-based fuels [4] and a large portion of that energy is used for light-duty passenger vehicles (LDVs). The market demand for LDVs provides significant motivation to improve energy consumption, particularly given the “leaky pipeline” of energy losses for LDVs. For example, a gasoline mid-size vehicle only utilizes between 12-30% of the fuel energy to actually move the vehicle [5–7]. There is huge potential and impact for fuel economy improvements, thermal efficiency benefits, and emissions reduction in LDVs.

An additional topic of key interest to the engine development community are methods to reduce vehicle emissions. Engines produce criteria pollutants, (where the initial criteria air pollutants were established by the Clean Air Act) and greenhouses gases that lead to poor air quality [8] and climate change [9]. Realizing even a small percentage of fuel economy improvement can reduce CO<sub>2</sub> emissions by significant amounts from the transportation sector [10,11]. Car manufacturers are continuously working towards increasing the fuel economy of

their production fleet while reducing the associated combustion emissions. In particular, particulate emissions generated during the combustion process are concerns in two of the major engine architectures today; namely compression and spark-ignition engines. Particulate emissions cause poor air quality, reduce visibility, and can lead to many health concerns [12–14]. Recent regulations require particulate emissions below a specified limit, and both of the major engine architectures are expected to be challenged to meet future regulations without expensive after-treatment technology that also reduces fuel economy. For example, studies have shown that direct injection spark ignited (DISI) gasoline vehicles may not meet the new particulate mass standard of 3 mg/mi in the U.S [15,16] or the particulate number standard of  $6 \times 10^{11}$  particles/km in Europe [17,18] without aftertreatment.

The two specific engine technologies that motivate this thesis work are: (1) gasoline compression ignition (GCI) as a low temperature combustion strategy and (2) higher injection pressures for reduced particulate emissions in DISI engines. Both technologies require direct fuel injection into the combustion chamber as a critical component of the combustion processes. There are many advantages of direct injection, including improved fuel metering and evaporative cooling effects, which can improve engine power density and reduce criteria air pollutant emissions. Direct injection allows precise amounts of fuel delivery compared with port fuel injection [19]. Additionally, direct injection can provide a specific distribution of fuel that is often required to enable advanced combustion strategies. Evaporative cooling effects allow higher compression ratios and higher boosting (i.e., turbocharging) ratios, which can lead to more efficient engines. Direct injection has been shown to provide many overall improvements to engine performance, with one major disadvantage; the increased output of particulate emissions. In the following sections, the advantages of these technologies are discussed in further detail, including identifying the critical uncertainties of fuel injection processes relevant to these technologies.

## **1.2 Gasoline Compression Ignition**

Advanced combustion strategies are combustion strategies that develop higher efficiency and cleaner burning engines. Examples of these strategies include down-sized (i.e., physically smaller) and boosted engines, low-temperature combustion, lean-burn gasoline combustion, clean diesel combustion, and variable compression ratio engines, to name a few. Many of these

strategies have the potential to realize up to 20-40% fuel economy improvements and eliminate the need for exhaust aftertreatment [20–24]. Low-temperature combustion (LTC) is flameless with fuel oxidation that occurs at relatively low temperatures compared with conventional engines. The process typically requires excess amounts of air or exhaust gas recirculation (EGR) to create a dilute mixture. The mixture is allowed to auto ignite via compression of the fuel, air and diluent gases. Low-temperature combustion has been and continues to be a topic of research for the engine community because of the fuel economy and emissions improvements it can offer. Examples of LTC include homogenous charge compression ignition (HCCI), reactivity-controlled compression ignition (RCCI), and premixed-charge compression ignition (PCCI).

HCCI is considered a hybrid between spark-ignited and compression ignition combustion. However, decades of research have shown that while HCCI can achieve thermal efficiency benefits at some load and speed conditions, HCCI is also hard to control, offers limited engine load operation, produces high hydrocarbon and carbon monoxide emissions, and can lead to potentially catastrophic in-cylinder pressures and acoustic noise [25–28]. Research has led to advances in combustion strategies that can overcome the limitations of HCCI and some other LTC operating strategies. One example is a hybrid between HCCI and DI combustion concepts. This combustion concept is described by several names in the literature such as partial-premixed combustion and gasoline compression ignition (GCI). During GCI combustion, high-pressure gasoline is directly injected into the combustion chamber with excess air and moderate to high levels of EGR. The properties of the fuel/air mixture provide long ignition delay times, which allow more time for the fuel to mix with the surrounding air. Studies have shown that GCI can achieve 40% thermal efficiency with lower particulate and NO<sub>x</sub> emissions compared with a conventional compression ignition engine [22,29–31]. Consequently, the GCI technology is attractive from efficiency and emissions standpoints.

GCI engine development has dramatically advanced using both computational and experimental tools; however, many aspects of the combustion design remain largely empirical, including spray processes such as the liquid break-up, droplet formation, and fuel/surface interactions (e.g., impingement), and fuel injector tip wetting and drying. The fundamental understanding of high-pressure diesel sprays has also advanced considerably in the past two decades; however, the fuel properties of gasoline and diesel are very different. Two important examples are the differences in fuel lubricity and volatility. The lubricity of gasoline is lower

than diesel and the operation at high-pressure is more easily achieved using diesel without risk of damaging system components. Gasoline is more volatile than diesel, and this dramatically effects the injection process, atomization and evaporation. Additionally, the high volatility has implications with respect to cavitation specifically for pump operation and nozzle flow. Cavitation is the process by which a liquid evaporates during large decreases in pressure, causing bubbles to form and subsequently implode. Cavitation can cause material damage, poor combustion efficiency and increased emissions [32].

### **1.3 Direct Injection Spark Ignited Gasoline**

The second engine technology that motivates studies of high-pressure gasoline spray development is the DISI engine architecture. DISI engine technology (widely commercialized around 2007) captured 49% of the market share within nine years of introduction [4]. Direct injection offers several benefits over the previous standard of port fuel injection. Fuel economy and thermal efficiency are increased through precise fuel metering and higher compression ratios, respectively. However, the main drawbacks from using direct injection are the decreased mixing times allowed and potential fuel impingement on combustion surfaces. Both drawbacks contribute to higher levels of particulate emissions generated with DISI engines. Regarding the decreased mixing times, studies have shown that increased injection pressure can increase air entrainment from higher fuel spray velocities and higher shear forces and create smaller droplets - providing conditions for faster mixing [33–35]. The trend of better mixing with higher fuel injection pressure is consistent regardless of fuel composition [36,37]. For example, Eitel et al. showed that increasing the injection pressure from the nominal value of 200 bar to 500 bar decreased the mean droplet size by 40% [38] with computational fluid dynamics (CFD) simulations of gasoline and a DISI injector. Moreover, the authors verified that particulate emissions decreased by increasing injection pressure when tested in a DISI engine at mid-load operation. The results are shown in Figure 1.1. The CFD simulations performed by Eitel et al. [38] were limited to using an average droplet size and evaporated mass of the spray and did not include any details of spray development, fuel films on injector nozzles, or simulations of particulate emissions. CFD simulations require well-defined spray properties and processes (e.g., accurate models for atomization, evaporation, mixing, tip wetting, wall wetting, cylinder motion, combustion and soot formation) to yield accurate predictions for emissions, even to capture

qualitative trends. Such simulations are costly and time consuming and include a large number of empirical fits to the spray processes, which increase uncertainty in the results. In comparison, experiments to understand key mechanisms effecting spray processes can often be conducted quickly over a broad range of operating conditions, and the outcomes can directly improve engine design and performance and inform computational models.

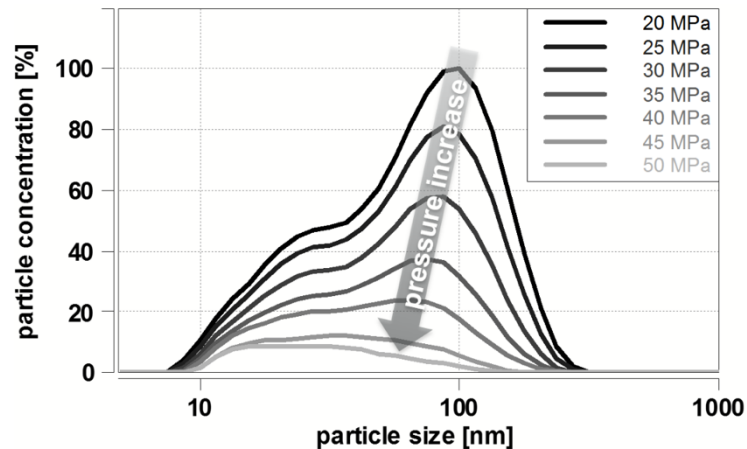


Figure 1.1. Effect of injection pressure on particle size distribution for DISI engine at 2000 rpm and mid-load operation [38]

A drawback from direct injection is the potential for fuel impingement on combustion surfaces. Fuel impingement is a phenomenon by which fuel is deposited onto a surface creating a liquid film of fuel. The films can become significant sources of particulate mass (PM) and particulate number (PN) emissions from DISI engines. There are several mechanisms that are the source of particulate emissions, including fuel impingement on the piston crown, intake and exhaust valves, and cylinder walls [39–43]. Operating strategies [44–46] and design criteria [39,47] can help reduce or eliminate wetted surfaces. However, one surface wetting mechanism that cannot be avoided by injection strategy and is not well understood is injector tip wetting. Injector tip wetting occurs when the fuel injection event creates liquid-phase fuel films or droplets on the tip of the fuel injector. Figure 1.2 shows schematics of the fuel flow leading to tip wetting in a DISI injector nozzle.



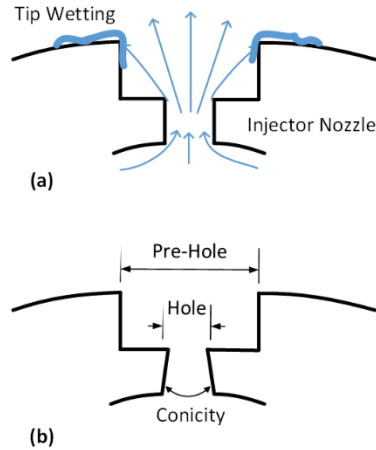


Figure 1.2. Schematics of the (a) general fuel flow leading to injector tip wetting in DISI engines, and (b) the basic internal features of DISI nozzle design [48].

Injector tip wetting and tip drying have important effects on particulate emissions from DISI engines, and at some conditions, combustion of fuel on the injector tip has been shown to be a significant source of particulates [38,39,49–52]. For example, Berndorfer et al. [50] used in-cylinder imaging to identify and quantify luminescence from diffusion flames originating from the fuel injector tip of a large-bore single-cylinder DISI engine. The large bore was used to reduce the effects of wall and piston wetting by the fuel spray and focus on injector diffusion flames. The injector diffusion flame imaging data were quantified and compared with experimental measurements of engine-out PM and PN. The diffusion flame results correlated well with the particulate measurements, leading the authors to conclude that combustion of fuel on the injector tip was the dominant source of particulate emissions, whereas combustion of the bulk charge was not. In some respects, tip wetting can be considered the lower bound for PM and PN emissions from DISI emissions. This dissertation work includes original applied and fundamental studies to identify conditions (both operational and hardware) affecting tip wetting.

#### 1.4 High-pressure Gasoline Fuel Sprays

Fuel spray research has advanced dramatically over the past three decades with respect to diesel sprays. Particularly, our understanding of diesel combustion [53], predictions of diesel fuel spray characteristics with semi-empirical correlations [54–56] and effects of operating conditions and injector geometry on diesel fuel spray behavior such as droplet distribution, Sauter Mean Diameter, cavitation, liquid length, cycle-to-cycle variability, apparent heat release, etc. [34,57–

61]. However, few previous studies have considered high fuel injection pressures (specifically injections pressures higher than 500 bar) for gasoline, and fewer have considered the early times of the spray development (i.e., transition between momentum and diffusion flow). The state of knowledge of high-pressure gasoline fuel sprays is summarized here. In the study by Kim et al. [62], the authors compared diesel and gasoline fuel spray development at fuel injection pressures between 400 and 1000 bar at 2 bar chamber pressure in a constant volume chamber (CVC). The CVC results showed gasoline yielded a shorter liquid penetration length compared with diesel fuel, but the gasoline sprays produced larger spray cone angles. Kim et al. [62] also performed engine studies using an optically accessible single cylinder engine and qualitatively compared the spray development of the two fuels at injection pressures of 400 and 600 bar. The engine results showed that under evaporating conditions the penetration of gasoline was significantly lower than for diesel. Both fuels yielded comparable peak indicated mean effective pressure, but gasoline combustion resulted in lower NO<sub>x</sub> emissions.

Unlike the study by Kim et al. [62], Payri et al. [63] concluded the penetration distances of diesel and gasoline were similar at the operating conditions studied. Payri et al proposed the mixing processes for diesel and gasoline at non-evaporative conditions were the same based on the similar penetration distance and momentum flux measurements for both fuels.

Tian et al. [64] derived a semi-empirical correlation for the penetration distance of high-pressure gasoline sprays based on their experimental study of p-xylene sprays in a CVC at non-evaporating conditions (300 K) and evaporating conditions (500-760 K). Tian et al. [64] compared spray penetration data at injection pressures between 200 and 1200 bar at a chamber pressure of 1 bar (for non-evaporative conditions) and 10 to 40 bar (for evaporative conditions). The correlation for penetration distance as a function of time used parameters found in previous diesel spray correlations, including the difference between the fuel injection pressure and the chamber pressure, nozzle outlet diameter, fuel density, and ambient (i.e., chamber) density, and the authors included ambient temperature as a means to include vaporization effects. Importantly, the correlation by Tian et al. [64] did not propose a spray break-up time, which has been widely used for diesel spray correlations. The correlation was compared with experimental results for high-pressure gasoline sprays in the study by Tian et al. [64] and both other research groups, including work by Medina et al. [65]. The comparisons showed significant discrepancies

at all times, which is expected due to the lack of a transition in spray development at the spray break-up time.

A recent study by Yamaguchi et al. [37] performed spray studies using n-heptane and various nozzle geometries at pressures up to 1500 bar. The authors found divergent nozzles produced shorter penetration than convergent nozzles. Using droplet size measurements, they also concluded increased injection pressure yields smaller droplets with the most pronounced decrease at injection pressures of 800 bar. However, n-heptane is a single component fuel and varies significantly from multi-component fuel like gasoline.

There is a significant need for additional experimental data at a broader range of conditions to provide direct observations of high-pressure gasoline spray development that can be used to validate the sparse existing experimental data, to identify key spray characteristics required for engine development, and to advance spray theory. This thesis addresses these needs by systematically quantifying gasoline fuel spray development with a range of high-fidelity diagnostics. Additionally, the study includes the first experiments to evaluate the effects of internal nozzle features on gasoline sprays at both conventional and high fuel injection pressures. The results are compared with previous experimental studies and the semi-empirical models proposed in the literature. Recommendations based on the outcomes of the studies are made in each chapter.

## **1.5 Thesis Objective and Chapter Content**

The objective of this dissertation was to quantitatively and qualitatively characterize fuel spray development for high-pressure gasoline at engine-relevant conditions and to provide new insight into the physical mechanisms governing sprays at these extreme pressure conditions. The results are used to understand the mechanisms that govern spray penetration and spread, which are critical to fuel mixing and maximizing efficiency and minimizing emissions. Many of the experimental data are new to the literature and provide the first direct measurements of spray progress. The results guide the development of engine development and operating strategies, as well as inform fundamental theory and empirical and semi-empirical models.

The technical approach used several different experimental platforms to conduct fundamental and applied spray studies. The fundamental studies were used to isolate the effects of state conditions (e.g., chamber pressure and temperature) and operating conditions (e.g., fuel

injection pressure) on fuel spray development and to measure the hydraulic characteristics of the injectors producing the sprays. For the fundamental spray studies, canonical injector geometries were used where key internal features of the nozzles were systematically changed between different injector designs. This allowed the effects of nozzle internal geometry on the spray parameters of high-pressure gasoline to be evaluated for the first time. The applied spray studies used data from production engines and injectors and considered a very large parametric space of operating conditions and hardware configurations to develop statistical understanding of the effects of fuel injector tip-wetting on particulate emissions. The relevant literature to each of the experimental studies is reviewed in each of the corresponding chapters of the thesis.

Chapter 2 presents the results of spray development studies using the University of Michigan (UM) constant volume chamber (CVC) at non-reactive conditions (i.e., low temperature and high pressure) using high-speed diffuse backlit shadowgraph imaging (DBI). The results characterize the spray development for high-pressure reference grade gasoline in terms of spray tip penetration distance, spray tip penetration rate, and spray cone angle, and the results are compared with previous experimental studies and simplified physics-based models that have been proposed in the literature for high-pressure gasoline and diesel sprays. Three injectors and a total of five holes were tested with varying internal geometries with respect to conicity, inlet hole tapering, and hole diameter. A total of five injection pressures and four ambient densities were tested under this configuration. Trends as a function of nozzle geometry and operating conditions are discussed, in addition to the unique and unusual behaviors observed, including the formation of a vapor pre-jet in near nozzle images and spray flutter. The key outcomes of this chapter were the first experimental data on high-pressure gasoline fuel sprays and trends as a function of operating conditions and injector geometry. The contents of this chapter have been included in two peer-reviewed papers which were also presented at the Society of Automotive Engineers (SAE) World Congress [65] and will be presented at the SAE International Powertrains, Fuels and Lubricants Meeting [66].

Chapter 3 presents work conducted in the facilities at Centro Motores Termicos (CMT) at Universitat Politecnica de Valencia (UPV). Two injectors used in the UM CVC studies were also investigated at reacting conditions using the high-temperature high-pressure test rig at UPV. High- and low-temperature conditions were studied at UPV at similar injection and chamber pressures as tested in the UM CVC study. The spray development was visualized using a high-

speed schlieren optical technique. Additionally, the spray momentum rate and the injected mass flux were measured to characterize the hydraulic performance of each injector nozzle. The contributions of this chapter include spray momentum rate and injected mass measurements which are used to interpret the trends observed with the UM CVC data presented in Chapter 2. The data also provide insight into the effects of nozzle geometry on discharge, momentum, area, and velocity coefficients. Such measurements are required to provide in-depth analysis of hydraulic behavior [67]. In addition, the evaporative spray schlieren imaging provides new data to the literature on chamber and fuel injector temperature effects. The results of this chapter are the basis for a journal article in preparation for submission to *Atomization and Sprays*.

Chapter 4 is a study of the effects of fuel-injector tip wetting. Tip surface wetting is a significant source of particulate emissions for spark ignition engines equipped with direction injection. As noted earlier, fuel impingement on the combustion chamber walls, piston crown, and on the fuel injector tip can each contribute to particulate emissions. Tip wetting is a significant source of deposits [68,69] and contributes to particulate emissions during certain engine operating modes [43,49]. As part of this doctoral work, a large array of conditions was tested to determine the relationship between tip wetting and different engines architectures, operating conditions, and injector geometries. Three engines and an array of 35 injectors were tested for different engine loads, engine speeds, fuel injection pressure, and injection timing. The experimental matrix was executed under conditions relevant to tip wetting dominant regimes previously identified with endoscopic images [43]. The results quantify the effects of the operating conditions and hardware configurations on particulate emissions. The chapter includes proposed conceptual mechanisms for tip wetting and tip drying. The contents of this chapter have been accepted for publication in the *Internal Journal of Engine Research*.

The final chapter of the thesis summarizes the key conclusions of each of the studies and provides recommendations for future work.

## References

1. BP Statistical Review of World Energy 2019, London, UK, 2019.
2. Energy Information Administration, "International Energy Outlook," Washington, DC, ISBN 2025869592, 2019.
3. Reitz, H.R., Ogawa, H., Payri, R., Fansler, T., Kokjohn, S., Moriyoshi, Y., Agarwal, A.K.,

- Arcoumanis, D., Assanis, D.N., Bae, C., Boulouchos, K., Canakci, M., Curran, S., Denbratt, I., Gavaises, M., Guenther, M., Hasse, C., Huang, Z., Ishiyama, T., Johansson, B., Johnson, T. V., Kalghatgi, G.T., Koike, M., Kong, S.C., Leipertz, A., Miles, P.C., Novella, R., Onorati, A., ... Zhao, H., "IJER editorial: The future of the internal combustion engine," *Int. J. Engine Res.* 21(1):3–10, 2019, doi:10.1177/1468087419877990.
4. Davis, S.C., Williams, S.E., Boundy, R.G., and Moore, S., "2016 Vehicle Technology Market Report," Oak Ridge, TN, ISBN 1800553684, 2016, doi:10.2172/1127388.
  5. Baglione, M., Duty, M., and Pannone, G., "Vehicle System Energy Analysis Methodology and Tool for Determining Vehicle Subsystem Energy Supply and Demand," *SAE Tech. Pap.* (2007-01-0398), 2007, doi:https://doi.org/10.4271/2007-01-0398.
  6. Carlson, R.B., Wishart, J., and Stutenberg, K., "On-Road and Dynamometer Evaluation of Vehicle Auxiliary Loads," *SAE Int. J. Fuels Lubr.* 9(1):260–268, 2016, doi:10.4271/2016-01-0901.
  7. Thomas, J., "Drive Cycle Powertrain Efficiencies and Trends Derived from EPA Vehicle Dynamometer Results," *SAE Int. J. Passeng. Cars - Mech. Syst.* 7(4):1374–1384, 2014, doi:10.4271/2014-01-2562.
  8. U.S. Environmental Protection Agency, "Clean Air Act," Washington, D.C., 2010.
  9. Sims, R., Schaeffer, R., and Et, A., "Transport. In: Climate Change 2014: Mitigation of Climate Change. Contribution of Working Group III to the Fifth Assessment Report of the Intergovernmental Panel on Climate Change," United Kingdom and New York, NY, 2014.
  10. Office of Transportation and Air Quality, "The 2018 EPA Automotive Trends Report," 2019.
  11. Office of Energy Efficiency and Renewable Energy, "Fuel Economy Guide 2020," 2019.
  12. Kittelson, D.B., "Engines and nanoparticles: A review," *J. Aerosol Sci.* 29(5–6):575–588, 1998, doi:10.1016/S0021-8502(97)10037-4.
  13. Brook, R.D., Rajagopalan, S., Pope, C.A., Brook, J.R., Bhatnagar, A., Diez-Roux, A. V., Holguin, F., Hong, Y., Luepker, R. V., Mittleman, M.A., Peters, A., Siscovick, D., Smith, S.C., Whitsel, L., and Kaufman, J.D., "Particulate Matter Air Pollution and Cardiovascular Disease," *Circulation* 121(21):2331–2378, 2010,

- doi:10.1161/CIR.0b013e3181dbecel.
14. Karakatsani, A., Analitis, A., Perifanou, D., Ayres, J.G., Harrison, R.M., Kotronarou, A., Kavouras, I.G., Pekkanen, J., Hämeri, K., Kos, G.P., Hartog, J.J. De, Hoek, G., and Katsouyanni, K., “Particulate matter air pollution and respiratory symptoms in individuals having either asthma or chronic obstructive pulmonary disease: A European multicentre panel study,” *Environ. Heal. A Glob. Access Sci. Source* 11(1):1–16, 2012, doi:10.1186/1476-069X-11-75.
  15. Saliba, G., Saleh, R., Zhao, Y., Presto, A.A., Lambe, A.T., Frodin, B., Sardar, S., Maldonado, H., Maddox, C., May, A.A., Drozd, G.T., Goldstein, A.H., Russell, L.M., Hagen, F., and Robinson, A.L., “Comparison of Gasoline Direct-Injection (GDI) and Port Fuel Injection (PFI) Vehicle Emissions: Emission Certification Standards, Cold-Start, Secondary Organic Aerosol Formation Potential, and Potential Climate Impacts,” *Environ. Sci. Technol.* 51(11):6542–6552, 2017, doi:10.1021/acs.est.6b06509.
  16. Zhang, S. and McMahon, W., “Particulate Emissions for LEV II Light-Duty Gasoline Direct Injection Vehicles,” *SAE Int. J. Fuels Lubr.* 5(2):637–646, 2012, doi:10.4271/2012-01-0442.
  17. Braisher, M., Stone, R., and Price, P., “Particle Number Emissions from a Range of European Vehicles,” *SAE Tech. Pap. Ser.* 1(Ci), 2010, doi:10.4271/2010-01-0786.
  18. Kontses, A., Ntziachristos, L., Zardini, A.A., Papadopoulos, G., and Giechaskiel, B., “Particulate emissions from L-Category vehicles towards Euro 5,” *Environ. Res.* 182(June 2019):109071, 2020, doi:10.1016/j.envres.2019.109071.
  19. Harada, J., Tomita, T., Mizuno, H., Mashiki, Z., and Ito, Y., “Development of direct injection gasoline engine,” *SAE Tech. Pap.* (412), 1997, doi:10.4271/970540.
  20. Shaik, A., Moorthi, N.S.V., and Rudramoorthy, R., “Variable compression ratio engine: A future power plant for automobiles - An overview,” *Proc. Inst. Mech. Eng. Part D J. Automob. Eng.* 221(9):1159–1168, 2007, doi:10.1243/09544070JAUTO573.
  21. Zhao, F., Asmus, T.N., Assanis, D.N., Dec, J.E., Eng, J.A., and Najt, P.M., “Homogeneous Charge Compression Ignition (HCCI) Engines,” SAE International, ISBN 978-0-7680-1123-4, 2003.
  22. Kalghatgi, G.T., Risberg, P., and Ångström, H., “Advantages of Fuels with High Resistance to to Auto-ignition in Late-injection, Low-temperature, Compression Ignition

- Combustion,” *SAE Int.* (724), 2006.
23. Lavoie, G.A., Ortiz-Soto, E., Babajimopoulos, A., Martz, J.B., and Assanis, D.N., “Thermodynamic sweet spot for highefficiency, dilute, boosted gasoline engines,” *Int. J. Engine Res.* 14(3):260–278, 2013, doi:10.1177/1468087412455372.
  24. Office, V.T., “Advanced Combustion Systems and Fuels,” 2018.
  25. Stanglmaier, R.H. and Roberts, C.E., “Homogeneous Charge Compression Ignition ( HCCI ): Benefits , Compromises , and Future Engine Applications,” *SAE Tech. Pap.* (1999-01–3682), 1999, doi:10.4271/1999-01-3682.
  26. Dec, J.E. and Sjöberg, M., “Isolating the Effects of Fuel Chemistry on Combustion Phasing in an HCCI Engine and the Potential of Fuel Stratification for Ignition Control,” *SAE Tech. Pap.* (2004-01–0557), 2004, doi:10.4271/2004-01-0557.
  27. Chang, K., Lavoie, G.A., Babajimopoulos, A., Filipi, Z.S., and Assanis, D.N., “Control of a Multi-Cylinder HCCI Engine During Transient Operation by Modulating Residual Gas Fraction to Compensate for Wall Temperature Effects,” *SAE Tech. Pap.* 2007(724):776–790, 2007.
  28. Dec, J.E., “Advanced compression-ignition engines - Understanding the in-cylinder processes,” *Proc. Combust. Inst.* 32 II(2):2727–2742, 2009, doi:10.1016/j.proci.2008.08.008.
  29. Kalghatgi, G.T., Risberg, P., and Ångström, H.-E., “Partially Pre-Mixed Auto-Ignition of Gasoline to Attain Low NO<sub>x</sub> at High Load in a Compression Ignition Engine and Comparison with a Diesel Fuel,” *SAE Int.*, 2007, doi:10.4271/2007-01-0006.
  30. Adams, C., “Characterization of Injection Pressure Effects on Gasoline Compression Ignition Combustion,” *UW-Madison Thesis*, 2017.
  31. Dempsey, A.B., Curran, S., Wagner, R., and Cannella, W., “Effect of Premixed Fuel Preparation for Partially Premixed Combustion With a Low Octane Gasoline on a Light-Duty Multicylinder Compression Ignition Engine,” *J. Eng. Gas Turbines Power* 137(11):111506, 2015, doi:10.1115/1.4030281.
  32. Piehl, J. and Bravo, L., “Assessment of Cavitation Models for Computational Fluid Dynamics Analysis of Erosion Risk in a Hydrocarbon-Fueled Nozzle,” 2018, doi:10.13140/RG.2.2.11744.12808.
  33. Yatsuyanagi, N., Sakamoto, H., and Sato, K., Atomization Characteristics of Liquid Jets



- Injected Into a High-Velocity Flow Field, *At. Sprays* 4(4):451–471, 1994, doi:10.1615/atomizspr.v4.i4.50.
34. Yao, C., Geng, P., Yin, Z., Hu, J., Chen, D., and Ju, Y., “Impacts of nozzle geometry on spray combustion of high pressure common rail injectors in a constant volume combustion chamber,” *Fuel* 179:235–245, 2016, doi:10.1016/j.fuel.2016.03.097.
  35. Lefebvre, A.H. and Vincent G. McDonell, “Atomization and Sprays,” Second Edi, ISBN 0891166033, 2017, doi:10.1016/0009-2509(90)87140-N.
  36. Jiang, C., Parker, M.C., Helie, J., Spencer, A., Garner, C.P., and Wigley, G., “Impact of gasoline direct injection fuel injector hole geometry on spray characteristics under flash boiling and ambient conditions,” *Fuel* 241(November 2018):71–82, 2019, doi:10.1016/j.fuel.2018.11.143.
  37. Yamaguchi, A., Koopmans, L., Helmantel, A., Karrholm, F.P., and Dahlander, P., “Spray Characterization of Gasoline Direct Injection Sprays Under Fuel Injection Pressures up to 150 MPa with Different Nozzle Geometries,” *SAE Tech. Pap. Ser.* 1:1–14, 2019, doi:10.4271/2019-01-0063.
  38. Eitel, F., Schäfer, J., Redante, E., Nolte, R., Königstein, A., and Heeger, C., “Potential and Challenges of Fuel Injection Pressure up to 50 MPa for Gasoline Direct Injection Engines,” *26th Aachen Colloq. Automob. Engine Technol. 2017* (Di):489–508, 2017.
  39. Gawlica, T., Samenfink, W., Schünemann, E., and Koch, T., “Model-based optimization of multi-hole injector spray targeting for gasoline direct injection,” *Tagung Einspritzung und Kraftstoffe*, ISBN 1861346433: 271–289, 2019, doi:10.1007/978-3-658-23181-1\_14.
  40. Arsuaga, L.G.G., “Advanced Diagnostics for Spray Behavior , Fuel Impingement , and Soot Processes in Direct Injection Spark Ignition Engines,” University of Michigan, 2019.
  41. Singh, R., Burch, T., Lavoie, G.A., and Wooldridge, M., “Effects of Fuel Injection Events of Ethanol and Gasoline Blends on Boosted Direct-Injection Engine Performance Experimental Set-up,” *SAE Int. J. Fuels Lubr.*, 2017, doi:10.4271/2017-01-2238.Copyright.
  42. Fatouraie, M., Wooldridge, M., and Wooldridge, S., “In-Cylinder Particulate Matter and Spray Imaging of Ethanol / Gasoline Blends in a Direct Injection Spark Ignition Engine,” *SAE Int. J. Fuels Lubr.* 6(1), 2013, doi:10.4271/2013-01-0259.
  43. Fatouraie, M., Peterson, K., Biddappa, B., Livshiz, N., Larimore, J., and Mosburger, M.,

- “Advanced Gasoline Combustion and Engine Controls,” *Reducing Particulate Emissions in Gasoline Engines*, SAE International, Warrendale: 103–114, 2018.
44. Geiler, J.N., Grzeszik, R., Quaing, S., Manz, A., and Kaiser, S.A., “Development of laser-induced fluorescence to quantify in-cylinder fuel wall films,” *Int. J. Engine Res.* 19(1):134–147, 2018, doi:10.1177/1468087417733865.
  45. Serras-Pereira, J., Aleiferis, P.G., and Richardson, D., “An experimental database on the effects of single- and split injection strategies on spray formation and spark discharge in an optical direct-injection spark-ignition engine fuelled with gasoline, iso -octane and alcohols,” *Int. J. Engine Res.* 16(7):851–896, 2015, doi:10.1177/1468087414554936.
  46. Singh, R., Han, T., Fatouraie, M., Mansfield, A., Wooldridge, M., and Boehman, A., “Influence of fuel injection strategies on efficiency and particulate emissions of gasoline and ethanol blends in a turbocharged multi-cylinder direct injection engine,” *Int. J. Engine Res.* 1–13, 2019, doi:10.1177/1468087419838393.
  47. Knorsch, T., Rogler, P., Miller, M., and Wiese, W., “On the Evaluation Methods for Systematic Further Development of Direct-Injection Nozzles,” *SAE Tech. Pap.* 01, 2016.
  48. Medina, M., Alzahrani, F., Fatouraie, M., Wooldridge, M.S., and Sick, V., “Mechanisms of Fuel Injector Tip Wetting and Tip Drying Based on Experimental Measurements of Engine-Out Particulate Emissions from Gasoline Direct Injection Engines,” *Int. J. Engine Res.*, 2020.
  49. Steimle, F., Kulzer, A., Richter, H., Schwarzenthal, D., and Romberg, C., “Systematic analysis and particle emission reduction of homogeneous direct injection SI engines,” *SAE Tech. Pap.* 2, 2013, doi:10.4271/2013-01-0248.
  50. Berndorfer, A., Breuer, S., Piock, W., and Bacho, P. Von, “Diffusion Combustion Phenomena in GDi Engines caused by Injection Process,” *SAE International*, 2013, doi:10.4271/2013-01-0261.
  51. Dageförde, H., Kiefer, A., Samenfink, W., Wiese, W., and Kufferath, A., “Requirements for Spray and Tip Design of a Multi-hole Injector for DISI Engines,” *ICLASS Conf.* 1–8, 2015.
  52. Fischer, A. and Thelliez, M., “Methodology and Tools to Predict GDI Injector Tip Wetting as Predecessor of Tip Sooting,” *SAE Tech. Pap.* (2018-01–0286):1–10, 2018, doi:10.4271/2018-01-0286.

53. Dec, J.E., "A Conceptual Model of DI Diesel Combustion Based on Laser-Sheet Imaging\*," *SAE Technical Paper*, 1997, doi:10.4271/970873.
54. Hiroyasu, H. and Arai, M., "Structure of Fuel Sprays in Diesel Engines," *SAE Tech. Pap.* (900475), 1990, doi:10.4271/900475.
55. Naber, J. and Siebers, D.L., "Effects of Gas Density and Vaporization on Penetration and Dispersion of Diesel Sprays," *SAE Tech. Pap.* (960034), 1996, doi:10.4271/960034.
56. Taşkıran, Ö.O. and Ergeneman, M., "Experimental Study on Diesel Spray Characteristics and Autoignition Process," *J. Combust.* 2011, 2011, doi:10.1155/2011/528126.
57. Payri, R., Viera, J.P., Gopalakrishnan, V., and Szymkowicz, P.G., "The effect of nozzle geometry over internal flow and spray formation for three different fuels," *Fuel* 183, 2016, doi:10.1016/j.fuel.2016.06.041.
58. Payri, R., Gimeno, J., Bracho, G., and Vaquerizo, D., "Study of liquid and vapor phase behavior on Diesel sprays for heavy duty engine nozzles," *Appl. Therm. Eng.* 107:365–378, 2016, doi:10.1016/j.applthermaleng.2016.06.159.
59. Eagle, E.W., Morris, S.B., and Wooldridge, M., "High-speed imaging of transient diesel spray behavior during high pressure injection of a multi-hole fuel injector," *Fuel* 116(0):299–309, 2014, doi:10.1016/j.fuel.2013.07.120.
60. Desantes, J.M., Payri, R., Salvador, F.J., and La Morena, J. De, "Influence of cavitation phenomenon on primary break-up and spray behavior at stationary conditions," *Fuel* 89(10):3033–3041, 2010, doi:10.1016/j.fuel.2010.06.004.
61. Skeen, S.A., Manin, J., and Pickett, L.M., "Simultaneous formaldehyde PLIF and high-speed schlieren imaging for ignition visualization in high-pressure spray flames," *Proc. Combust. Inst.* 35(3):3167–3174, 2015, doi:10.1016/j.proci.2014.06.040.
62. Kim, K., Kim, D., Jung, Y., and Bae, C., "Spray and combustion characteristics of gasoline and diesel in a direct injection compression ignition engine," *Fuel* 109(x):616–626, 2013, doi:10.1016/j.fuel.2013.02.060.
63. Payri, R., Garcia, A., Domenech, V., Durrett, R., and Plazas, A.H., "An experimental study of gasoline effects on injection rate, momentum flux and spray characteristics using a common rail diesel injection system," *Fuel* 97:390–399, 2012, doi:10.1016/j.fuel.2011.11.065.
64. Tian, J., Zhao, M., Long, W., Nishida, K., Fujikawa, T., and Zhang, W., "Experimental

- study on spray characteristics under ultra-high injection pressure for DISI engines,” *Fuel* 186:365–374, 2016, doi:10.1016/j.fuel.2016.08.086.
65. Medina, M., Fatouraie, M., and Wooldridge, M., “High-Speed Imaging Studies of Gasoline Fuel Sprays at Fuel Injection Pressures from 300 to 1500 bar,” *SAE Tech. Pap. c*(2018-01-0294):1–18, 2018, doi:10.4271/2018-01-0294.
  66. Medina, M., Zhou, Y., Fatouraie, M., and Wooldridge, M.S., “High-Speed Imaging Study on the Effects of Internal Geometry on High-Pressure Gasoline Sprays,” *SAE Tech. Pap.*, 2020.
  67. Gimeno, J., “Desarrollo y aplicacion de la medida del flujo de cantidad de movimiento de un chorro diesel,” 2008.
  68. Alzahrani, F., “Theoretical and Experimental Study of Fuel Injector Tip Wetting as a Source of Particulate Emissions in Gasoline Direct-Injection Engines,” University of Michigan, 2020.
  69. Henkel, S., Hardalupas, Y., Taylor, A., Conifer, C., Cracknell, R., Goh, T.K., Reinicke, P.B., Sens, M., and Rieß, M., “Injector Fouling and Its Impact on Engine Emissions and Spray Characteristics in Gasoline Direct Injection Engines,” *SAE Int. J. Fuels Lubr.* 10(2), 2017, doi:10.4271/2017-01-0808.

## Chapter 2

### High Speed Imaging Studies of Gasoline Sprays under Non-Evaporative conditions

*Portions of this chapter appear in the paper Medina, M., Fatouraie, M., Wooldridge, M., “High-Speed Imaging Studies of Gasoline Fuel Sprays at Fuel Injection Pressures from 300 to 1500 bar”, SAE Technical Paper, 2018-01-0294, as well as paper Medina, M., Zhou, Y., Fatouraie, M., Wooldridge, M., “High-Speed Imaging Study on the Effects of Internal Geometry on High-Pressure Gasoline Sprays”, SAE Powertrain, Fuels, and Lubricants, 2020.*

#### 2.1 Introduction

New legislation and initiatives for particulate and greenhouse gas emissions have motivated research to dramatically improve combustion systems. Particularly, the internal combustion engine has seen many new technologies introduced in recent years to improve thermal efficiency as well as reduced vehicle exhaust emissions [1]. Some examples include the shift from port fuel injection to direct fuel injection in gasoline engines [2], downsized and boosted gasoline engines [3], and variable compression ratio engines [4,5]. Direct injection in gasoline engines has increased thermal efficiency and lowered fuel consumption, but with a drawback of increased particulate emissions relative to port fuel injected gasoline engines [6,7]. The increased emissions are attributed to the decreased mixing time inherent to direct injection and fuel wetting combustion surfaces [8–10].

Improving the spray process and fuel atomization can reduce particulate emissions in direct-injection gasoline engines [11,12]. Methods to improve atomization with direct injection include increasing the fuel injection pressure [13,14] and using a multiple injection strategy [15–18]. However, our understanding of high-pressure gasoline spray development is limited to few studies and the possible benefits are not fully understood. The limited knowledge of the spray behavior for gasoline at high pressures is a considerable source of uncertainty, and increasing fuel injection pressures has costs in terms of fuel pump work and friction [13]. Studies of high-

pressure gasoline spray development can fill the gap in understanding and enhance the benefits on combustion systems while minimizing costs.

While some key outcomes have been learned from the few previous computational and experimental studies of gasoline spray behavior at high pressure, the prior work considered a sparse range of hardware and operating conditions. Eitel et al. [13] performed computational and experimental tests for gasoline direct injection (GDI) injectors up to pressure of 500 bar. The computational results showed smaller droplet size and higher evaporated mass for injection pressures of 500 bar compared with 200 bar. The engine results showed that increased injection pressure significantly decreased engine-out particulate emissions by up to 60% with at most 1% fuel economy penalty. However, the authors concluded that injection pressures of 350 bar provide sufficient reduction in particulate emissions that a higher pressure system may not be cost effective particularly if other technologies such as particulate filters and electrification are added. Paz et al. [19] performed engine experiments using 1500 bar injection pressure to study gasoline compression ignition (GCI). The study concluded that controlling mixing with this combustion strategy offered improvements to soot-NO<sub>x</sub> tradeoff with no loss in gross indicated efficiency. Yamaguchi et al. [20] performed spray studies using n-heptane and various nozzle geometries at pressures up to 1500 bar. The authors found divergent nozzles produced shorter penetration than convergent nozzles. Using droplet size measurements, they also concluded increased injection pressure yields smaller droplets with the most pronounced decrease at injection pressures of 800 bar. In Medina et al. [21], experiments were conducted using high pressure gasoline at pressures up to and including 1500 bar with a single orifice injector in a constant volume chamber. The results showed gasoline spray development was a strong function of chamber pressure with a weaker dependence on injection pressure.

Geometric effects and nozzle configuration have been shown to impact the spray mixing and atomization in many diesel fuel injector studies [11,22,23] including the pioneering work of Naber and Siebers [24], Siebers [25,26], and Hiroyasu and Arai [27]. No previous studies have investigated the effects of the nozzle internal flow field on high-pressure gasoline sprays. Therefore, the objective of this study was to quantify the effects of different internal geometries on transient gasoline spray development at high pressures. The current work expands on the earlier study by Medina et al. [21] by considering different nozzle internal geometries.

## 2.2 Experimental Methodology

### 2.2.1 Experimental Facility

The experimental facility used to study the spray development is discussed in detail in Medina et al. [21,28]. The approach is briefly summarized here. Spray development was observed using diffuse backlit shadowgraph imaging in a constant volume chamber. The chamber was equipped with three optical access ports and several ports for instrumentation. Imaging was recorded perpendicular to the injector axis as shown in Figure 2.1. The chamber was pressurized using high-purity nitrogen (PurityPlus Gases, purity rating 99.999%). A K-type thermocouple was used to monitor the chamber temperature and a pressure gauge (Supco-DPG1000) was used to monitor the chamber pressure. The temperature was measured at 298 K with repeatability of 3 K for the full range of experimental conditions. The uncertainty in the chamber pressure was  $\pm 0.2$  bar. The uncertainty in the fuel injection pressure was  $\pm 10$  bar. Table 2.1 provides a summary of chamber pressures and fuel injection pressures studied. All experiments were conducted at a chamber temperature of 298 K and the corresponding densities are listed in Table 2.1.

Table 2.1. Summary of Experimental Conditions

<b>Parameter</b>	<b>Value</b>
Fuel type	Reference grade gasoline
Chamber gas	Nitrogen
Injection pressure [bar]	300, 600, 900, 1200, 1500
Chamber temperature [K]	298
Chamber pressure [bar] (chamber density [kg/m <sup>3</sup> ] at 298K)	1 (1.13), 5 (5.65), 10 (11.33), 20 (22.66)

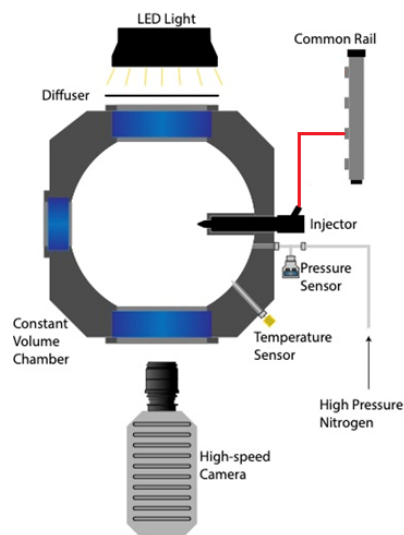


Figure 2.1. Top view schematic of experimental setup for diffuse backlit shadowgraph high-speed imaging including constant volume chamber, light source, camera, and injection system

The fuel used in this study was a reference grade gasoline (Gage Products Co., 40665-55F) with no ethanol. The fuel properties are well documented and a summary is provided in Table 2.2. The fuel was blended with 350 ppm by volume of a fuel lubricity additive (Infinium R655) to allow for operation with diesel pump and injection system. The fuel was pressurized using diesel fuel pump (Bosch CP3) and supplied to a common fuel rail. The pressurized fuel was directly supplied to a single injector.

Table 2.2. Summary of Fuel Properties

Property	Test Method	Value
Fuel type	-	Reference grade gasoline, 40665-55F
Specific gravity 289 K	ASTM D4052	0.743
Reid vapor pressure 310 K [kPa]	ASTM D5191	61.46
Research octane number (RON)	ASTM D2699	91.5
Motor octane number (MON)	ASTM D2700	83.4
Heat of combustion [MJ/kg]	ASTM D240	43.6
H/C ratio [Mole basis]	Gage-calculated	1.91
Distillation, IBP [K]	ASTM D86	305.2
Distillation, 10% [K]	ASTM D86	322.9
Distillation, 50% [K]	ASTM D86	372.4
Distillation, 90% [K]	ASTM D86	428.2

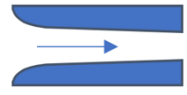


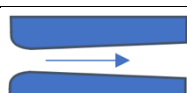



The fuel injectors tested in this study were multi-hole prototype research grade fuel injectors developed by Bosch and are presented in Table 2.3. Injector A was previously used in the study by Medina et al. [21] and had one hole centrally located with a converging nozzle and a high percentage of hydro-erosion rounding of the nozzle inlet. Injector B and C had two holes oriented on the same plane with  $30^\circ$  of separation. The holes were located  $15^\circ$  above and below the horizontal plane as shown in Figure 2.2. Throughout the conditions studied for Injectors B and C, the two sprays did not visibly interact with each other. The key features of the internal geometry for each orifice are provided in Table 2.3. Hydro-erosion increases the static flow rate by rounding the nozzle inlet edges. The percentage of hydro-erosion rounding reflects the percent increase in the static flow rate. Injector B had two nozzles with two different outlet diameters each with straight nozzle passages and no inlet rounding. Injector C had two nozzles, each with the same outlet diameter and each with hydro-erosion rounding of the nozzle inlet. However, one nozzle passageway was diverging and the other was converging. Nozzle passage conicity was measured relative to the nozzle exit diameter, where a straight or uniform passageway had a conicity of 0, a converging nozzle had a positive conicity, and a diverging nozzle had a negative conicity. Table 2.3 includes sketches of the different nozzle internal geometries. The schematics were made to describe the geometry visually but were not drawn to scale and the arrow indicates the flow direction. All nozzles were the same length from inlet to outlet. All injectors were used in the same experimental facility and electronically controlled using a LabView based program with 1 ms duration injection events.



Figure 2.2. Schematic of the nozzle orifice configuration of injector B and C.

Table 2.3. Injector Orifice Information

Injector	Orifice	Normalized outlet diameter*	Conicity**	Hydro-Erosion Rounding	Angle from center
A	Hole 1	0.578	1.5	40%	
B	Hole 1	0.578	0	0%	
	Hole 2	1	0	0%	
C	Hole 1	0.789	-1.5	20%	
	Hole 2	0.789	3.5	20%	

\*Outlet diameter normalized to the maximum outlet diameter studied.

\*\*Defined as  $k = (D_{in} - D_{out})/10$

A high-speed camera (Vision Research Phantom v7.11 12-bit CMOS array) was used to capture the injection events. Three data sets were collected: two macroscopic spray images for injector A, B, and C and one near-nozzle images for injector A. Camera settings for each data set are listed in Table 2.4 The lens used for all the experiments were a Nikon Nikkor 50 mm lens and 105 mm lens.

Table 2.4. Summary of Camera Conditions

Setting	Bulk Spray Imaging (Injector A)	Bulk Spray Imaging (Injector B and C)	Near Nozzle Imaging (Injector A)
Frame rate [fps]	69,000	67,000	280,991
Exposure time [ $\mu$ s]	14	7	3.2
Lens aperture [f/#]	5.6	5.6	4
Camera resolution [pixel $\times$ pixel]	608 $\times$ 152	304 $\times$ 232	208 $\times$ 64
Image resolution [pixels/mm]	13.9	7.4	63.6
Lens (Nikon Nikkor)	105 mm	50 mm	105 mm

### 2.2.2 Image Processing

Image processing techniques were used to identify and quantify key metrics such as spray tip penetration distance, and spray angle. The rate of spray tip penetration was derived from the penetration time histories. The images were also evaluated to determine if cavitation effects occurred (e.g. sudden expansions in spray angle) [29,30]. The following steps were used to process all the images. Frame sequences were converted from color to grey scale. From grey scale, the images were converted to binary images with a threshold level. The binary images were used to determine the spray tip penetration distance ( $S$ ) and spray angle ( $\theta$ ) for each image sequence. The spray tip penetration distance was determined as the farthest point of the spray from the center of the injector nozzle which was set as the origin of the coordinate system. The spray angle was determined as the inclusive angle of the spray at one third the maximum length of the spray ( $S/3$ ). These definitions are visually defined in Figure 2.3. The spray tip penetration rate was determined by differentiating the spray tip penetration distance data using a forward difference approximation. For simplicity, spray tip penetration distance and spray tip penetration rate are referred to as penetration distance and penetration rate, respectively.

Sensitivity analysis was performed to determine the effect of the binary threshold level on the spray characterization. The sensitivity analysis showed less than 0.8 mm difference in measured penetration distance between 10% variation in threshold levels. The sensitivity analysis also showed differences of less than  $1.5^\circ$  in spray angle for the same range of threshold values. Averages of  $S$  and  $\theta$  for each condition were calculated over the 20 injection events. As seen in the results presented below, the variability in each injection event was larger than the uncertainty due to the image processing.

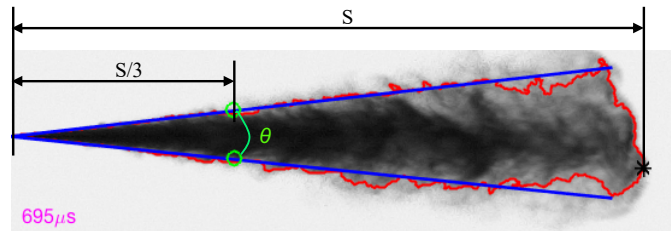


Figure 2.3. Greyscale spray image overlaid with the binary spray contour (red), the spray angle reference lines (blue), the one-third maximum penetration length (green circles), and the maximum penetration length (black asterisk). The image represents an injection event for 600 bar injection pressure and 20 bar chamber pressure. The spray angle shown is  $12.7^\circ$  and the maximum penetration length is 37.9mm

## 2.3 Results

The design of experiments included a large range of experimental conditions leading to a significant amount of imaging data. In the interests of conciseness, imaging results for a limited set of injection pressures and chambers pressure are presented here. Similarities and differences in the results from the other operating conditions are reported relative to the trends for these reference conditions.

### *2.3.1 Macroscopic Spray Characteristics: Operating Conditions Effects*

#### Penetration distance and rate

The results shown are an average of 20 repetitions and the error bars indicated one standard deviation from the mean. The dashed horizontal line in the penetration distance figures represents the optical accessibility limit which is set by the size of the imaging window in the CVC. The start of injection (SOI) was defined from the images as the time of the frame immediately prior to the frame where fuel visibly exited the nozzle. The uncertainty associated with the SOI for the bulk spray events during recording was  $\pm 7.25 \mu\text{s}$ , while the average standard deviation for the average SOI was  $\pm 6.1 \mu\text{s}$ . The penetration rate is calculated using the central difference method and the spray break-up time is defined as the time of maximum penetration rate.

The results for spray tip penetration distance and spray tip penetration rate are presented in Figure 2.4 for the 1500 bar injection pressure and a range of chamber pressures from 1 to 20 bar for Injector A hole 1. As seen in Figure 2.4a, the penetration distance was similar for each condition before the spray break-up time, after which the penetration distance data diverged, with lower chamber pressures resulting in faster penetration. In Figure 2.4b, the maximum penetration rate increases as a function of decreasing chamber pressure. Note that at lower chamber pressures, the penetration distance develops faster thus reaching the optical limit sooner. Penetration rate data at the optical limit are excluded from Figure 2.4b.

The similarity in penetration distance at early times indicates the early spray development was not strongly correlated with chamber pressure, which is consistent with this portion of the spray development being momentum driven. The penetration distance after the spray break-up time was a strong function of chamber pressure, which is again consistent with expectations for spray development at later times, when fluid mixing and entrainment dominate. Similar trends

were observed for injection pressures of 300, 600, 900, and 1200 bar. After the spray break-up time, the penetration distance was longer for the lower chamber pressures and reached the optical limit first, following the same trend as higher injection pressures. The results at 300 bar showed a slight variation in penetration distance between all four chamber conditions at early times. The 300 bar injection pressure data set exhibited the greatest variability from cycle to cycle, which may be due to challenges controlling the fuel rail pressure at 300 bar.

Figure 2.5 shows the penetration distance and penetration rate for 20 bar chamber pressure for different fuel injection pressures for Injector A Hole 1. In Figure 2.5a, the early time histories of the penetration distance are similar for all injection pressures except 300 bar, and the results diverge after the spray break-up time. In Figure 2.5b, as the injection pressure increased, the maximum penetration rate also increased. After the spray break-up time, the penetration rate was comparable for all conditions, indicating no significant correlation between penetration rate and injection pressure after the break-up time for the conditions studied. Comparison of the results of Figure 2.4 and 2.5 indicate a stronger sensitivity of the spray development (after the spray break-up time) to chamber pressure in comparison with fuel injection pressure. Such trends have been previously observed for diesel sprays [24]. Similar trends were observed at the lower chamber pressures studied. Please see the Appendix 1 for the 1, 5 and 10 bar results.

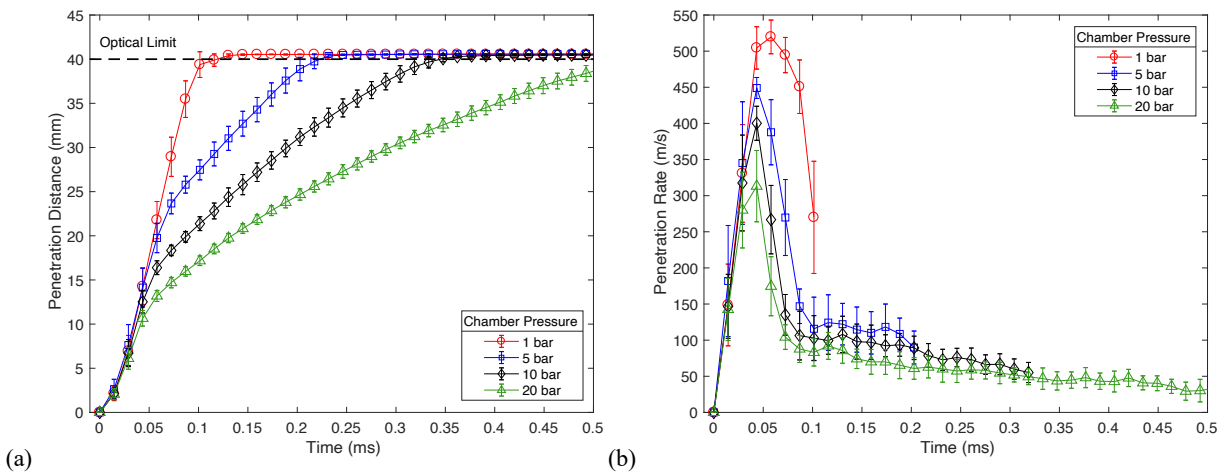


Figure 2.4 (a) Average penetration distance, and (b) average penetration rate at 1500 bar injection pressure for different chamber pressures. The spray break-up time is the time of maximum penetration rate. The error bars are the standard deviation of 20 experiments.

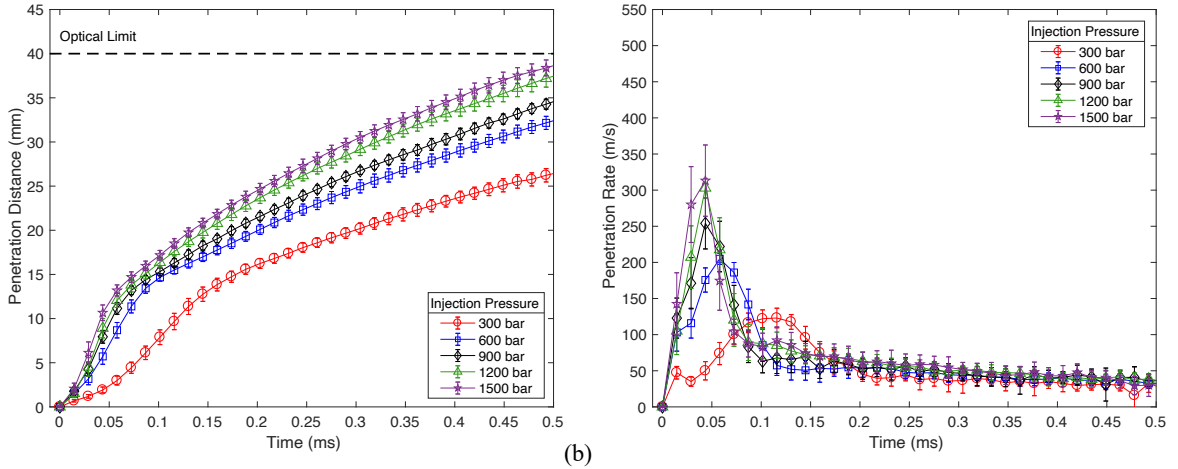


Figure 2.5. (a) Average penetration distance, and (b) average penetration rate for 20 bar chamber pressure for different fuel injection pressures. The spray break-up time is the time of maximum penetration rate. The error bars are the standard deviation of 20 experiments.

Figure 2.6 compares the spray break-up times for all chamber pressures and injection pressures studied. At the lowest fuel injection pressures of 300 bar, the spray break-up time was most sensitive to chamber pressure. The 300 bar injection pressure also yielded the longest spray break-up times. Thus, for 300 bar, the spray was controlled by momentum for a longer period of time compared with higher injection pressures. However, the momentum of the fluid at 300 bar injection pressure is lower and the penetration distance reflects that, which can be seen in Figure 2.5 and in the appendix. As injection pressure increased, the spray break-up times decreased, and the sensitivity to the chamber pressure decreased. In particular for 1200 bar injection pressure and higher, the spray break-up times for the different chamber pressures were within the scatter of the data, and for several of the high fuel injection pressure conditions, there was no measured difference in spray break-up time.

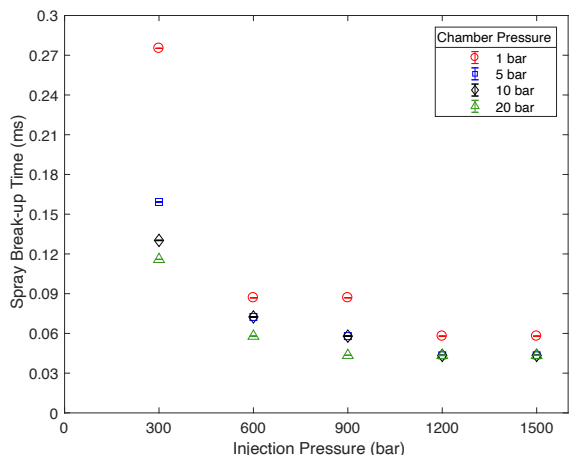


Figure 2.6. Comparison of all average spray break-up times. The error bars represent the standard deviation of the average of 20 experiments.

The results for penetration distance and penetration rate are presented in Figure 2.7 for a chamber pressure of 20 bar (density of  $22.66 \text{ kg/m}^3$ ), and injection pressures from 300 and 1500 bar for Hole 1 of Injector B. The dashed horizontal line in the figure represents the optical accessibility limit (i.e., the imaging limit due to the size of the chamber window). The penetration rate was calculated by differentiating the penetration distance data with a central difference method. As injection pressure increased, the penetration distance increased; however, the penetration distance increased at a faster rate at early times, before the time of maximum penetration rate (i.e., the spray break-up time) as seen in Figure 2.7b. After the spray break-up time, the penetration rate for all injection pressures was nearly identical and within the standard deviation of the data. Additionally, at higher injection pressure, i.e. 1200 and 1500 bar, the penetration distance was less sensitive to changes in injection pressure. Whereas, at lower injection pressures the penetration distance showed slightly more sensitivity to changes in injection pressure. For example, the maximum penetration rate differs by 47% between 300 to 600 bar and by 15% between 1200 and 1500 bar. These trends are consistent for all chamber densities and injector geometries studied.

Figure 2.8 shows the penetration distance and penetration rate at an injection pressure of 1500 bar for chamber pressures from 1 to 20 bar for the same Injector B Hole 1. The penetration distance shows more sensitivity to changes in chamber pressure at a constant injection pressure than to changes in injection pressure at a constant pressure. However, changing chamber pressure did not impact the penetration rate prior to the spray break-up time (before  $59.8 \mu\text{s}$ ), and the penetration rate immediately after the spray break-up time decreased with increasing chamber pressure. These trends were also observed for all injector geometries.

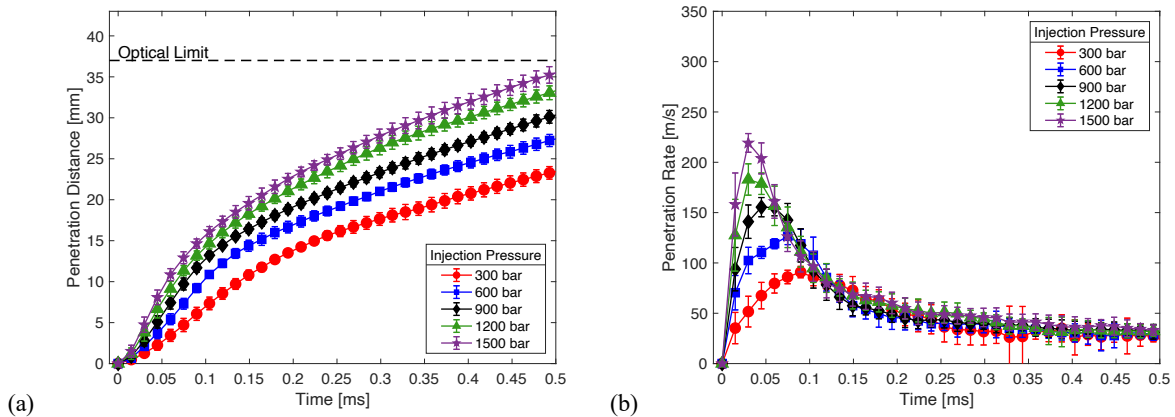


Figure 2.7. (a) Average penetration distance and (b) average penetration rate at 20 bar chamber pressure for Injector B Hole 1

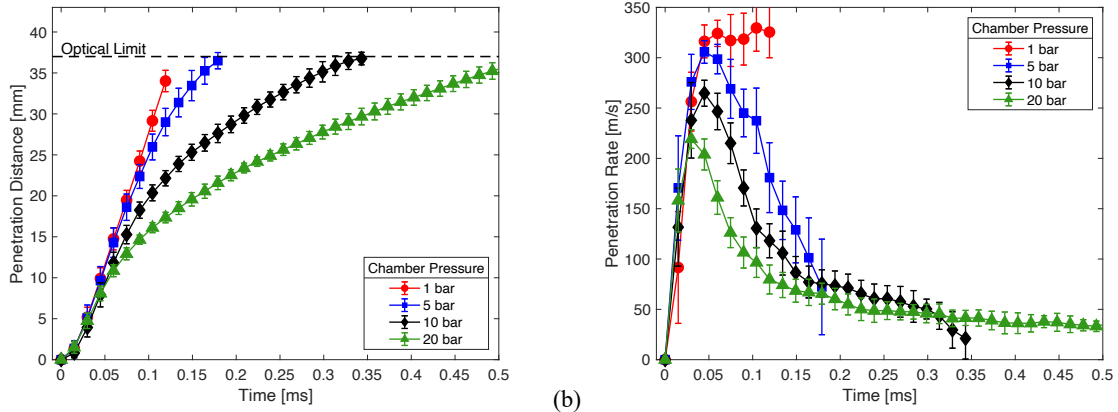


Figure 2.8. (a) Average penetration distance and (b) average penetration rate at 1500 bar injection pressure for Injector B Hole 1

### Spray angle

The spray angle data corresponding to the results presented in Figures 2.4 and 2.5 for Injector A hole 1 are presented in Figure 2.9. The results show the trends of the spray angle as a function of chamber pressure with fixed fuel injection pressure (Figure 2.9a) and as a function of fuel injection pressure for fixed chamber pressure (Figure 2.9b). There was little variability in the spray angle data for either data set at times earlier than the spray break-up time. After the spray break-up time, the spray angle showed significant sensitivity to the chamber pressure, with differences in spray angle of  $2^\circ$  to  $6^\circ$  between the different chamber pressures, and the spray angle increased significantly with increasing chamber pressure. The spray angle showed less sensitivity to the fuel injection pressure, as seen in Figure 2.9b, especially for fuel injection pressures of 900 bar and higher. All conditions reached steady spray angle values at times much later than the spray break-up time.

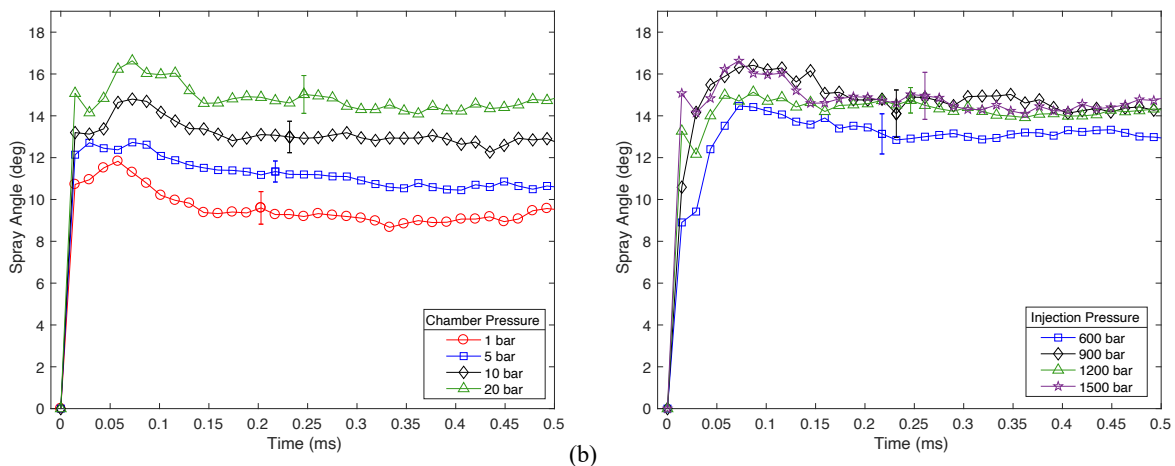


Figure 2.9. (a) Chamber pressure effects on average spray angle at 1500 bar injection pressure. (b) Injection pressure effects on average spray angle at 20 bar chamber pressures. For both panels, the error bars indicate one standard deviation of the average of 20 experiments.



Results for the spray angle measurements are presented in Figure 2.10a for Injector B Hole 1. The results showed no sensitivity to changing fuel injection pressure with fixed chamber pressure. However, the effects on changing ambient pressure differed based on the fuel injection pressures and injector geometry. At high fuel injection pressure, like the data shown in Figure 10b for 1500 bar, the higher chamber pressures yielded wider spray angles, and the lower chamber pressures (e.g., 1 and 5 bar) showed no effect on spray angle. This trend was consistent for all nozzles tested. However, at lower injection pressures (e.g., 600 to 900 bar, not shown here, please see Appendix 1), the spray angle increased by 2° to 4° for each increase in chamber pressure for Injector B. Spray angle measurements for Injector C showed greater variability at higher chamber pressures with spray angle increased by 1° to 3°.

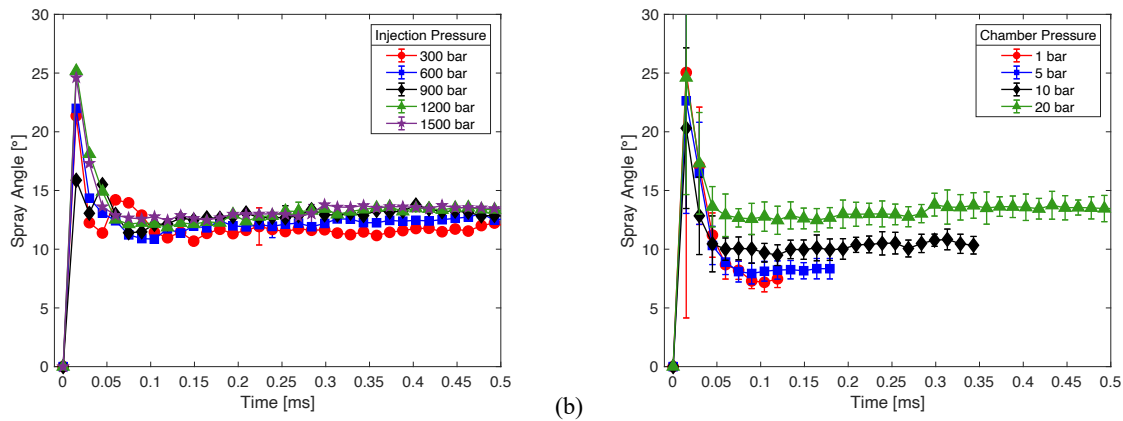


Figure 2.10. Average spray angle for Injector B Hole 1 for (a) a fixed chamber pressure of 20 bar and (b) fixed injection pressure of 1500 bar.

### 2.3.2 Macroscopic Spray Characteristics: Injector Geometry Effects

The comparisons of the effects of the differences in the internal nozzle geometries were categorized into three pairs: the effects of inlet hole rounding, the effects of hole diameter, and the effects of hole conicity. Figure 2.11 summarizes the spray development characteristics for the comparison between Injector A Hole 1 and Injector B Hole 1 at 1200 bar injection pressure and 20 bar chamber pressure. The data from the converging nozzle with rounded inlet are from Injector A Hole 1 and the data from the straight hole nozzle are from Injector B Hole 1. The results show Injector A Hole 1 had slightly higher spray penetration distance at an equivalent point in time compared with the straight hole nozzle. The maximum penetration rate is also notably higher by 30% with the rounded inlet nozzle. Spray angle for Injector A Hole 1 is higher for a portion of the spray development (0.05 – 0.25 ms). At later times in the injection event ( $t >$

0.3ms), both injector holes exhibited similar spray angles and penetration rates as seen in Figure 2.11 (b and c). Injector A Hole 1 consistently resulted in higher penetration distances, penetration rates, and spray angles for all operating conditions tested.

The effects on mass flow rate may explain some of the trends for spray development as a function of nozzle geometry. Using Bernoulli's principle between the orifice inlet and outlet and the definition of discharge coefficient, the mass flow rate equation can be expressed as follows [24,31]:

$$\dot{m} = C_d A_o \sqrt{2\rho\Delta P} \quad (1)$$

where  $A_o$  is the cross-sectional area of the nozzle. Equation 1 can be used to compare the mass flow rate between Injector A hole 1 and Injector B hole 1. For the same operating conditions, the fuel density,  $\rho$ , and pressure differential,  $\Delta P$ , are nominally identical for the two nozzle holes and only the discharge coefficient,  $C_d$ , differ. A converging nozzle has been shown to have higher discharge coefficients for diesel fuel under cavitating and non-cavitating flows [29,31]. This is primarily due to the reduced effect of flow separation and the reduced severity of cavitation. Hydroerosion rounding of the inlet nozzle of Injector A Hole 1 reduces the probability of flow separation and is expected to produce a more evenly distributed flow inside the nozzle. Both effects should result in a larger effective outlet area compared with the straight nozzle. As a consequence of higher  $C_d$  Injector A Hole 1 is expected to have a higher mass flow rate than Injector B Hole 1, which could be the cause of the higher penetration distance, rate, and spray angle for the data shown in Figure 2.11.

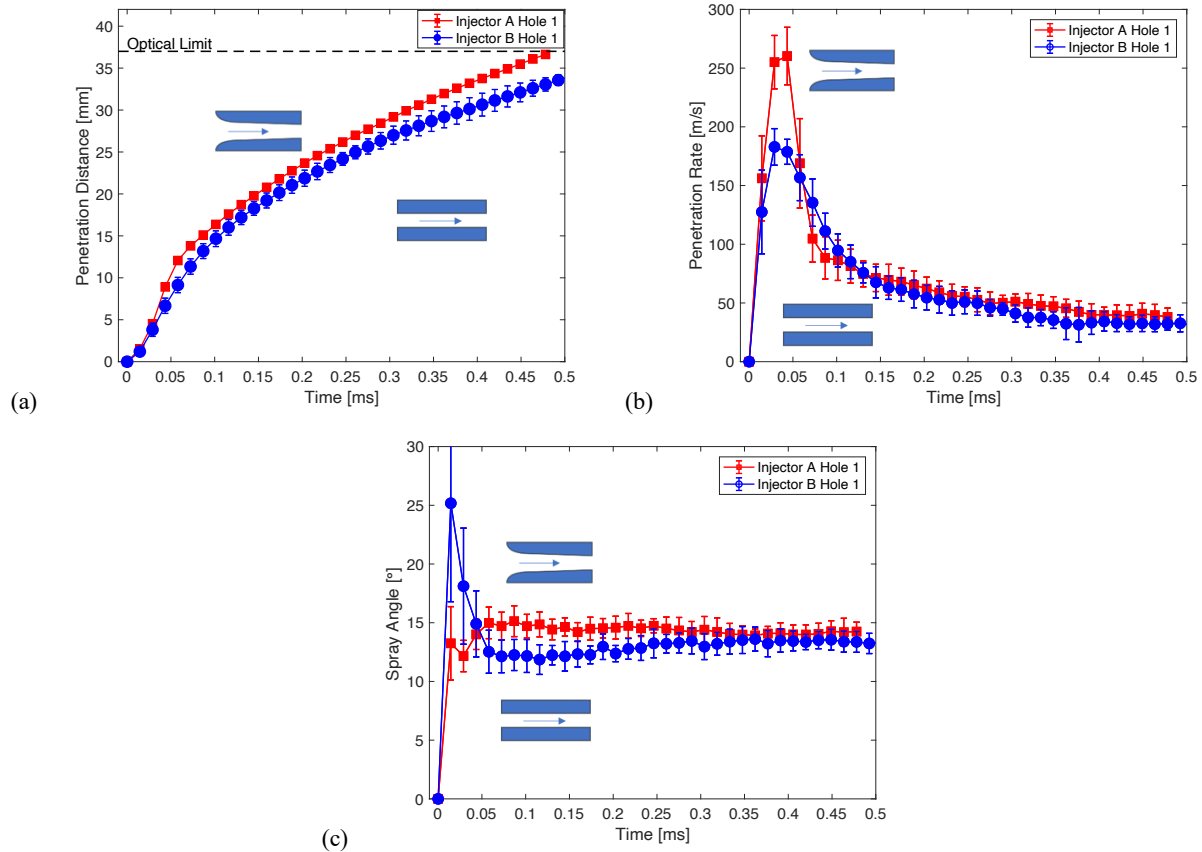


Figure 2.11. Comparison of spray development results of Injector A Hole 1 and Injector B Hole 1 at 1200 bar injection pressure and 20 bar chamber pressure. (a) average penetration distance (b) average penetration rate (c) average spray angle

The effects of nozzle diameter are presented in Figure 2.12 for 1500 bar injection pressure and 20 bar chamber pressure. Injector B Hole 2 is twice the diameter of Injector B Hole 1, which leads to larger spray angles as well as higher penetration rates at times after spray breakup compared with the smaller nozzle hole (by 19%). The results are per expectations where the larger diameter nozzle yields a higher mass flow rate, and therefore higher penetration distance. These trends were consistent across all operating conditions tested. Bergstrand et al. [32] studied injector geometry effects on diesel surrogate spray development with laser induced exciplex fluorescence. Two cylindrical orifices were tested with differences in outlet diameter. The larger outlet diameter was found to have higher gas phase penetration and spray volume, similar to the data reported in this study. Both nozzles had similar penetration distances before the spray break-up time and then diverged in penetration distance after spray break-up time, as was observed here and seen in Figure 2.12. Bergstrand et al. [32] attributed the behavior to lower mass flow rate and subsequently lower jet momentum from the smaller flow area. Similar trends were reported by Hiroyasu and Arai [27] in their study of high pressure diesel fuel sprays.

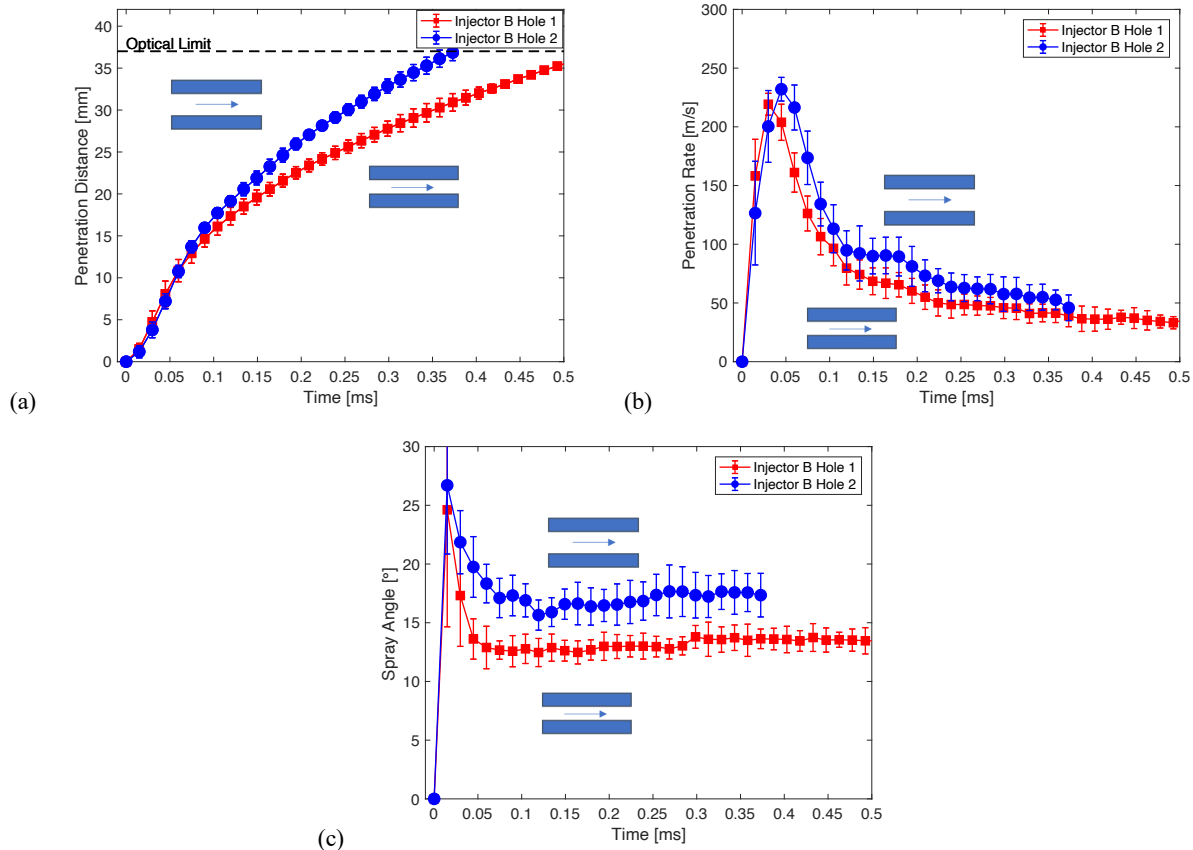


Figure 2.12. Comparison of spray development at 1500 bar injection pressure and 20 bar chamber pressure as a function of nozzle size where the diameter of Injector B Hole 1 is  $\frac{1}{2}$  that of Injector B Hole 2 (a) average penetration distance (b) average penetration rate (c) average spray angle

Figure 2.13 compares the effects of different nozzle conicity on spray development for 1500 bar injection pressure and 20 bar chamber pressure. The nozzle with a converging hole has slightly higher penetration distance at later times (e.g., after 0.2 ms) compared with the diverging hole. This behavior can be attributed to the higher outlet velocities that are caused by a converging nozzle. The diverging nozzle has a wider spray angle, which is attributed to the expansion of the flow due to the diverging flow passage.

Consistent spray development trends were observed when all nozzles were compared at the different operating conditions investigated. Injector B Hole 1 (the cylindrical nozzle with smallest outlet diameter) consistently had the lowest spray angle for all conditions tested, while Injector C Hole 1 (the diverging nozzle) had the highest spray angle. The first trend highlights that a small cylindrical nozzle has a small effective area leading to lower entrainment and mixing rates while a diverging nozzle has the opposite effect. Injector B Hole 2 (the largest outlet diameter) resulted in the highest penetration distance for a majority of the tested conditions. The

trend highlights the need to consider the outlet diameter particularly with respect to fuel impingement. Table 2.5 summarizes the effects of the nozzle internal features on the trends observed for penetration distance and spray angle.

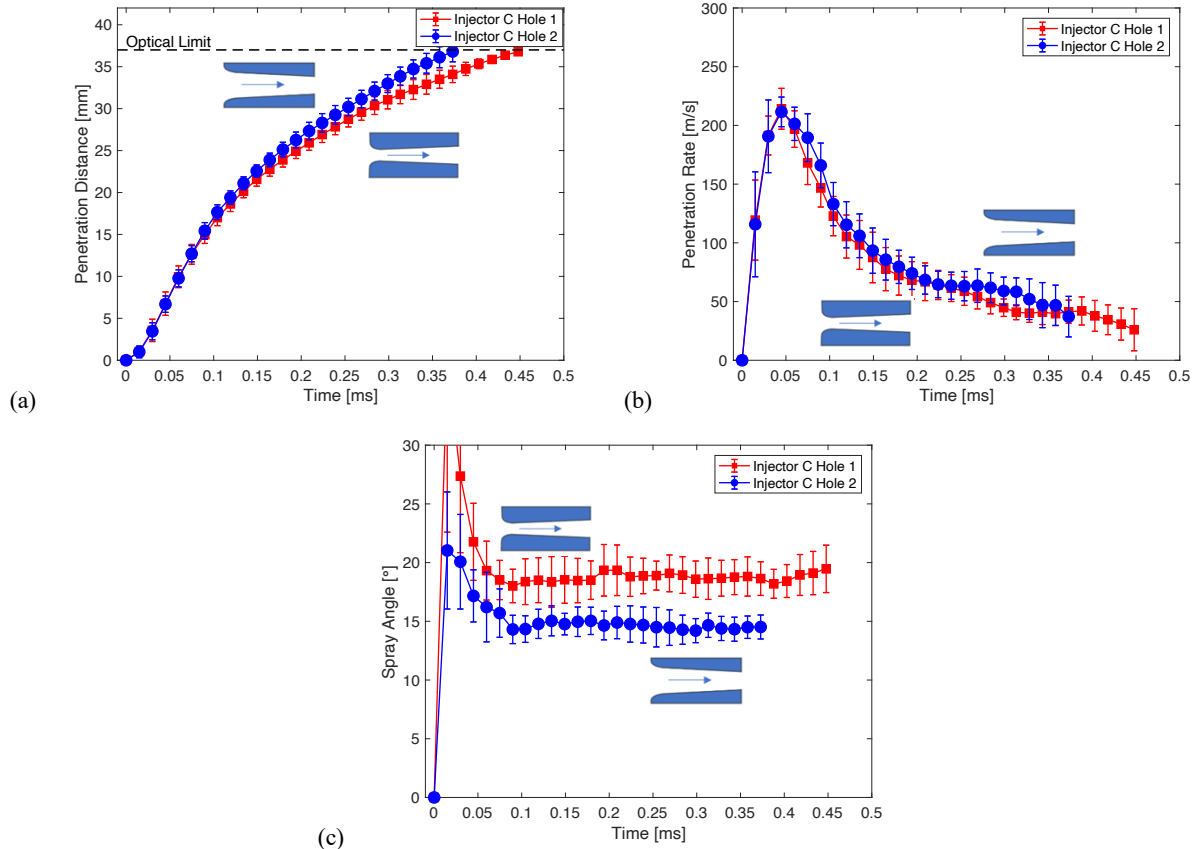


Figure 2.13. Comparison of spray development metrics between both holes in injector C for 1500 bar injection pressure and 20 bar chamber pressure (a) average penetration distance, (b) average penetration rate, and (c) average spray angle

Table 2.5. Effects of nozzle internal features on spray development

Parameter	Increasing nozzle diameter	Converging/Diverging	Inlet rounding
Penetration distance	++ (after spray break-up time)	+ (converging, after spray break-up time)	+
Spray Angle	++	++ (diverging)	+ (after spray break-up time)
Spray Flutter	++	++ (diverging)	+

### 2.3.3 Stochastic behavior of spray development

#### Early development of near-nozzle spray

High magnification imaging of the region near the exit of the nozzle showed some interesting and variable phenomena during the very early time of the spray development. Figures 2.14 and 2.15 show examples of two sequences of near-nozzle images indexed by the time after SOI for conditions of 20 bar chamber pressure and 600 bar fuel injection pressure (Figure 2.14) and 20 bar chamber pressure and 1500 bar fuel injection pressure (Figure 2.15). The first column of each figure shows image sequences where a lower contrast mixture exited the nozzle before a stream of higher contrast liquid fuel was recorded. The second column of each figure shows typical spray development recorded from a different injection event at the same conditions, where no anomalous spray development was observed. The contours of the typical spray development are highlighted in red in the middle column of Figures 2.14 and 2.15. The last column of each figure shows the red contour of the typical spray development superimposed on the anomalous spray images. Due to the lower contrast, the fluid ejected at early times in the anomalous sprays was identified as a vapor pre-jet. Comparison of the development of the anomalous spray with the red contour of the typical spray highlights the differences between the two injection events. The vapor pre-jet takes longer time to develop at lower fuel injection pressure, and consequently the vapor pre-jet significantly delays the liquid spray penetration. The imaging data show the vapor pre-jets exhibited similar shape as the typical liquid sprays with similar spray angles, indicating the pre-jet delays spray development, but does not alter the physical structure of the liquid spray.

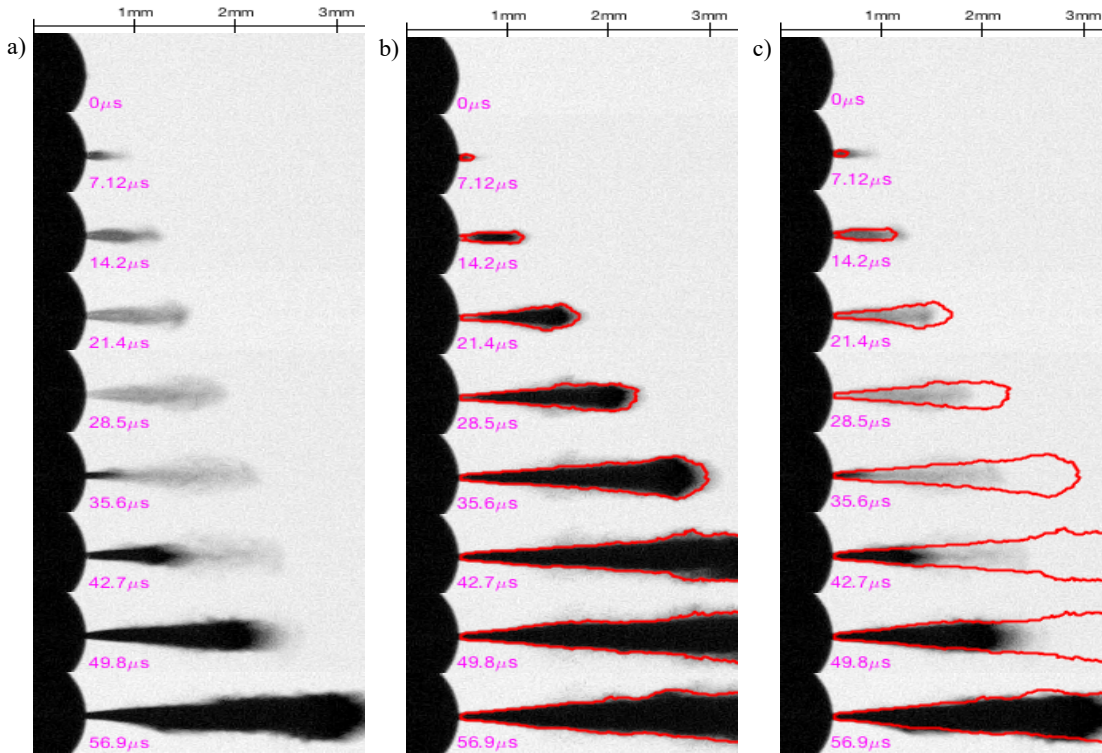


Figure 2.14. Series of greyscale images for a chamber pressure of 20 bar and injection pressure of 600 bar showing (a) anomalous spray images, (b) typical spray images with continuous spray development and red contours, and (c) anomalous images with red contours superimposed

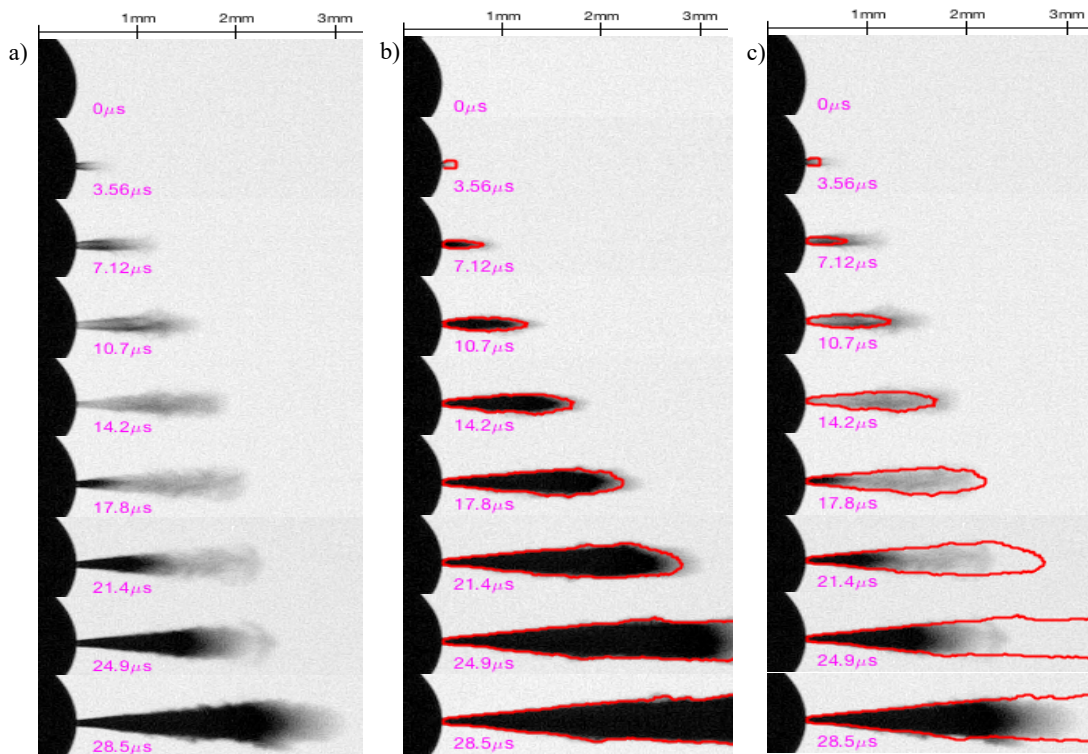


Figure 2.15. Series of greyscale images for a chamber pressure of 20 bar and injection pressure of 1500 bar showing (a) anomalous spray images, (b) typical spray images with continuous spray development and red contours, and (c) anomalous images with red contours superimposed

The vapor pre-jets were not observed at all conditions. The frequency of occurrence of the vapor pre-jets was determined to identify relationships with the experimental conditions. The results are presented in Figure 2.16 and show the observation of the pre-jets directly correlated with chamber pressure and, interestingly, not with fuel injection pressure. The events also occurred randomly amongst the 20 injection events; not in a particular order. One thought was the phenomena might be due to cavitation which was expected to correlate with the ratio of the fuel injection pressure to the chamber pressure, as described by the cavitation number [33]. The association of the data with only the chamber pressure indicates cavitation is not likely the cause of the early jet phenomena. Instead, the strong dependence on chamber pressure indicates that the vapor pre-jet is caused by the ingestion of chamber gases when the valve is open or due to interaction of the needle with the injector sac volume.

Vapor pre-jets have been identified in previous injection studies of diesel fuel [34–36]. In the study by Crua et al. [35], the formation of the vapor pre-jet resembled a mushroom head and with a distinctly different shape when compared to the bulk liquid fuel. On the contrary, the pre-jets observed in this study were similar in shape and development to the bulk spray with the exception of the observations for the 300 bar injection pressure conditions. More filamentous shapes were formed at 300 bar as seen in Figure 2.17 for 20 bar chamber pressure.

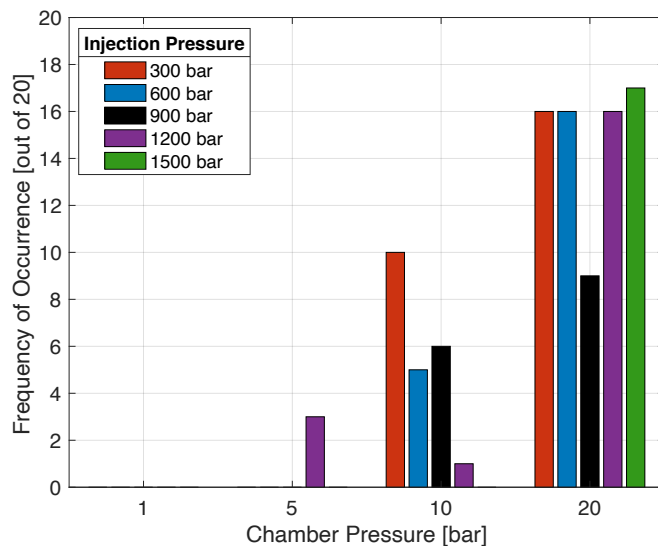


Figure 2.16. Frequency of occurrence of the vapor pre-jets for the conditions investigated in the study.



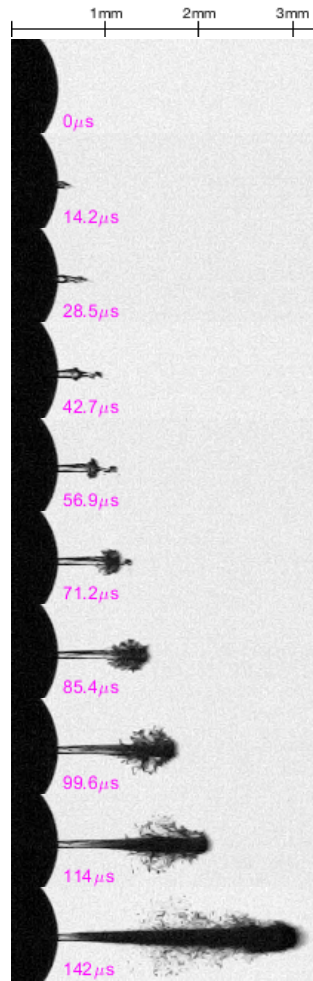


Figure 2.17. Series of greyscale near nozzle images for 300 bar fuel injection pressure and chamber pressure of 20 bar.

### Spray flutter

Increasing hydro-erosion rounding and conicity reduce the likelihood of flow separation at the inlet of the nozzle. Flow separation has been reported to cause cavitation in fuel injector nozzles, which has detrimental effects in terms of injector durability and injector performance [37,38]. Additionally, high-pressure gasoline is expected to increase the probability of cavitation due to the higher volatility of gasoline in comparison with diesel fuel. While identifying cavitation using the imaging data outside/downstream of the nozzle exit did not initially appear possible, some interesting behavior was observed during the spray development that may be indication of cavitation. Specifically, near the exit region of the nozzle, large fluctuations in the spray structure, described as spray flutter here, were observed at some conditions.

Figure 2.20 shows an image sequence of the spray flutter for Injector C Hole 1 and Injector C Hole 2 for 1500 bar injection pressure and 1 bar chamber pressure. The image

sequence starts 0.716 ms after the start of injection. The images show the spray angle for Hole 2 is stable and axisymmetric; however, the images of the spray from Hole 1 show varying spray angle for the same time. For example, for Hole 1, the spray is symmetric at 0.716 ms near the nozzle exit, and then an asymmetric feature develops and is observed in the next image in the sequence. The spray subsequently recovers a symmetric pattern near the nozzle exit at approximately 0.761 ms, and then the process starts again. The asymmetric features are highlighted by the red circle in Figure 2.20 for clarity. The features were present at other conditions and appeared above and below the spray. Spray flutter was observed at other operating conditions and was sensitive to the characteristics of the injector nozzle geometry. Injector C Hole 1 and Injector B Hole 2 showed the largest effects of spray flutter compared with the other nozzle geometries tested.

Figure 2.18 compares the cycle specific spray angle data from Figure 2.20 with the cycle-averaged data. The spray angle data showed the effects of spray flutter were repeated throughout the spray development. The repetition looked cyclic with a characteristic frequency but a Fast Fourier Transform (FFT) analysis did not reveal such behavior for any of the cycles at any of the conditions tested. Additionally, the results showed that while there is measurable change in the cone angle in the particular cycle presented, the average behavior of the spray angle is smooth without bulk repeatable variations in spray angle. In order to quantify the spray flutter, the difference between the spray angle of the instantaneous cycle and the cycle average was quantified. The mean-squared-difference is presented in Figure 2.19. The results showed Hole 1 exhibited significantly higher spray flutter than Hole 2 for all cycles at the test conditions. Additional data presented in Figure 2.19b for both holes of Injector B at the same operating condition show Hole 2 exhibited statistically higher flutter than Hole 1. Spray flutter for Injector C Hole 1 was highest at 1 bar chamber pressure, while for Injector B, spray flutter was highest at 20 bar chamber pressure. Table 2.5 summarizes the effects of injector geometry on spray flutter.

Sudden expansion in spray angle has been attributed to internal nozzle cavitation with diesel operation [30,39]. However, the previous diesel fuel studies showed cavitating nozzles consistently produced larger symmetric spray angles as opposed to the oscillating trend observed in the current work and shown in Figure 2.18 for Hole 1. The asymmetric feature presented in Figure 2.20 also caused an increased spray angle. Yue et al. [40] performed computational studies of GDI injectors to compare machining effects on internal nozzle geometry. Yue et al.

compared an idealized hole with a perfect surface finish with a real nozzle with micron-resolved finish details. The authors concluded that surface roughness and manufacturing defects generated unstable structures along the jet surface such as instability waves similar to the asymmetric feature observed in the current work. Desantes et al. [41] performed near-nozzle imaging of diesel sprays with a single-hole nozzle to examine influences of cavitation. Cavitation bubbles were observed outside the nozzle particularly for low chamber pressure conditions. The authors concluded that cavitation bubbles induced spray boundary oscillations. These previous studies suggest the oscillating spray angle observed here may be caused by surface roughness, machining defects and/or cavitation. Cavitation is considered a likely cause here due to the high fuel volatility and high-pressure fuel injection conditions.

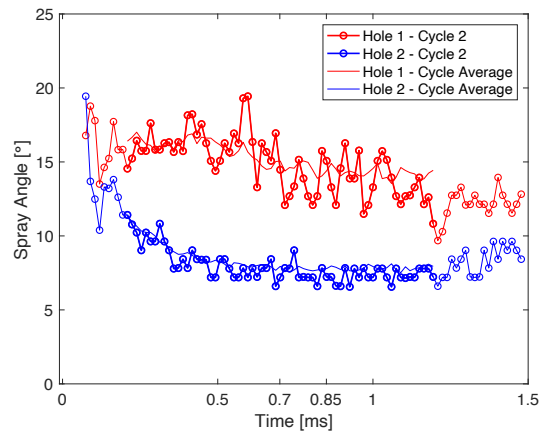


Figure 2.18. Comparison of single cycle spray angle data with cycle averaged data for Injector C Hole 1 and Injector C Hole 2

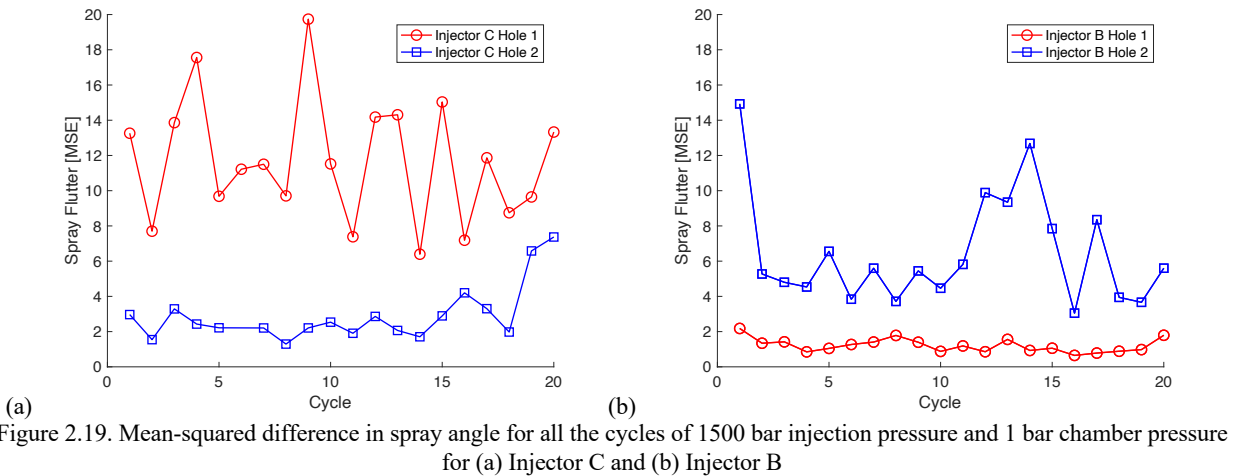


Figure 2.19. Mean-squared difference in spray angle for all the cycles of 1500 bar injection pressure and 1 bar chamber pressure for (a) Injector C and (b) Injector B

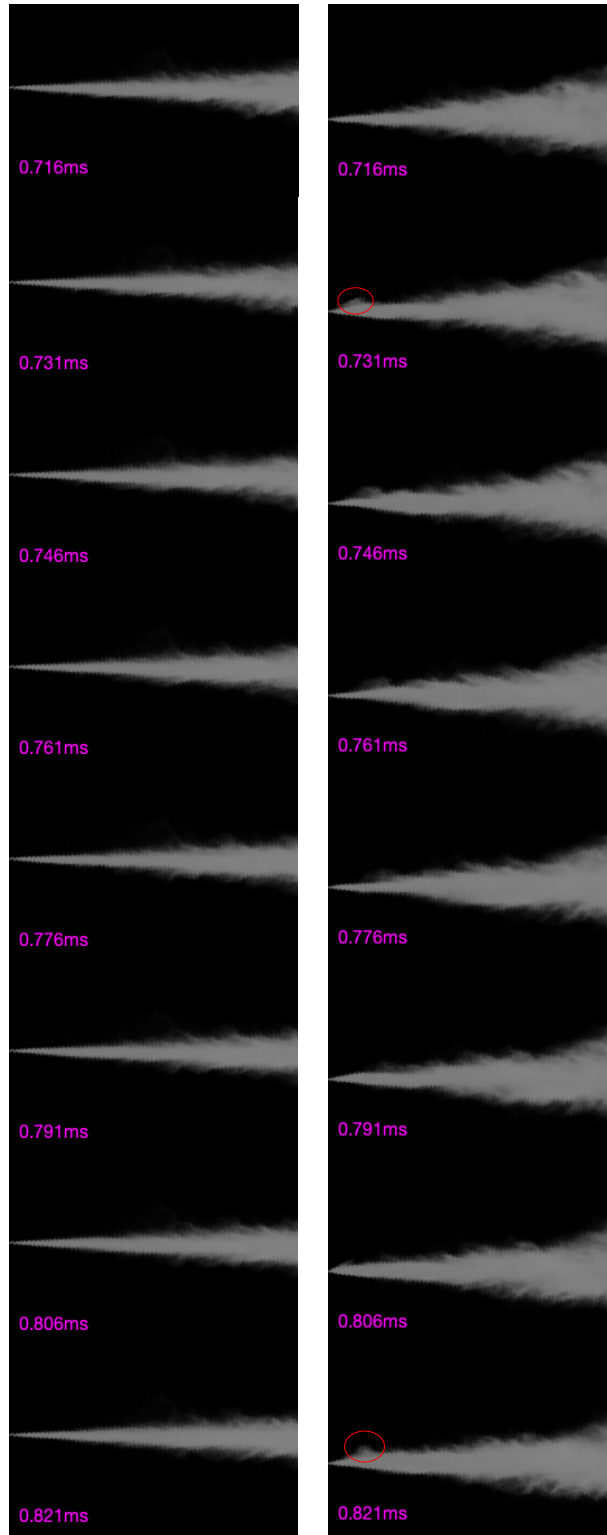


Figure 2.20. Image sequence of spray development from Injector C Hole 1 (right column) and Injector C Hole 2 (left column) for 1500 bar injection pressure and 1 bar chamber pressure. The red circles highlight observable changes in the size and symmetry of the spray angle from Hole 2.

## 2.4 Conclusion

The current work provides new data and associated understanding of high-pressure gasoline spray development for a wide range of conditions. For the experimental conditions considered, the gasoline spray development (quantified in terms of penetration distance, penetration rate, and spray angle) was a strong function of chamber pressure, and a weaker function of fuel injection pressure. For constant chamber pressure, the penetration rates at early times differed by 15-47% for different injection pressures. For constant injection pressure, the penetration rates at early times differed by 6-17% for different chamber pressures. Spray angle was a more complex function of operating conditions. The spray break-up time increased as a function of decreasing chamber pressure and injection pressure.

Comparison of spray measurements for the various internal nozzle geometries resulted in some notable trends and conclusions. Larger nozzle diameter, as well as the combination of a converging nozzle and hydroerosion rounding, resulted in increased penetration distance and spray angle. The nozzle with the smallest diameter consistently resulted in the lowest spray angle for all conditions tested, suggesting that the entrainment rates are lower and could lead to poor combustion. The diverging nozzle consistently produced the highest spray angle for all conditions tested, suggesting the opposite effect. The largest outlet diameter consistently had the highest penetration distance suggesting that fuel impingement and particulate emissions could be high during engine operation for this nozzle geometry.

Phenomena attributed to vapor pre-jets were observed with high frequency at the highest chamber pressures studied. No vapor pre-jets were observed at the lowest chamber pressures. The dependence on chamber pressure indicates the injector ingested chamber gases or the needle interacted with the sac volume. Current work includes trying to quantify the amount of fuel affected by the vapor pre-jet, in order to assess the potential effects on fuel mixing in an engine setting.

The sprays were observed to flutter (where the spray angle would occasionally asymmetrically increase and then return to a symmetric profile). The mean squared difference of the spray angle relative to the cycle-averaged spray angle was used to quantify the effect. The diverging nozzle with inlet rounding (Injector C Hole 1) and the large straight nozzle (Injector B Hole 2) exhibited higher variability in spray angle behavior compared with the other geometries studied. The conditions that exhibited the highest spray flutter were dependent on injector

geometry. Both holes with inlet rounding exhibited the highest flutter for the conditions with the largest pressure differentials between the fuel injection pressure and the chamber pressure. Both straight nozzles exhibited the highest flutter at the highest chamber pressure conditions. The combination of the injector geometry and the largest pressure differentials indicate the nozzles may have been experiencing significant cavitation affecting the external flow development.

## 2.5 Acknowledgements

The work presented here was funded in part by the Office of Energy Efficiency and Renewable Energy (EERE), U.S. Department of Energy (DOE), under Award Number DE-EE0006831, and Robert Bosch, LLC.

## Reference:

1. National Research Council, “Technologies for Reducing Fuel Consumption in Spark-Ignition Engines,” *Cost, Effectiveness, and Deployment of Fuel Economy Technologies for Light-Duty Vehicles*, The National Academies Press, Washington, D.C., ISBN 2012010415: 23–96, 2015.
2. Zhao, F., Lai, M.C., and Harrington, D.L., “Automotive spark-ignited direct-injection gasoline engines,” *Prog. Energy Combust. Sci.* 25(5):437–562, 1999, doi:10.1016/S0360-1285(99)00004-0.
3. Fraser, N., Blaxill, H., Lumsden, G., and Bassett, M., “Challenges for Increased Efficiency through Gasoline Engine Downsizing,” *SAE Tech. Pap.* (2009-01–1053), 2008, doi:10.4271/2009-01-1053.
4. Shaik, A., Moorthi, N.S.V., and Rudramoorthy, R., “Variable compression ratio engine: A future power plant for automobiles - An overview,” *Proc. Inst. Mech. Eng. Part D J. Automob. Eng.* 221(9):1159–1168, 2007, doi:10.1243/09544070JAUTO573.
5. Walsh, J., “VC-Turbo – the world ’ s first production-ready variable compression ratio engine,” 1–5, <https://global.nissannews.com/en/releases/vc-turbo-the-worlds-first-production-ready-variable-compression-ratio-engine>, 2017.
6. Saliba, G., Saleh, R., Zhao, Y., Presto, A.A., Lambe, A.T., Frodin, B., Sardar, S., Maldonado, H., Maddox, C., May, A.A., Drozd, G.T., Goldstein, A.H., Russell, L.M., Hagen, F., and Robinson, A.L., “Comparison of Gasoline Direct-Injection (GDI) and Port

- Fuel Injection (PFI) Vehicle Emissions: Emission Certification Standards, Cold-Start, Secondary Organic Aerosol Formation Potential, and Potential Climate Impacts,” *Environ. Sci. Technol.* 51(11):6542–6552, 2017, doi:10.1021/acs.est.6b06509.
7. Braisher, M., Stone, R., and Price, P., “Particle Number Emissions from a Range of European Vehicles,” *SAE Tech. Pap. Ser. 1(Ci)*, 2010, doi:10.4271/2010-01-0786.
  8. Stevens, E. and Steeper, R., “Piston Wetting in an Optical DISI Engine : Fuel Films , Pool Fires , and Soot Generation,” *SAE Tech. Pap.* (2001-01–1203), 2001, doi:10.4271/2001-01-1203.
  9. Berndorfer, A., Breuer, S., Piock, W., and Bacho, P. Von, “Diffusion Combustion Phenomena in GDi Engines caused by Injection Process,” *SAE International*, 2013, doi:10.4271/2013-01-0261.
  10. Fatouraie, M., Peterson, K., Biddappa, B., Livshiz, N., Larimore, J., and Mosburger, M., “Advanced Gasoline Combustion and Engine Controls,” *Reducing Particulate Emissions in Gasoline Engines*, SAE International, Warrendale: 103–114, 2018.
  11. Yao, C., Geng, P., Yin, Z., Hu, J., Chen, D., and Ju, Y., “Impacts of nozzle geometry on spray combustion of high pressure common rail injectors in a constant volume combustion chamber,” *Fuel* 179:235–245, 2016, doi:10.1016/j.fuel.2016.03.097.
  12. Park, S.H., Youn, I.M., Lim, Y., and Lee, C.S., “Influence of the mixture of gasoline and diesel fuels on droplet atomization, combustion, and exhaust emission characteristics in a compression ignition engine,” *Fuel Process. Technol.* 106:392–401, 2013, doi:10.1016/j.fuproc.2012.09.004.
  13. Eitel, F., Schäfer, J., Redante, E., Nolte, R., Königstein, A., and Heeger, C., “Potential and Challenges of Fuel Injection Pressure up to 50 MPa for Gasoline Direct Injection Engines,” *26th Aachen Colloq. Automob. Engine Technol. 2017 (Di)*:489–508, 2017.
  14. Jiang, C., Parker, M.C., Helie, J., Spencer, A., Garner, C.P., and Wigley, G., “Impact of gasoline direct injection fuel injector hole geometry on spray characteristics under flash boiling and ambient conditions,” *Fuel* 241(November 2018):71–82, 2019, doi:10.1016/j.fuel.2018.11.143.
  15. Merola, S.S., Irimescu, A., Tornatore, C., Marchitto, L., and Valentino, G., “Split Injection in a DISI Engine Fuelled with Butanol and Gasoline Analyzed through Integrated Methodologies,” *SAE Int. J. Engines* 8(2):474–494, 2015, doi:10.4271/2015-

- 01-0748.
16. Arsuaga, L.G.G., “Advanced Diagnostics for Spray Behavior , Fuel Impingement , and Soot Processes in Direct Injection Spark Ignition Engines,” Univeristy of Michigan, 2019.
  17. Su, J., Xu, M., Yin, P., Gao, Y., and Hung, D., “Particle Number Emissions Reduction Using Multiple Injection Strategies in a Boosted Spark-Ignition Direct-Injection (SIDI) Gasoline Engine,” *SAE Int. J. Engines* 8(1):20–29, 2014, doi:10.4271/2014-01-2845.
  18. Serras-Pereira, J., Aleiferis, P.G., and Richardson, D., “An experimental database on the effects of single- and split injection strategies on spray formation and spark discharge in an optical direct-injection spark-ignition engine fuelled with gasoline, iso -octane and alcohols,” *Int. J. Engine Res.* 16(7):851–896, 2015, doi:10.1177/1468087414554936.
  19. Paz, J., Staaden, D., and Kokjohn, S., “Gasoline Compression Ignition Operation of a Heavy-Duty Engine at High Load,” *SAE Tech. Pap.* 1–10, 2018, doi:10.4271/2018-01-0898.
  20. Yamaguchi, A., Koopmans, L., Helmantel, A., Karrholm, F.P., and Dahlander, P., “Spray Characterization of Gasoline Direct Injection Sprays Under Fuel Injection Pressures up to 150 MPa with Different Nozzle Geometries,” *SAE Tech. Pap. Ser.* 1:1–14, 2019, doi:10.4271/2019-01-0063.
  21. Medina, M., Fatouraie, M., and Wooldridge, M., “High-Speed Imaging Studies of Gasoline Fuel Sprays at Fuel Injection Pressures from 300 to 1500 bar,” *SAE Tech. Pap.* c(2018-01–0294):1–18, 2018, doi:10.4271/2018-01-0294.
  22. Payri, R., Viera, J.P., Gopalakrishnan, V., and Szymkowicz, P.G., “The effect of nozzle geometry over internal flow and spray formation for three different fuels,” *Fuel* 183, 2016, doi:10.1016/j.fuel.2016.06.041.
  23. Koo, J.Y., “The effects of injector nozzle geometry and operating pressure conditions on the transient fuel spray behavior,” *KSME Int. J.* 17(4):617–625, 2003, doi:10.1007/BF02984463.
  24. Naber, J. and Siebers, D.L., “Effects of Gas Density and Vaporization on Penetration and Dispersion of Diesel Sprays,” *SAE Tech. Pap.* (960034), 1996, doi:10.4271/960034.
  25. Siebers, D.L., “Liquid-Phase Fuel Penetration in Diesel Sprays,” *SAE Tech. Pap.* (980809), 1998, doi:10.4271/980809.
  26. Siebers, D.L., “Scaling Liquid-Phase Fuel Penetration in Diesel Sprays Based on Mixing-



- Limited Vaporization,” *SAE Tech. Pap.*, 1999, doi:10.4271/1999-01-0528.
27. Hiroyasu, H. and Arai, M., “Structure of Fuel Sprays in Diesel Engines,” *SAE Tech. Pap.* (900475), 1990, doi:10.4271/900475.
  28. Eagle, E.W., Morris, S.B., and Wooldridge, M., “High-speed imaging of transient diesel spray behavior during high pressure injection of a multi-hole fuel injector,” *Fuel* 116(0):299–309, 2014, doi:10.1016/j.fuel.2013.07.120.
  29. He, Z., Guo, G., Tao, X., Zhong, W., Leng, X., and Wang, Q., “Study of the effect of nozzle hole shape on internal flow and spray characteristics,” *Int. Commun. Heat Mass Transf.* 71:1–8, 2016, doi:10.1016/j.icheatmasstransfer.2015.12.002.
  30. Suh, H.K. and Lee, C.S., “Effect of cavitation in nozzle orifice on the diesel fuel atomization characteristics,” *Int. J. Heat Fluid Flow* 29(4):1001–1009, 2008, doi:10.1016/j.ijheatfluidflow.2008.03.014.
  31. Payri, R., García, J.M., Salvador, F.J., and Gimeno, J., “Using spray momentum flux measurements to understand the influence of diesel nozzle geometry on spray characteristics,” *Fuel* 84(5):551–561, 2005, doi:10.1016/j.fuel.2004.10.009.
  32. Bergstrand, P., Persson, F., Försth, M., and Denbratt, I., “A Study of the Influence of Nozzle Orifice Geometries on Fuel Evaporation using Laser-Induced Exciplex Fluorescence,” *SAE Tech. Pap. Ser. 1*, 2010, doi:10.4271/2003-01-1836.
  33. Nurick, W.H., “Orifice cavitation and its effect on spray mixing,” *J. Fluids Eng. Trans. ASME* 99(2):426–427, 1977, doi:10.1115/1.3448785.
  34. Crua, C., Heikal, M.R., and Gold, M.R., “Microscopic imaging of the initial stage of diesel spray formation,” *Fuel* 157:140–150, 2015, doi:10.1016/j.fuel.2015.04.041.
  35. Crua, C., Shoba, T., Heikal, M., Gold, M.R., and Higham, C., “High-speed microscopic imaging of the initial stage of diesel spray formation and primary breakup,” *SAE Int.* 28:1085–1092, 2010, doi:10.4271/2010-01-2247.
  36. Pickett, L.M., Manin, J., Payri, R., Bardi, M., and Gimeno, J., “Transient Rate of Injection Effects on Spray Development,” *SAE Int.* 6, 2013, doi:10.4271/2013-24-0001.
  37. Piehl, J. and Bravo, L., “Assessment of Cavitation Models for Computational Fluid Dynamics Analysis of Erosion Risk in a Hydrocarbon-Fueled Nozzle,” (September), 2018, doi:10.13140/RG.2.2.11744.12808.
  38. Soteriou, C., Andrews, R., and Smith, M., “Direct injection diesel sprays and the effect of

- cavitation and hydraulic flip on atomization,” *SAE Tech. Pap.* (412), 1995, doi:10.4271/950080.
39. Payri, F., Bermúdez, V., Payri, R., and Salvador, F.J., “The influence of cavitation on the internal flow and the spray characteristics in diesel injection nozzles,” *Fuel* 83(4–5):419–431, 2004, doi:10.1016/j.fuel.2003.09.010.
  40. Yue, Z., Battistoni, M., and Som, S., “A Numerical Study on Spray Characteristics at Start of Injection for Gasoline Direct Injection,” *14th Trienn. Int. Conf. Liq. At. Spray Syst.* 1–8, 2018.
  41. Desantes, J.M., Payri, R., Salvador, F.J., and La Morena, J. De, “Influence of cavitation phenomenon on primary break-up and spray behavior at stationary conditions,” *Fuel* 89(10):3033–3041, 2010, doi:10.1016/j.fuel.2010.06.004.

## Chapter 3

### **The Effects of Injector Geometry and Operating Conditions on Spray Mass, Momentum and Development at Evaporative and Non-evaporative Conditions**

Two of the high-pressure gasoline fuel injectors that were used in the constant volume chamber backlit imaging studies (Chapter 2) were further characterized to quantify the effects on internal features of the nozzles on spray mass, momentum and development. These studies were conducted using the facilities at the Universitat Politecnica de Valencia (UPV) in Spain and in collaboration with Professor Raul Payri and Jaime Gimeno, Ph.D. candidates Abian Bautista, Armando Moreno, Alberto Viera and technicians Omar Huerta Cornejo and Jose Enrique Del Rey.

#### **3.1 Experimental Methodology**

Two experimental facilities were used to measure the time-resolved mass flow rate and the time resolved momentum of the sprays from two of the canonical fuel injector nozzle geometries. A third high-temperature and high-pressure facility was used to measure the external spray development using high-speed schlieren imaging. The fuel properties of the gasoline used in the study are listed in Table 3.1 (no additional lubricity additive was used). The fuel differs slightly from the gasoline fuel utilized in experiments summarized in Chapter 2, primarily in the vapor pressure (11.8%) and research octane number (7.5%). All other properties exhibited less than 5% difference. For each of the measurements, the fuel was pressurized using a custom piston pump and supplied to the injector through a dual common rail system. Injection events were electronically controlled using an impulse generator (Genotec). The energize time for all injection events was set to 1 ms, similar to the experiments conducted in the Chapter 2, to simulate typical engine injector performance and to represent transient injector behavior. The injectors used in the study were Injectors B and C, previously described in Chapter 2 and Table 2.3.

Table 3.1 Fuel Properties

Property	Test Method	Value
Fuel type	-	Gasoline
Density 288 K [kg/m <sup>3</sup> ]	ASTM D4052	745.1
Reid vapor pressure [kPa]	ASTM D5191	69.7
Research octane number (RON)	ISO 5184	99
Motor octane number (MON)	ISO 5163	87.1
Heat of combustion [MJ/kg]	Gage-calculated	42.4
Distillation, IBP [K]	ASTM D86	306
Distillation, 10% [K]	ASTM D86	323
Distillation, 50% [K]	ASTM D86	370
Distillation, 90% [K]	ASTM D86	435

### 3.1.1 Instantaneous Mass Flow Rate Characterization

A commercially available Injection Rate Discharge Curve Indicator (IRDCI), which employs the Bosch method [1], was used to measure the instantaneous mass flow rate of the sprays from the injectors, i.e., the rate of injection (ROI). The IRDCI consists of a pressure transducer, a long fuel-filled tube, a large fuel reservoir, a relief valve, and a back-pressure cavity typically filled with nitrogen to reduce pressure oscillations. A schematic of the IRDCI is shown in Figure 3.1. Details on the fundamental working principle are provided in previous studies [1–4]. The functionality of the facility is briefly described here. Fuel is injected into the long tube which contains fuel at the start of the test. The fuel injection event produces a pressure wave that is proportional to the instantaneous mass flow rate. The pressure wave is detected using a fast-response piezoelectric pressure sensor. The underlying theory is based on the hydraulic pulse theorem [1–4]. To account for uncertainties in the measurement, fuel is collected at the outlet of the IRDCI at the same rate at which fuel is being added to the reservoir (which is labeled “Release volume” in Figure 3.1). The fuel is collected on a mass balance, serving as a second mass flow rate measurement and for comparison with the IRDCI pressure-based measurements. The experimental error associated with the IRDCI measurements of fuel mass flow rate is less than 0.6% [5–7].

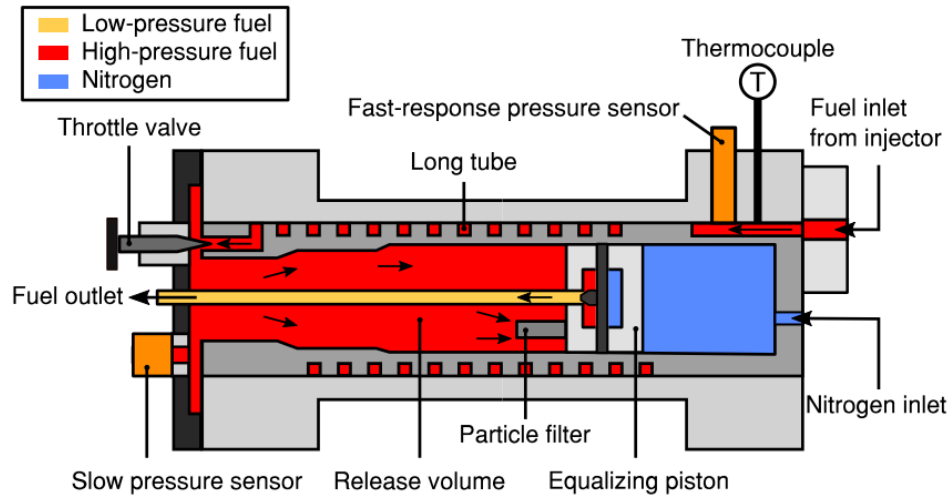


Figure 3.1. Schematic of injection rate meter including the main components [4]

For each IRDCI experiment, the injector is placed in a cooling jacket that is fixed at the entrance of the IRDCI. The cooling jacket provides a continuous flow of temperature-controlled coolant. Two coolant temperatures, four injection pressures and three back pressures were tested and are listed in Table 3.2. Two sets of data with 50 repetitions each were collected at each condition. The first data set was used to verify stability and repeatability, and the second data set was used for analysis.

Table 3.2. Summary of Experimental Conditions

Parameter	Facility		
	IRDCI	Momentum Flux	CPF Reactor
Chamber gas	-	Nitrogen	Nitrogen
Fuel type	Reference gasoline		
Injector Tested	B and C (see Table 2.3)		
Injection Pressures [bar]	600, 900, 1200, 1500		
Chamber Pressure [bar]	10, 20 30	5, 10, 20, 30	5, 10, 20, 30
Chamber Temperature [K]	293	293	400, 600, 800
Coolant Temperature [K]	293, 363	363	293, 363
Number of repetitions	100	100	20

### 3.1.2 Instantaneous Momentum Characterization

The momentum rate meter is a custom-designed enclosed vessel with high-pressure chamber capabilities and optical access. The underlying assumptions and details of the system are presented in previous studies [8,9]. A schematic of the spray momentum rate meter is provided in Figure 3.2. A brief summary of the operation is provided here. For a typical

experiment, the chamber is pressurized with nitrogen to conditions consistent with the injection timing of the piston engine of interest. Momentum measurements are acquired using a piezoelectric sensor aligned perpendicular to the axis of the fuel spray. Only one spray plume is allowed to impact the sensor in the tests. As shown in Figure 3.2, the impact force of the spray plume is directly related to the axial momentum flux of the spray.

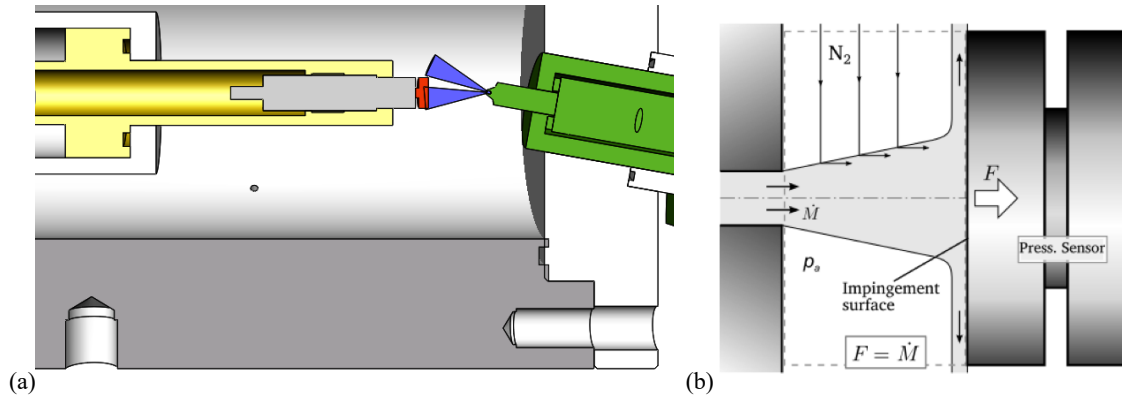


Figure 3.2. (a) Side cut plane of the momentum rate meter vessel with color-coded parts. Jets are shown in blue. The injector is shown in green. The sensor impingement surface is shown in red, and the sensor fixture is shown in yellow. (b) A conceptual schematic of the spray momentum measurement principle [8].

For the current work, the sensor target area was placed 8 mm from the nozzle outlet. This was the minimum distance to ensure no interference between the two plumes. A small distance also avoids potential losses from the spray due to atomization and evaporation. Similar to the IRDCI tests, two data sets of 50 measurements each were recorded. Four fuel injection pressures, four chamber pressures, and one coolant temperature were tested. The complete list of conditions is provided in Table 3.2.

### 3.1.3 High-speed imaging characterization

Figure 3.3 is a schematic of the custom-designed, high-temperature, high-pressure test facility used to image the gasoline spray development. A detailed description of the facility is presented in Bardi [5]. A brief summary of the facility and the experimental approach is provided here. The facility is a constant-pressure flow (CPF) reactor with the ability to create nearly quiescent and steady thermodynamic conditions [10]. During an experiment, the chamber is continuously pressurized with nitrogen to simulate engine conditions and has three orthogonal optical access ports each with viewing access of 12.8 cm. The chamber is rated to a maximum

temperature of 1000 K and a maximum pressure of 150 bar. The operating conditions used in the reactor experiments are listed in Table 3.2.

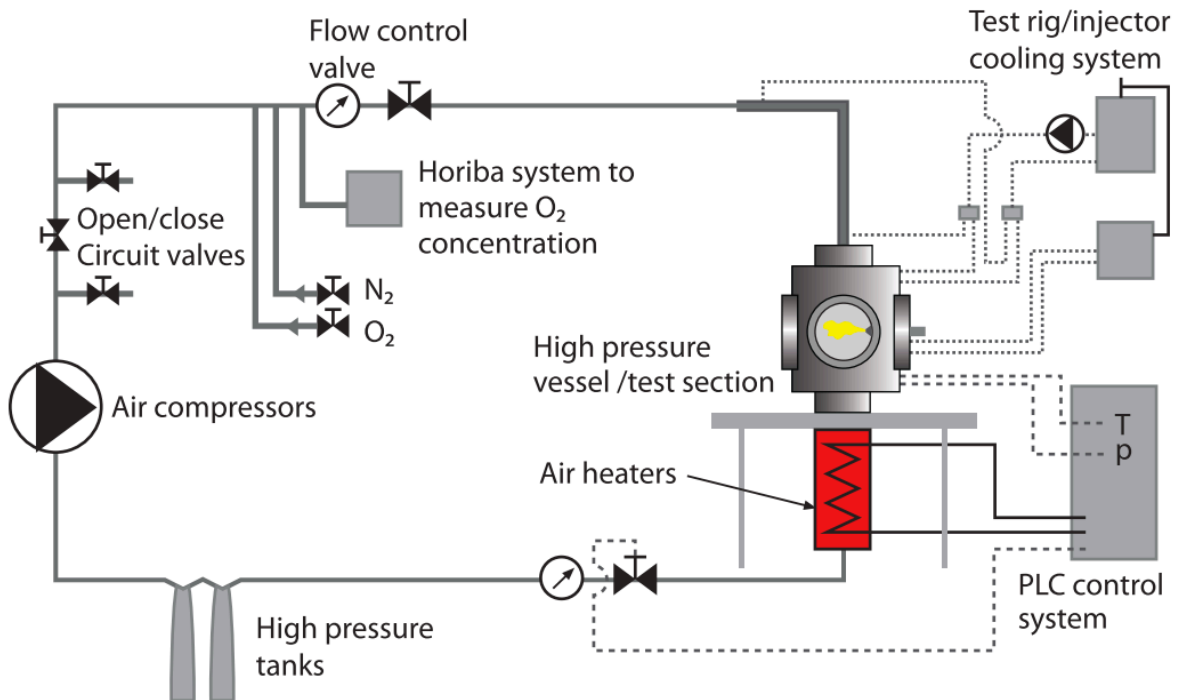


Figure 3.3. Schematic for the high temperature high pressure test chamber including the gas flow equipment, the heating and cooling system, and the control system [5]

Schlieren imaging has been used extensively to visualize spray development [11–14]. The imaging technique used in this study was a single pass schlieren setup. A schematic of the optical arrangement is shown Figure 3.4. The technique consists of a light source, collimating mirror, focusing lens, diaphragm, and camera. The light from a mercury-xenon arc lamp is passed through a pin-hole with a diameter of 1.2 mm. The light is reflected from a 150 mm parabolic mirror with a focal length of 650 mm, collimating the light through the test section. After passing through the test section, the light is focused with a 150 mm biconvex lens onto a diaphragm placed at the focal point of 450 mm. The diaphragm is set to a diameter of 4 mm and in front of the high-speed camera (Photron Fastcam SA5). The images were recorded using a 100 mm lens (Zeiss) with the camera and the settings listed in Table 3.3.

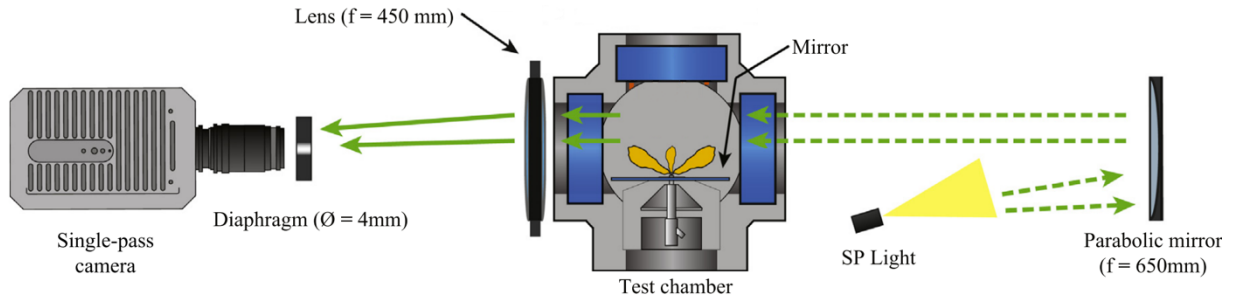


Figure 3.4. Schematic of the single-pass schlieren optical setup applied to the high-temperature, high-pressure flow reactor imaging studies. The green arrows indicate the light path. Adapted from Payri et al. [14].

Table 3.3 Summary of camera settings used with the schlieren flow reactor imaging

Setting	Value
Frame Rate [fps]	65,100
Exposure Time [ $\mu$ s]	3.95
Lens aperture [f/#]	5.6
Camera resolution [pixel x pixel]	256x300
Image resolution [pixel/mm]	6.9

### 3.1.4 Data Processing

The data collected in the three facilities were processed using methods specific to each experimental approach. Details are provided in several references [6,7,9,12,15], and the approaches are briefly reviewed here.

The IRDCI data from all 50 injection events were averaged and converted to mass flow rates/ROI, including corrections for signal bias, using the methods described in Bosch et al. [1], and Payri et al. [6]. The ROI data are then integrated to obtain the total injected mass. The calculated mass is compared with the measured mass from the IRDCI mass balance. Using both measurements, a scaling factor is determined and used to correct the IRDCI measurements. Examples of corrected ROI signal are shown in Figure 3.5 along with the integrated mass, indicated by the shaded area. For each time-history of mass flow rate, a region was selected for analysis after the start of injection and before the end of injection, where the injection rate was relatively stable as a function of time. For this study, the time interval was at least 0.5 ms after the start of injection and for a duration of  $\sim 0.25$  ms (shown with vertical dashed lines in Figure 3.5). The ROI data in this region were mathematically averaged and identified as the characteristic injection rate for each experiment. The ROI data were then used to calculate hydraulic coefficients such as the momentum coefficient, discharge coefficient, and area



coefficient for each injector. Variability in the time interval selected for analysis is considered in the uncertainty of the hydraulic coefficients determined from the data.

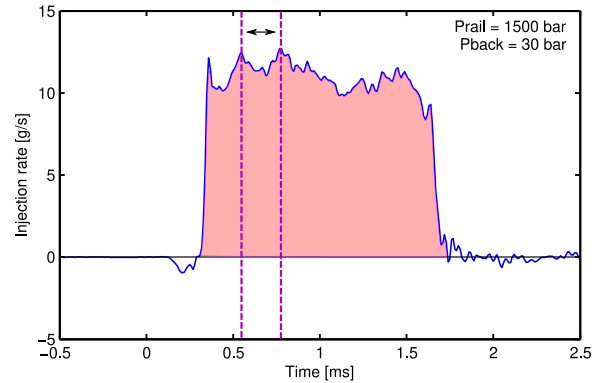


Figure 3.5. Results for average injection rate for 1500 bar injection pressure and 30 bar back pressure for Injector 2. The data include the mass from both nozzle holes of the injector. The shading represents the total mass per injection event. Vertical dashed lines indicate the region of the ROI data used to determine the hydraulic coefficients for the injector.

The force measurement is equivalent to the momentum flux as shown in the previous work by Gimeno and Payri et al. [8,9]. The characteristic momentum flux value is determined similar to the characteristic ROI. The average momentum flux is calculated and a time region after the measurement has stabilized is assigned as the representative flux for the operating conditions tested. Figure 3.6 shows an example of the momentum flux measurement where the stabilized range is indicated with vertical dashed lines.

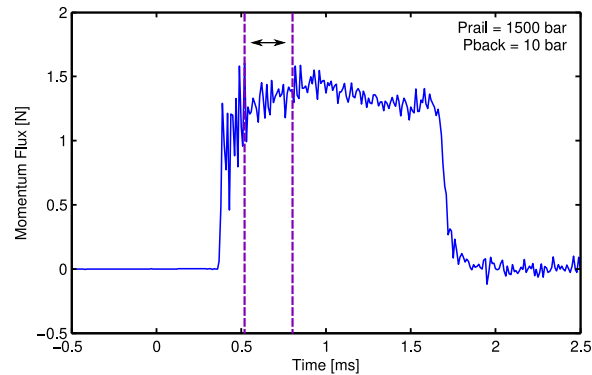


Figure 3.6. Average corrected momentum flux measurement for 1500 bar injection pressure and 10 bar chamber pressure. Vertical dashed lines indicate stabilized region.

The high-speed schlieren images were used to quantify the spray development in terms of spray tip penetration and spray angle. The image processing included four major steps: image masking, background subtraction, contour detection, and contour analysis. The image masking was determined by defining the general area where the sprays were located. This was done using the centerline axis of the spray and the maximum anticipated width of the spray, creating a segmented triangular shape. An example of masking is shown in Figure 3.7.

To perform accurate background subtraction for the schlieren images, two algorithms were implemented: dynamic background subtraction and image temporal derivative. The effects of applying the algorithms for background subtraction are shown in Figures 3.7. Briefly summarizing each algorithm, the dynamic background subtraction creates an image by mathematically summing two images (the previous raw image and the previous binary image with the original background) and differencing the results with the current image to remove the background data. The image temporal derivative is a pixel-wise standard deviation of the current frame with two previous frames. The algorithms complement each other because the dynamic background captures a majority of the dense regions of the spray, whereas the image temporal derivative captures the dilute fluid regions. The final image after applying both algorithms are presented in Figure 3.7. More details on the image processing algorithms can be found in previous literature [4,12,14,16].

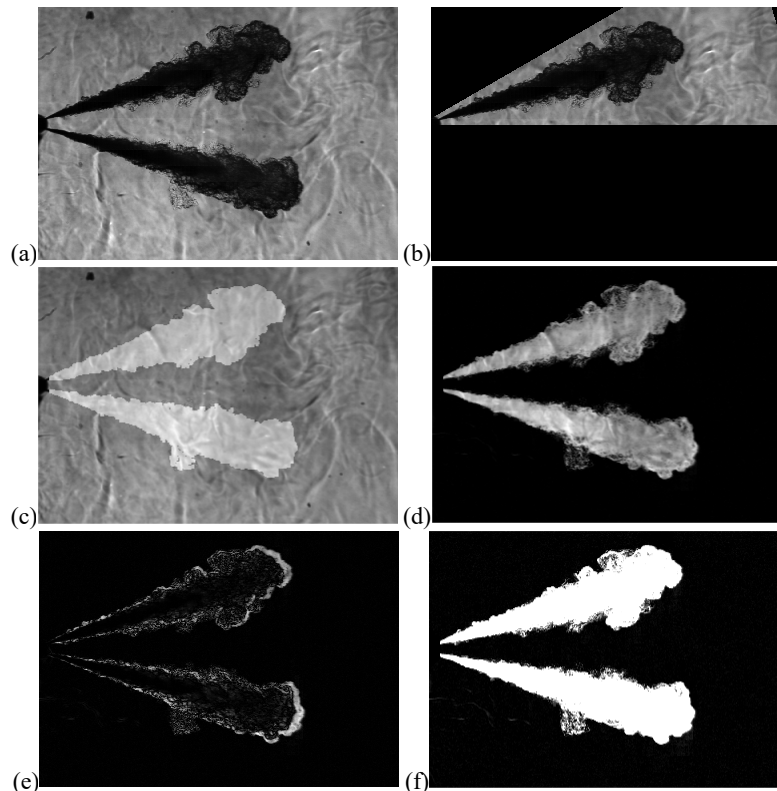


Figure 3.7. Schlieren image processing steps for Injector C for an injection pressure of 1500 bar and a chamber density of  $8.44 \text{ kg/m}^3$  (corresponding to a chamber temperature of 800 K and a chamber pressure of 20 bar). (a) original image at time step  $i$  (b) masking applied to isolate hole 1 (c) summation of images at time step  $i$  and  $i-1$  used for background subtraction (d) resulting image from background subtraction at time step  $i$  (e) temporal derivative of  $i$ th frame, using frames at  $i-1$ , and  $i-2$ , (e) final image after background subtraction using the two algorithms and conversion from gray scale to binary image.

Once each spray had been isolated, contour detection was performed using binary images. The spray boundaries were a function of the threshold value used during the conversion to binary images. The threshold was determined by multiplying a dynamic range to a fixed value, adjusting for individual image luminosity [16,17], and the uncertainty in the derived spray features due to image processes was determined. Any background features incorrectly assigned as part of the fuel spray during the background subtraction process were removed through erosion-dilation and pixel connectivity criteria. Additional details on the application of the algorithms to schlieren image processing can be found in [4,14,16]. Spray tip penetration distance, and spray angle were calculated for each time step using the contours from the processed images. The spray tip penetration distance was measured as the distance from the origin of the spray to the spray pixel located at the maximum distance along the plume axis. Spray angle was defined as the angle at one-third the penetration distance of the spray.

## 3.2 Results

The experimental matrix of the study spanned a wide range of operating conditions and several nozzle geometries in the three facilities. In the interest of conciseness, representative data are presented in the following sections. The results at other conditions followed similar trends unless specified otherwise. The additional data from the different facilities and experimental conditions are presented in the Appendix for reference.

### 3.2.1 Mass Flow Rate

Figure 3.8 shows the injection rate results for two coolant temperatures (20 °C and 90 °C) for Injector C at 1500 bar injection pressure and 20 bar chamber pressure. The averages are shown as solid lines and the standard deviations of 50 repetitions are shown as the shaded regions. All the injection events were programmed with the IRDCI controller to use the same trigger signal and the same injection duration of 1 ms. However, the mass flow rate data all showed the actual injection duration was longer, with total times ranging from 1.5 to 2 ms. In addition, the mass flow rate data in Figure 3.9 show the coolant temperature of 90° C resulted in a slightly longer injection event than the lower temperature conditions. The other portions of the injection event were very similar, with similar opening time and similar profile for the majority of the event. For the data presented in Figure 3.8, the higher coolant temperature resulted in a

0.067 ms longer injection event, corresponding to about 1 mg more fuel injected after the end of injection compare with the lower temperature condition. Comparison of the total mass injected for the two conditions (determined by integrating the injection rate data) showed ~2 mg difference or 9%. The differences between the two masses are an indication of the small differences in the injection rate profiles at the different coolant temperatures. The integrated mass for a majority of the conditions tested showed the higher coolant temperature yielded between 1% and 4% more fuel primarily due to longer injection events. Figure 3.8 shows the case with the highest difference in integrated mass.

One explanation for this trend may be related to fuel viscosity. Higher temperatures result in lower viscosity, thus reducing the viscous forces required to close the needle at the end of injection. Salvador et al. [18] noticed the same behavior with diesel fuel for multiple injection durations and injection pressures. Salvador et al. [18] proposed that lower viscous forces at lower temperatures reduce the maximum needle lift, such that the needle closes from a lower position at lower temperatures. This reduces the time needed to close the injector. Similar behavior was noticed with dimethyl ether and increasing fuel temperature [19]. The fuel temperature affects viscous forces and mechanical operation of the needle impacting the injection duration. However, the amount of additional fuel mass injected at higher temperatures would depend on the fuel viscosity.

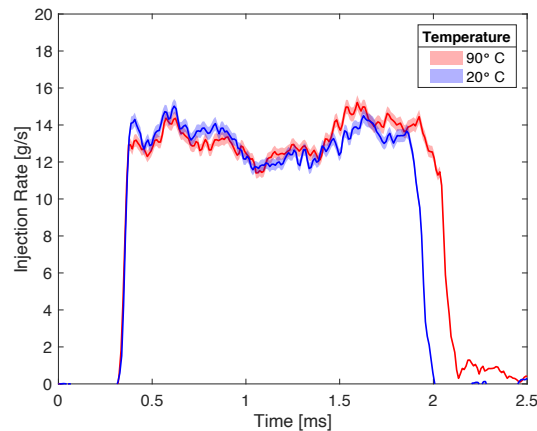


Figure 3.8. Average fuel injection rate for two coolant temperatures for Injector C Holes 1 and 2 at 1500 bar injection pressure and 20 bar chamber pressure

Figure 3.9 shows the effects of three chamber pressures at 1500 bar injection pressure for Injector C. The injection rate results are similar for the three chamber pressures, with differences occurring only during the opening events. Lower chamber pressure exhibited a large spike in

injection rate during the opening event, particularly for higher injection pressures. This behavior may be due to the limit of the dynamic response of the IRDCI, because the lowest rated chamber pressure for the system is 10 bar and the measurements exhibit more noise at 10 bar chamber pressure. Excluding the variation at the start of injection, the results show chamber pressure has negligible effect on injector mass flow rate, which is consistent with previous studies of other fuels and injectors [1,8,20].

Figure 3.10 shows the effects of injection pressure at 30 bar chamber pressure for Injector C with 20° C coolant temperature. As expected, increasing fuel injection pressure increased the fuel mass flow rate for the same injection timing due to higher flow velocities. In addition, higher injection pressures resulted in slightly earlier end of injection. This trend was consistent across chamber pressures and injectors tested at lower coolant temperatures. However, when the coolant temperature was increased to 90° C, the needle opening and closing events were almost identical for most conditions. This trend may be attributable to the fuel viscosity. As discussed, earlier higher temperatures result in lower viscosity thus reducing the viscous forces required to close the needle at the end of injection regardless of injection pressure. However, there was one exception for the data at higher coolant temperatures for Injector C at an injection pressure of 600 bar. At these conditions, the mass flow rate data indicate later needle closing.

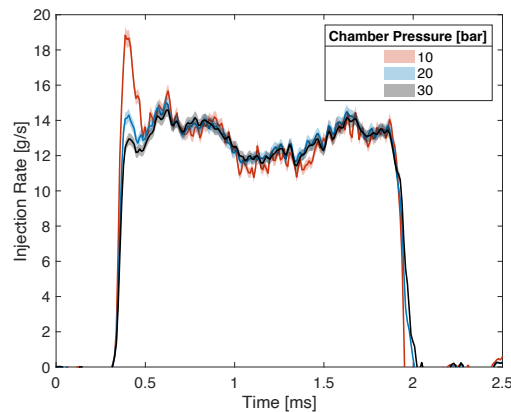


Figure 3.9. Average injection rate for Injector C at 20° C coolant temperature at 1500 bar injection pressure for three chamber pressures

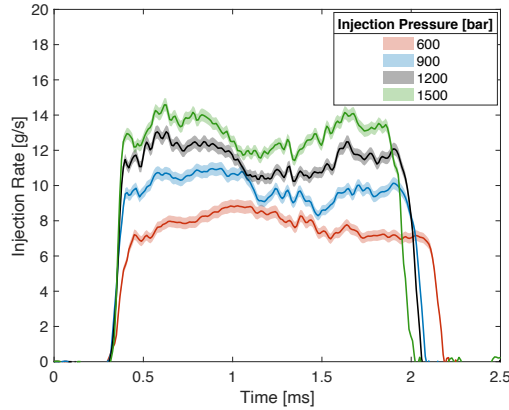


Figure 3.10. Average injection rate for Injector C at 20° C coolant temperature at 30 bar chamber pressure for four injection pressures

The hydraulic parameter for each nozzle were determined from the mass flow rate and momentum flux measurements. The average value for each measurement was used for the analysis to determine the momentum coefficient, discharge coefficient, effective area, and effective outlet velocity. All the coefficients are derived from first principles, and details and assumptions are provided in the references [3,8,9,20].

Figures 3.11 presents the ROI results for both injectors tested at 90° C for all injection and chamber pressures as a function of  $(\Delta P)^{1/2}$ , where  $\Delta P$  is the difference between the fuel injection pressure and the chamber pressure. The data show, as expected based on Bernoulli's approximation for flow velocity, that ROI is linearly proportional to  $(\Delta P)^{1/2}$  and that Injector C consistently produced a higher mass flow rate compared with Injector B. Recall, the differences between Injector B and Injector C are the conicity, inlet hole rounding of the nozzles and nozzle diameters. Injector B has two cylindrical nozzles, one with a slightly larger diameter and one with a slightly smaller diameter than the nozzles of Injector C. Note the total physical nozzle outlet diameter (and therefore total nozzle outlet area) for each injector is the same. So the trends may be attributed to the effects of rounding the nozzle inlet (Injector C) and uniform (Injector B) versus converging/diverging nozzle channel (Injector C). The mass flow rates for Injector B were consistently lower than the mass flow rates of Injector C, by 10% to 19%, with the smallest difference observed at injection pressures of 600 bar and the highest difference observed at injection pressures of 1200 bar. Assuming the conicity effects are offsetting, the results indicate rounding has a measurable impact on mas flow rate.

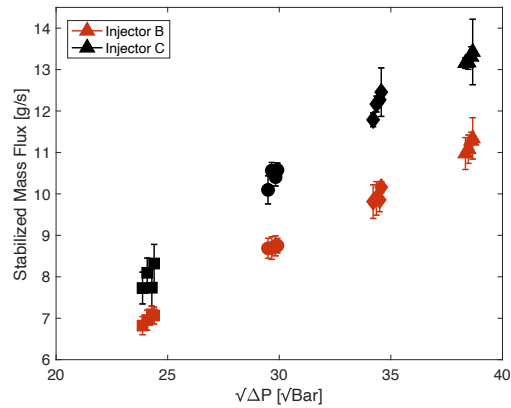


Figure 3.11. Average mass flux for both injectors. All operating conditions are shown at 90° C coolant temperature.

### 3.2.2 Momentum Flux

The momentum flux results for Injector C Hole 2 at 1200 bar injection pressure and 90° C coolant temperature are presented in Figure 3.12 for four chamber pressures. The results are virtually identical for all chamber pressures, which is consistent with expectations based on the theory and principles used to design the facility [8]. Briefly, as long as the sensor is placed a reasonable distance from the orifice and orthogonal to the spray, the momentum of the jet is unaffected by the chamber density.

Figure 3.13 presents the effects of injection pressure on the momentum flux at 5 bar chamber pressure for the same injector nozzle and coolant temperature. The main observation is that the momentum flux increases with increasing injection pressure. Higher variability in the momentum measurement is observed for higher chamber pressures for all injection pressures.

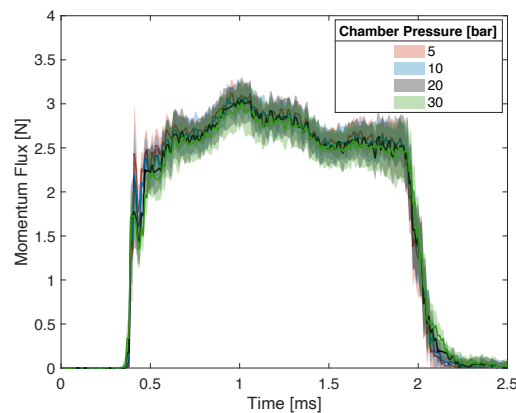


Figure 3.12. Average momentum flux measurements for Injector C Hole 2 at 90° C coolant temperature at injection pressure of 1200 bar for four chamber pressures

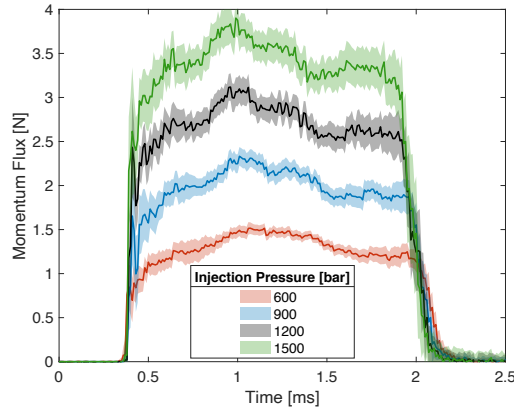


Figure 3.13. Average momentum flux measurements for Injector C Hole 2 at 90° C coolant temperature at 5 bar chamber pressure for four injection pressures

Figure 3.14 presents the results for the momentum flux measurements as a function of  $\Delta P$ , and, like the mass flow rate measurements, the results show linear dependence. Here the momentum flux data are resolved to the level of the individual nozzles of the injectors. Injector B Hole 2, with the largest outlet diameter, resulted in the highest momentum flux at all test conditions. At the opposite end of the results, Injector B Hole 1, with the smallest outlet diameter, resulted in the smallest momentum flux at all test conditions. The intermediate results for Injector C Holes 1 and 2, were close to the values for the largest nozzle diameter, Injector B Hole 2. While the differences between the momentum flux results of the largest three orifices may appear small, they were as high as 9% for some conditions. Between Injector C Holes 1 and 2, the differences ranged between 7 to 9% for all conditions. Injector C Holes 1 and 2 have the same outlet diameter but differ in conicity. Injector C Hole 2 has a converging nozzle resulting in higher outlet velocities compared with Injector C Hole 1, which is reflected in the momentum flux data. Overall, the trends indicate the size of the nozzle outlet diameter has a stronger effect on momentum flux than conicity or hydro-erosion rounding.

The trends in average momentum flux measurements shown in Figure 3.14 can be used to explain the effects of injector geometry on the spray characteristics presented in Chapter 2. For example, in Figure 2.12, Injector B Hole 2 had higher penetration distance, penetration rate and spray angle compared with Injector B Hole 1. The higher penetration distance and rate can be attributed to the higher momentum flux, which is a product of the internal geometries induced flow.



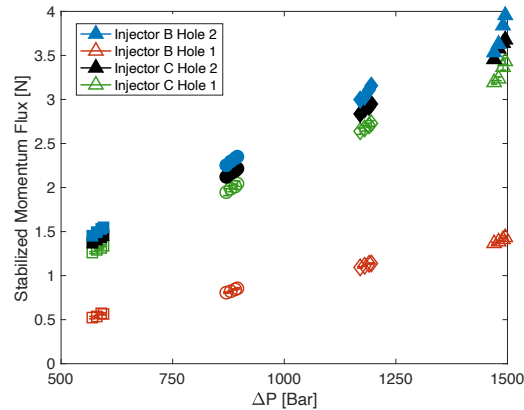


Figure 3.14. Average momentum flux for all four orifices. All operating conditions are shown at 90° C coolant temperature.

The theoretical momentum flux can be calculated using  $\Delta P$  and the Bernoulli principle and compared with the experimental data. The ratio between the measured momentum and theoretical momentum flux can be calculated to obtain the momentum coefficient for each nozzle. The momentum coefficient results are shown in Figure 3.15 for the four orifices. Two trends are observed. The first key conclusion from Figure 3.15 is the relative performance of the different injector geometries. Both nozzles with hydro-erosion rounding (Injector C) resulted in the highest momentum coefficients. Hydro-erosion rounding is used to reduce the amount of flow separation, and the results show rounding does improve the nozzle performance; more closely approximating the theoretical value. Injector C Holes 1 and 2 have the same outlet diameters, but with diverging and converging nozzle passages, respectively. The data show the larger inlet diameter associated with the converging nozzle of Injector C Hole 2 further reduces flow separation compared with the diverging nozzle. The uniform cross-section/cylindrical nozzles both exhibited lower momentum coefficients, which is attributed to increased flow separation.

The second observation is that the momentum coefficient is independent of Reynolds number. Under cavitating conditions the discharge coefficient only depends on the cavitation number and not the Reynolds number [9,21,22]. During cavitation, a recirculation zone is created in the nozzle forming a vena contracta effect. This reduces the effective area of the nozzle and the mass flow rate, decreasing the actual momentum compared with the theoretical momentum. Although some of the nozzle geometries included features to reduce the probability of cavitation, such as the hydro-erosion rounding of the nozzle inlet of Injector C Hole 2, all nozzles exhibited this behavior at 90° C coolant temperature. The fuel properties of gasoline combined with the

trends observed with the momentum coefficient as a function of high Reynolds number support the conclusion that the nozzle flows experience cavitation.

Figure 3.16 shows the momentum coefficient as a function of cavitation number for the four orifices. The cavitation number is defined based on the study by Nurick [22]. All four orifices show a decreasing trend with increasing cavitation number. Various studies have suggested that once cavitation appears, the discharge coefficient is only dependent on cavitation number and practically independent on Reynolds number [9,22–24]. Additionally, the same studies state that large cavitation numbers suggest non-cavitating flow while small cavitation numbers (close to 1) correspond to strong cavitating flow. The statements are with respect to discharge coefficient and Figure 3.16 shows the momentum coefficient. However, the discharge coefficient and the momentum coefficient are linearly dependent suggesting that under cavitating conditions, the momentum coefficient is dependent on the cavitation number.

External spray features such as spray flutter observed and discussed in section 2.3.3 support the conclusion that the flow is cavitating. Spray flutter was suspected to be a product of surface roughness, machining defects and/or cavitation. Cavitation was considered more likely due to the fuel volatility and the operating conditions. Therefore, many factors indicate the flow is cavitating at all operating conditions for all orifices. To summarize, the downstream external spray features such as spray flutter, the high-pressure fuel injection that results in small cavitation numbers (close to 1), the fuel volatility, and the negative trend with increasing cavitation number all suggest that the nozzles are experiencing cavitation. This is an important conclusion that should be considered when interpreting the other spray measurements and when considering injector design for high-pressure gasoline sprays.

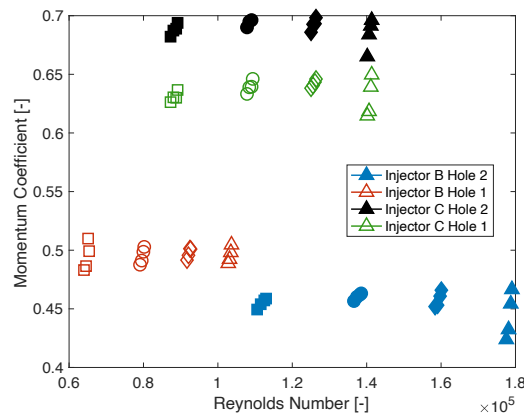


Figure 3.15. Momentum coefficient results for the four orifices of Injectors B and C at 90° C coolant temperature as a function of Reynolds number.

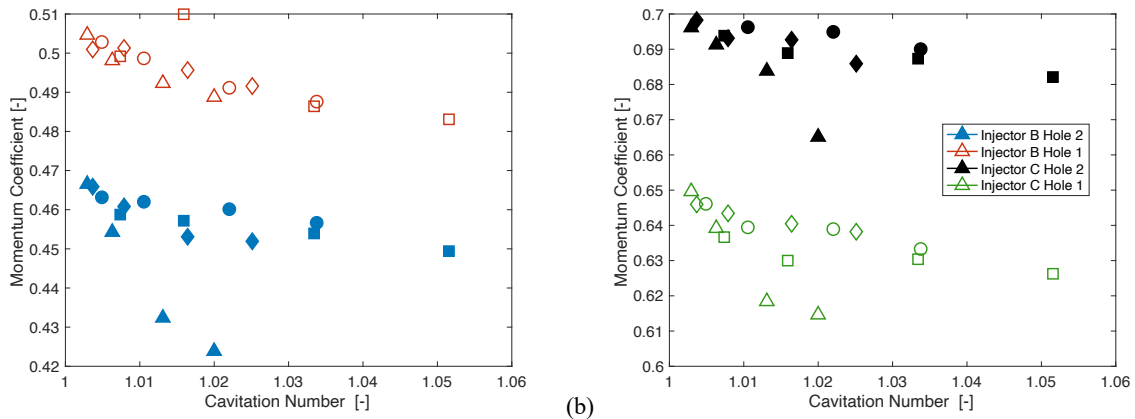
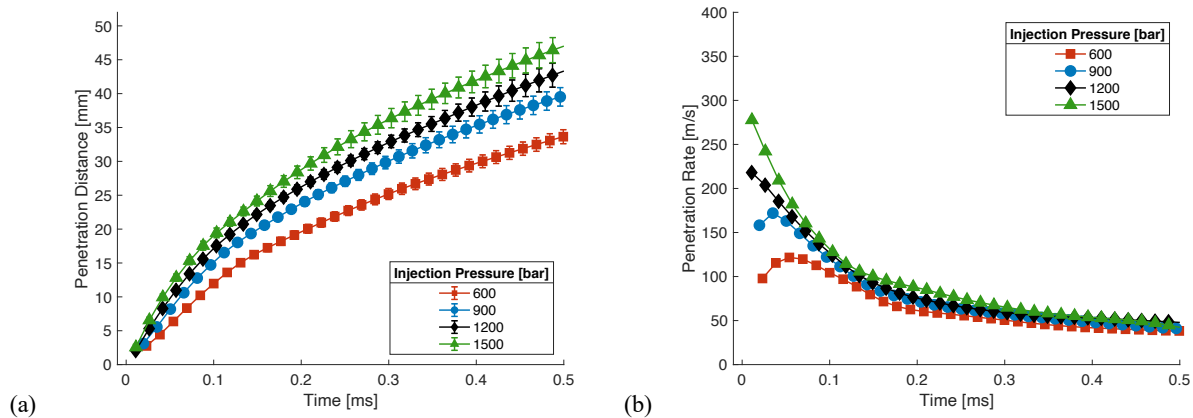
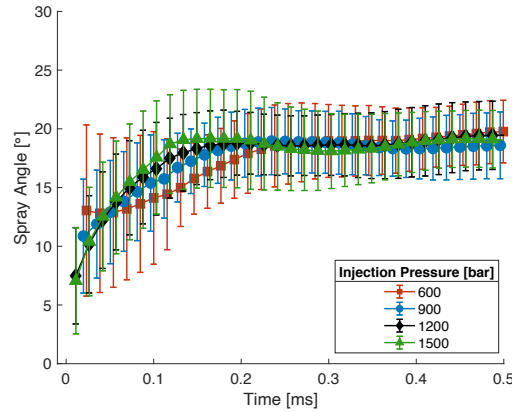


Figure 3.16. Momentum coefficient results for the four orifices of (a) Injector B and (b) Injector C at 90° C coolant temperature as a function of cavitation number

### 3.2.3 Macroscopic Spray Development

Results from analysis of the schlieren images are presented in Figure 3.17 for 800 K chamber temperature and 30 bar chamber pressure (chamber density of 12.63 kg/m<sup>3</sup>) for Injector B Hole 2 and 90° C coolant temperature. The data include the spray tip penetration distance, spray tip penetration rate, and spray angle. Since the results are based on schlieren imaging, the data include the vapor-phase portions of the fuel spray. The data in Figure 3.16 are averages of 20 repetitions with error bars that signify one standard deviation. The trends observed here are similar to the results obtained from the shadowgraph images presented in the previous chapter. Increasing injection pressure produced higher penetration distances. Higher injection pressures resulted in higher maximum penetration rates; however, at later times the penetration rate was similar for the different injection pressures. The spray angle measurements showed no sensitivity to injection pressures, as previously reported.





(c) Figure 3.17. Results for spray development for Injector B Hole 2 at 800 K chamber temperature, 30 bar chamber pressure (density 12.63 kg/m<sup>3</sup>) and 90° C coolant temperature. (a) average penetration distance (b) average penetration rate and (c) average spray angle

Several chamber temperatures and pressures were tested resulting in 12 total combinations and nine chamber densities from 2.11 to 25.27 kg/m<sup>3</sup>. Three chamber densities were repeated but using a combination of different chamber conditions. Figure 3.18 shows the average penetration distance for Injector B Hole 1 at 1500 bar injection pressure and 90° C coolant temperature for the 12 chamber conditions. In the figure, the data are clustered in three groupings with similar penetration behavior. The groupings are due to the different chamber pressures. The fastest penetration data are from the experiments with 5 bar chamber pressure. The slowest penetration data are from the highest chamber pressures of 20 and 30 bar. The smaller differences in the penetration distances within each group are due to the different chamber temperatures. Amongst the same chamber pressure data, the highest temperature results in the farthest penetration due to the lower chamber density. Interestingly, the penetration and spray angle data from the three identical pairs of densities differ (4.21, 8.42 and 16.9 kg/m<sup>3</sup>), as seen in Figure 3.18. This trend shows the chamber pressure has a stronger effect on spray penetration distance than chamber temperature, particularly for lower chamber pressures. Also interesting is the penetration distance time histories for 12.6 and 16.9 kg/m<sup>3</sup> were identical, as seen in the inset of Figure 3.18. This behavior was observed for all nozzles and all injection pressures.

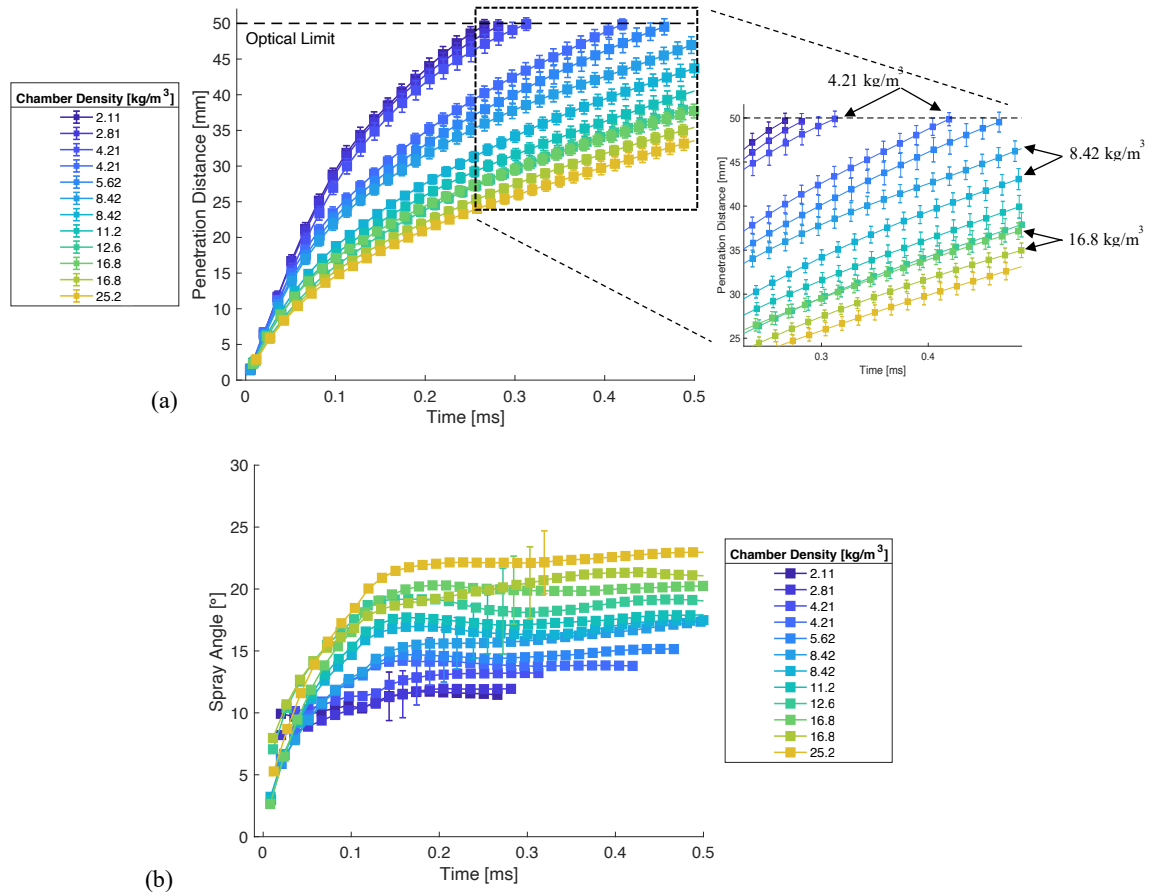


Figure 3.18. (a) Average penetration distance and (b) average spray angle for Injector B Hole 1 at 1500 bar injection pressure and 90° C coolant temperature for 12 chamber density conditions.

At lower injection pressures, the groupings of data were more pronounced, with greater division between the penetration distances, as seen in Figure 3.19 for Injector C Hole 1 at 600 bar injection pressure. The effects of temperature were smaller at lower chamber pressures, with more overlapping data. However, small differences are still observed between identical chamber densities.

The grouping of the results observed in Figure 3.18 and 3.19 could be a product of the fuel properties that were studied for the first time in this dissertation. For example, Payri et al. [25] studied the spray characteristics of n-dodecane and n-heptane in a constant pressure flow reactor. Payri reported that for the same chamber density, a change of 200 K in chamber temperature did not result in any difference in the penetration distance data. However, Naber and Siebers [26] studied diesel spray characteristics in a CVC at various chamber conditions and reported that for the same chamber density, increasing chamber temperature resulted in a reduced penetration distance. The diesel spray characteristics of penetration distance for the same density

are similar to the trends explored in this dissertation with gasoline. Both diesel and gasoline are multicomponent fuels while the fuels studied in Payri et al. [25] were single component fuels. Therefore, a key conclusion is that the fuel composition and properties affect the spray characteristics sufficiently to cause visible impact on spray penetration.

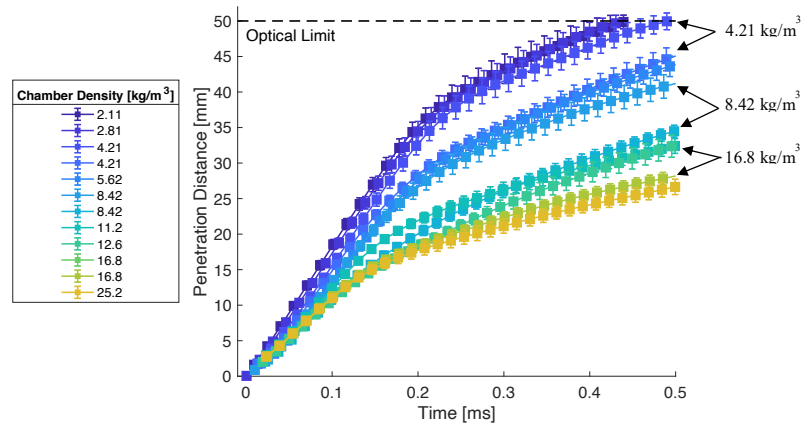


Figure 3.19. Average penetration distance for Injector C Hole 2 at 600 bar injection pressure and 90° C coolant temperature for 12 chamber density conditions.

Figure 3.20 compares penetration distance time histories for all nozzles at 1500 bar injection pressure tested in the CPF reactor and the UM CVC. At early times ( $< \sim 0.1$  ms), the data are identical. At later times, Injector C Hole 2 and Injector B Hole 1 have the fastest penetration with very similar results. In some cases, the penetration distance of Injector C Hole 1 is also overlapping. However, in all cases Injector B Hole 1 had the lowest penetration distance. The trends are consistent with the momentum flux results for the different injector hole geometries. The nozzle with the smallest exit diameter with cylindrical conicity produced the lowest mass flow rate and lowest momentum flux causing the lowest penetration distance. Conversely, the larger diameter and/or the combined effect of a converging nozzle with hydro-erosion resulted in higher flow velocities, reduced flow separation, and increased mass flow rates and momentum.

Similar trends have been reported for other fuel spray studies. Particularly, Sasaki et al. [27] studied the penetration distance for two nozzles using DME in a high temperature environment. Sasaki reported that both nozzles, a converging nozzle with inlet rounding and a larger diameter nozzle, had the same penetration despite the converging nozzle with inlet rounding showing higher flow rates. In this dissertation work, the momentum measurements supported the trends noticed in penetration distance. Although the spray characteristics of DME

and gasoline are vastly different, some similarities are observed for the effects of injector geometry.

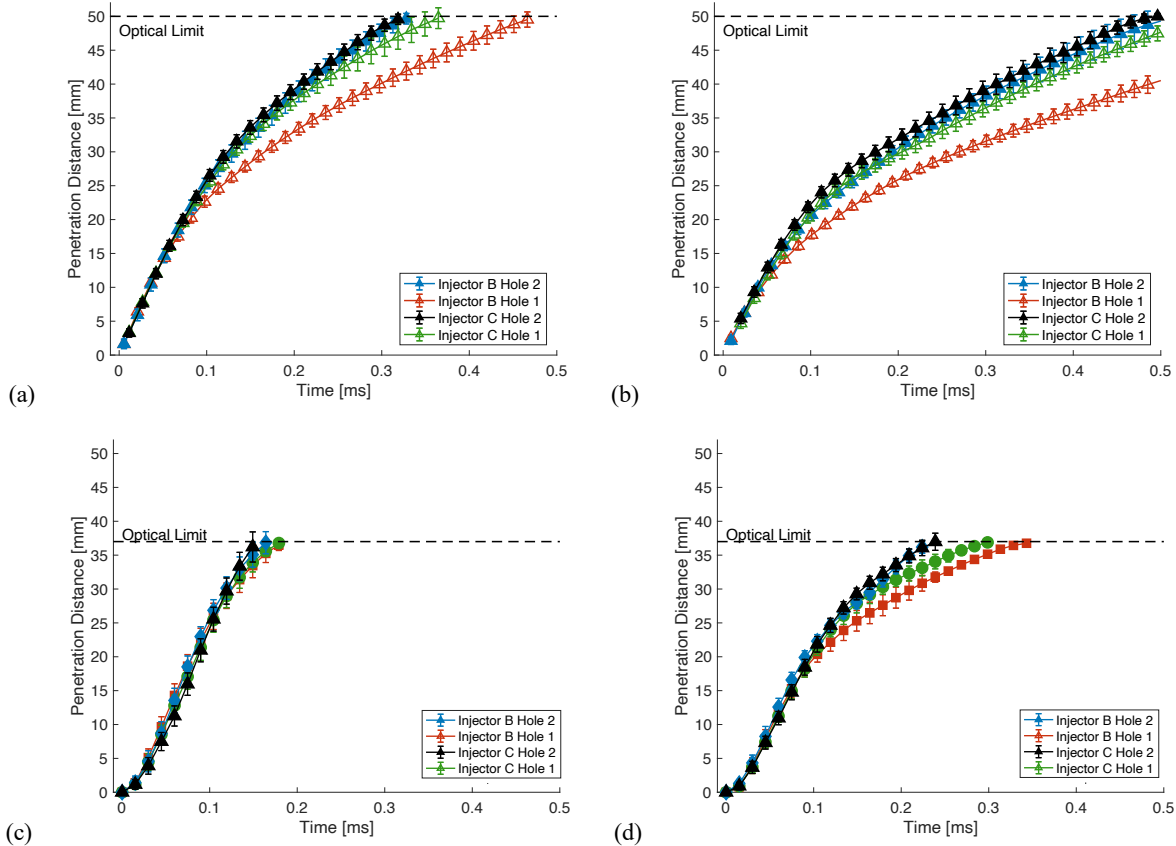


Figure 3.20. Average penetration distance for all nozzles at 1500 bar injection pressure tested in CPF (top row) and at UM CVC (bottom row). (a) 600 K chamber temperature and 10 bar chamber pressure, density of  $5.62 \text{ kg/m}^3$  (b) 600 K chamber temperature and 20 bar chamber pressure, density of  $11.2 \text{ kg/m}^3$  (c) 300 K chamber temperature and 5 bar chamber pressure, density of  $5.65 \text{ kg/m}^3$  (d) 300 K chamber temperature and 10 bar chamber pressure, density of  $11.33 \text{ kg/m}^3$

### 3.3 Conclusions

Three facilities were used to measure mass flow rate, momentum flux and spray development. The major conclusions based on the results are:

- Injector temperature had a noticeable effect on the injection rate. Temperature is suspected to affect fuel viscosity impacting needle opening and closing events. For a majority of the cases, higher coolant temperature led to 1% to 4% more fuel injected per event.
- Internal injector geometry played a considerable role on internal flow dynamics and hydraulic behavior. The mass injection data showed hydro-erosion rounding and conicity increased the mass flow rate between 10-19% compared with cylindrical/uniform cross-

section nozzles. The momentum data showed larger nozzle diameters and converging and rounded inlet nozzles could be used to achieve similar momentum fluxes, with differences of less than 6% in momentum flux between these two nozzle geometries.

- The data showed all nozzles were cavitating, regardless of injector temperature, nozzle geometry, chamber pressure and injection pressure, as determined by the decreasing momentum coefficient trend. Cavitation could be a cause of component damage and can affect fuel flow rates, mixing and atomization.
- In agreement with previous spray visualization studies, chamber pressure had a strong effect on spray penetration, more so than chamber temperature and the combined parameter of chamber density.
- While nozzle geometry had no effect on the early portion of the spray development, nozzle geometry significantly influenced spray development at later times (e.g., after the spray break-up time), producing similar trends as those observed with the momentum flux measurements.

### 3.4 Acknowledgements

The work was made possible through a collaboration with the Engine Research Division, Centro Motores Termicos at Universitat Politecnica de Valencia. I would like to offer special thanks to the faculty, technicians and graduate students that contributed their time and expertise to the collection and analysis of this chapter content.

### Reference

1. Bosch, W., "The Fuel Rate Indicator: A New Measuring Instrument For Display of the Characteristics of Individual Injection," *SAE Tech. Pap. Ser. 1*, 1968, doi:10.4271/660749.
2. la Morena, J. de, "Estudio de la Influencia de las Caracteristicas del Flujo Interno en Tobera sobre el Proceso de Inyeccion Diesel en Campo Proximo," Universitat Politecnica de Valencia, 2011.
3. Salvador, F.J., Gimeno, J., Carreres, M., and Crialesi-Esposito, M., "Fuel temperature influence on the performance of a last generation common-rail diesel ballistic injector. Part I: Experimental mass flow rate measurements and discussion," *Energy Convers. Manag.* 114:364–375, 2016, doi:10.1016/j.enconman.2016.02.042.



4. Viera, A., "Effect of multiple injection strategies on the diesel spray formation and combustion using optical diagnostics," 2019.
5. Bardi, M., "Partial Needle Lift and Injection Rate Shape Effect on the Formation and Combustion of the Diesel Spray," 2014.
6. Payri, R., Salvador, F.J., Gimeno, J., and Bracho, G., "A new methodology for correcting the signal cumulative phenomenon on injection rate measurements," *Exp. Tech.* 32(1):46–49, 2008, doi:10.1111/j.1747-1567.2007.00188.x.
7. Viera, J.P., "Experimental study of the effect of nozzle geometry on the performance of direct-injection diesel sprays for three different fuels," Universitat Politècnica de Valencia, 2017, doi:10.4995/Thesis/10251/81857.
8. Gimeno, J., "Desarrollo y aplicación de la medida del flujo de cantidad de movimiento de un chorro diesel," 2008.
9. Payri, R., García, J.M., Salvador, F.J., and Gimeno, J., "Using spray momentum flux measurements to understand the influence of diesel nozzle geometry on spray characteristics," *Fuel* 84(5):551–561, 2005, doi:10.1016/j.fuel.2004.10.009.
10. Meijer, M., Somers, B., Johnson, J., Naber, J., Lee, S.Y., Malbec, L.M., Bruneaux, G., Pickett, L.M., Bardi, M., Payri, R., and Bazyn, T., "Engine Combustion Network (ECN): Characterization and comparison of boundary conditions for different combustion vessels," *At. Sprays* 22(9):777–806, 2012, doi:10.1615/AtomizSpr.2012006083.
11. Parrish, S.E., "Evaluation of Liquid and Vapor Penetration of Sprays from a Multi-Hole Gasoline Fuel Injector Operating Under Engine-Like Conditions," *SAE Tech. Pap. 2014-04-01* 7(2):1017–1033, 2014, doi:10.4271/2014-01-1409.
12. Pastor, J.V., Payri, R., Garcia-oliver, J.M., and Nerva, J., "Schlieren Measurements of the ECN-Spray A Penetration under Inert and Reacting Conditions," *SAE Int.*, 2012, doi:10.4271/2012-01-0456.
13. Skeen, S.A., Manin, J., and Pickett, L.M., "Simultaneous formaldehyde PLIF and high-speed schlieren imaging for ignition visualization in high-pressure spray flames," *Proc. Combust. Inst.* 35(3):3167–3174, 2015, doi:10.1016/j.proci.2014.06.040.
14. Payri, R., Salvador, F.J., Bracho, G., and Viera, A., "Differences between single and double-pass schlieren imaging on diesel vapor spray characteristics," *Appl. Therm. Eng.* 125:220–231, 2017, doi:10.1016/j.applthermaleng.2017.06.140.

15. Payri, R., Gimeno, J., Bardi, M., and Plazas, A.H., "Effect of Injection Rate Shaping Over Diesel Spray Development in," *ASME 2012 Intern. Combust. Engine Div. Spring Tech. Conf.* 1–10, 2012, doi:<https://doi.org/10.1115/ICES2012-81206>.
16. Payri, R., Gimeno, J., Bracho, G., and Vaquerizo, D., "Study of liquid and vapor phase behavior on Diesel sprays for heavy duty engine nozzles," *Appl. Therm. Eng.* 107:365–378, 2016, doi:[10.1016/j.applthermaleng.2016.06.159](https://doi.org/10.1016/j.applthermaleng.2016.06.159).
17. Siebers, D.L., "Liquid-Phase Fuel Penetration in Diesel Sprays," *SAE Tech. Pap.* (980809), 1998, doi:[10.4271/980809](https://doi.org/10.4271/980809).
18. Salvador, F.J., Gimeno, J., Carreres, M., and Crialesi-Esposito, M., "Fuel temperature influence on the performance of a last generation common-rail diesel ballistic injector. Part I: Experimental mass flow rate measurements and discussion," *Energy Convers. Manag.* 114:364–375, 2016, doi:[10.1016/j.enconman.2016.02.042](https://doi.org/10.1016/j.enconman.2016.02.042).
19. Guangxin, G., Zhulin, Y., Apeng, Z., Shenghua, L., and Yanju, W., "Effects of Fuel Temperature on Injection Process and Combustion of Dimethyl Ether Engine," *J. Energy Resour. Technol.* 135(4):1–5, 2013, doi:[10.1115/1.4023549](https://doi.org/10.1115/1.4023549).
20. Payri, R., Gimeno, J., Marti-aladaravi, P., and Vaquerizo, D., "Internal Flow Characterization on an ECN Injector," *At. Sprays* 26(9):889–919, 2015, doi:[10.1615/atomizspr.2015013930](https://doi.org/10.1615/atomizspr.2015013930).
21. Benajes, J., Pastor, J.V., Payri, R., and Plazas, A.H., "Analysis of the Influence of Diesel Nozzle Geometry in the Injection Rate Characteristic," *J. Fluids Eng.* 126(1):63, 2004, doi:[10.1115/1.1637636](https://doi.org/10.1115/1.1637636).
22. Nurick, W.H., "Orifice cavitation and its effect on spray mixing," *J. Fluids Eng. Trans. ASME* 99(2):426–427, 1977, doi:[10.1115/1.3448785](https://doi.org/10.1115/1.3448785).
23. Sun, Y., Guan, Z., and Hooman, K., "Cavitation in Diesel Fuel Injector Nozzles and its Influence on Atomization and Spray," *Chem. Eng. Technol.* 42(1):6–29, 2019, doi:[10.1002/ceat.201800323](https://doi.org/10.1002/ceat.201800323).
24. He, Z., Guo, G., Tao, X., Zhong, W., Leng, X., and Wang, Q., "Study of the effect of nozzle hole shape on internal flow and spray characteristics," *Int. Commun. Heat Mass Transf.* 71:1–8, 2016, doi:[10.1016/j.icheatmasstransfer.2015.12.002](https://doi.org/10.1016/j.icheatmasstransfer.2015.12.002).
25. Payri, R., Viera, J.P., Gopalakrishnan, V., and Szymkowicz, P.G., "The effect of nozzle geometry over internal flow and spray formation for three different fuels," *Fuel* 183, 2016,

doi:10.1016/j.fuel.2016.06.041.

26. Naber, J. and Siebers, D.L., “Effects of Gas Density and Vaporization on Penetration and Dispersion of Diesel Sprays,” *SAE Tech. Pap.* (960034), 1996, doi:10.4271/960034.
27. Sasaki, S., Kato, M., Yokota, T., Konno, M., and Gill, D., “An Experimental Study of Injection and Combustion with Dimethyl Ether,” *SAE Tech. Pap.* 2015-April(April), 2015, doi:10.4271/2015-01-0932.

## Chapter 4

# Mechanisms of Fuel Injector Tip Wetting and Tip Drying Based on Experimental Measurements of Engine-Out Particulate Emissions from Gasoline Direct Injection Engines

*This chapter was accepted to the International Journal of Engine Research as Medina, M., Alzahrani, F., Fatouraie, M., Wooldridge, M., Volker, S., “Mechanisms of Fuel Injector Tip Wetting and Tip Drying Based on Experimental Measurements of Engine-Out Particulate Emissions from Gasoline Direct Injection Engines”, February 2020*

### 4.1 Introduction

Emissions standards for gasoline direct-injection (GDI) engines are becoming more stringent around the world. Particulate emissions regulations, which include particulate mass (PM) limits, are trending towards particulate number (PN) criteria. For example, in 2014 PN standards were introduced in Europe for GDI engines with a limit of  $6 \times 10^{12}$  particles/km, which was lowered by an order of magnitude in 2017 to the current limit of  $6 \times 10^{11}$  particles/km [1], and the same limit must be met by 2020 in China [2]. In the U.S., phase-in of the 3 mg/mi PM emission standard was applied in 2017, which will be lowered to 1 mg/mi in California during 2025-2028 [3]. Many studies between 2009 and 2017 report PM and PN levels for GDI vehicles of 0.2 – 10 mg/mi and  $6 \times 10^{11}$  –  $2 \times 10^{13}$  particles/km, respectively [4–6] for the new European drive cycle (NEDC). This shows that PN limits are more challenging to meet than the limits for PM and identifying and mitigating the sources of PN for GDI engines is therefore critical to meet future emissions targets.

The sources of particulates from engines are attributed to fuel-rich combustion regions formed during fuel and air mixing, liquid films created by fuel spray impingement, fuel trapped in crevice volumes, and other mechanisms [7–10]. Pool fires can be created when liquid-phase fuel impinges on surfaces, including the piston crown, intake and exhaust valves, and cylinder walls [11–13]. Some operating strategies and design criteria [14] can help reduce and sometimes eliminate fuel rich zones, such as late fuel injection or multiple fuel injection events [12,15,16].

However, one surface wetting mechanism that cannot be avoided by injection strategy and is not well understood is injector tip wetting. Injector tip wetting occurs when the fuel injection event creates liquid-phase fuel films or droplets on the tip of the fuel injector. Figure 4.1 shows schematics of the fuel flow leading to tip wetting in a GDI injector nozzle and the important features used to describe the internal geometry of a GDI injector nozzle.

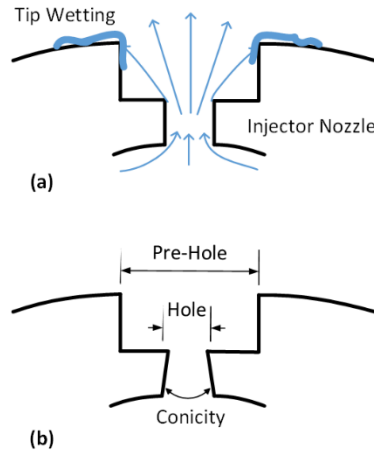


Figure 4.1 Schematics of the (a) general fuel flow leading to injector tip wetting in GDI engines, and (b) the basic internal features of GDI injector nozzle design. [17]

Injector tip wetting and tip drying have important effects on particulate emissions from GDI engines, and at some conditions, combustion of fuel on the injector tip has been shown to be a significant source of particulates. For example, Berndorfer et al. [18] used in-cylinder imaging to identify and quantify luminescence from diffusion flames originating from the fuel injector tip of a large bore single-cylinder GDI engine. The large bore was used to reduce the effects of wall and piston wetting by the fuel spray. The injector diffusion flame imaging data were quantified and compared with experimental measurements of engine-out PM and PN. The diffusion flame results correlated well with the particulate measurements, leading the authors to conclude that combustion of the fuel on the injector tip was the dominant source of particulate emissions, whereas combustion of the bulk charge was not.

Similarly, Dageforde et al. [19] investigated the spray behavior including wall impingement, tip wetting, and PN emissions for injectors with different internal geometries using different measurement techniques. The main differences in injector geometry were the pre-hole diameters and orifice inlets (see **Error! Reference source not found.b**). When tested in a GDI engine, the authors observed a significant difference in PN emissions after a 20-hour endurance test for an injector with a smaller pre-hole diameter. The smaller pre-hole diameter decreased

the penetration distance of the spray, reducing the likelihood of wall impingement of the fuel as visualized in a constant-volume chamber. Further testing using long distance microscopy revealed the smaller pre-hole diameter also resulted in qualitatively lower tip wetting. The authors concluded the significant improvement in PN emission was likely caused by the reduction in tip wetting from the pre-hole design modification.

Leick et al. [20] studied tip wetting using both experimental and computational methods for gasoline sprays. Flash boiling and non-flash boiling operating conditions were compared to study the spray structure for a single injector. Simulations and constant volume chamber experiments helped understand differences in spray behavior between the different operating conditions. Flash boiling sprays resulted in faster fuel vaporization and wider spray plumes at the orifice outlet. The wider spray plumes caused an interaction with the pre-hole surfaces resulting in tip wetting. However, engine experiments revealed that flash boiling decreased PN emissions under certain operating conditions, and increased PN emissions for other operating conditions. The improvements in vaporization rates and worsening tip wetting could not be decoupled from the PN measurements in this engine study. However, in a related study on flash boiling, Leick et al. [21] used laser-induced fluorescence to quantify the tip wetting area and height for different injector geometries and operating conditions. The results showed that flash boiling and injection pressure were the biggest factors affecting tip wetting. Changes in injector geometry did not reveal significant effects on tip wetting, contrary to what was found in Dageforde et al. for changes in injector geometry and PN emissions[19].

The different stages of tip wetting during the engine cycle were visualized in a single-cylinder engine using various imaging setups by Peterson et al. [22]. Using windows located in the engine head, near nozzle images were obtained to identify the mechanisms that led to excessive tip wetting. The three primary mechanisms identified were related to excessive plume width, large droplets at the end of injection, and remnant fuel in the injector sac volume. The three mechanisms were correlated with injector fouling and subsequently correlated with increased PN emissions.

The extensive library of literature available within the diesel fuel injection community has also helped inform conceptual understanding of gasoline fuel injector tip wetting; specifically, literature related to droplet formation during and at the end of injection. Highlighting work from Eagle et al.[23], where a taxonomy for fuel dribble in diesel injection

was investigated; the study incorporated high-speed imaging, two camera positions, five injectors, two fuels and various operating conditions. The large experimental matrix helped relate five physical processes to fuel dribble: (1) Injector dynamics (most likely due to improper sealing and needle bounce), (2) Gases ingested into the injector nozzle, (3) Fuel compressibility, (4) Dissolved gases in the fuel, and (5) Different fuel flow between injector orifices due to differences in orientation. The three distinct characteristics of fuel dribble were identified as: (1) Immediate dribble that happens after the end of injection, (2) Late-cycle dribble that occurs during the expansion stroke due to fuel vapor condensation, and (3) Blow-down dribble that occurs during exhaust valve opening due to in-cylinder charge motion stripping liquid deposits from the injector tip and sac. However, no relationship between fuel dribble and the role it has on tip wetting PN in diesel injectors was described in the work by Eagle et al.[23], probably because diffusion flames during fuel injection is the major source of particulate emissions in diesel engines.

A key process that mitigates tip wetting is tip drying, i.e. the evaporation of the fuel film deposited onto the injector tip from tip wetting. Understanding the mechanisms of injector tip drying is vital to reduce tip wetting and the resulting PN emissions. Karwa et al.[24] investigated the effects of ambient pressure, tip temperature and air flow velocity on tip drying rate in a controlled lab experiment using isooctane fuel. The authors identified two thermal mechanisms and a mass convection mechanism for tip drying. The difference between the thermal mechanisms was based on the temperature difference between the injector tip and the fuel boiling point. The first thermal mechanism, known as single-phase evaporation, was significant for tip temperatures up to 10°C higher than the boiling point, i.e. superheat of 10°C. For tip temperatures higher than a superheat of 10°C, the main thermal mechanism was controlled by boiling. The mass convection drying mechanism was represented using a constant airflow to simulate piston induced charge motion. By varying the conditions of the flow around the injector tip, the authors were able to evaluate the relative importance of the different drying mechanisms. The authors reported that air flow was important only for the single-phase evaporation mechanism, where air flow caused increased evaporation rate. For the boiling regime, the results showed no discernable sensitivity due to air flow.

Fischer and Thelliez [25] performed three-dimensional (3-D) computational fluid dynamics engine simulations of isooctane film formation and evaporation on an injector tip. The

results showed fuel and tip temperatures were the most important parameters controlling film formation and evaporation, with fuel temperature having higher impact than tip temperature. Higher flow velocities showed lower fuel film mass at the end of the injection event. However, charge motion did not influence fuel film evaporation. This led the authors to conclude that charge motion is important only during injection, where it affects the film distribution on the injector tip.

Tip wetting studies often use single-component fuels so the fuel properties can be considered well known, but the properties of single-component fuels can differ significantly from real fuel properties. To understand the evaporation behavior of real fuels, Stanglmaier et al. [26] measured the lifetime of droplets over a hot plate for Howell EEE certification gasoline at different system pressures. The certification gasoline was insensitive to pressure for surface temperatures below 160 °C. For higher system pressures, the certification gasoline did not exhibit Leidenfrost behavior associated with boiling evaporation.

Much has been learned from the previous work on tip wetting of gasoline fuel injectors; however, few studies have focused on relating spark-ignition engine operating conditions and injector hardware directly to the physical and chemical mechanisms controlling injector tip wetting and tip drying. While production engines at actual operating conditions are complex environments, much can be learned in terms of relating the observed trends in PN emissions with expected trends based on the physical mechanisms that have been proposed for tip wetting and tip drying. Consequently, the objective of this work was to identify trends in engine-out PN emissions for a broad range of engine and fuel injector operating conditions and relate the trends to physical mechanisms for tip wetting and tip drying. A brief review of the conceptual understanding of tip wetting and tip drying is presented, followed by the experimental details and approach. The experimental results are discussed in terms of the relative significance of the tip wetting and drying mechanisms.

## **4.2 Conceptual Understanding of GDI Fuel Injector Tip Wetting and Tip Drying**

### **Mechanisms**

The physical mechanisms that lead to injector tip wetting can be grouped into three categories. The first is the fuel deposited on the injector nozzle tip *during the injection process*. The second is the fuel deposited on the nozzle tip *at the end of injection event via droplets*,



*ligaments, and low momentum flow.* The third category is the fuel deposited on the nozzle tip from the *liquid and vapor inside the sac volume of the injector.* Two processes have been identified that contribute to injector tip wetting during injection. First, as the fuel flows through the nozzle hole and into the pre-hole (see **Error! Reference source not found.**), the fuel flow path widens. Depending on the geometry, flow dynamics, and operating conditions, the fuel flow interacts with the pre-hole wall and some of the fuel deposits on the surface of the wall and then flows around the corner and onto the outlet of the orifice. The flow-through deposition process is shown schematically in Figure 4.2. As described earlier, Leick et al. [21] investigated tip wetting using laser-induced fluorescence and concluded that one of the most important conditions affecting injector tip wetting was flash boiling. Flash boiling is known to cause the spray plume to widen and under certain cases cause spray collapse [27,28]. Since flash boiling affects plume width, it subsequently impacts injector tip wetting. This nozzle wetting mechanism is described here as wide-plume wetting. As shown in Figure 4.2, wider plumes lead to more tip wetting compared with narrower plumes.

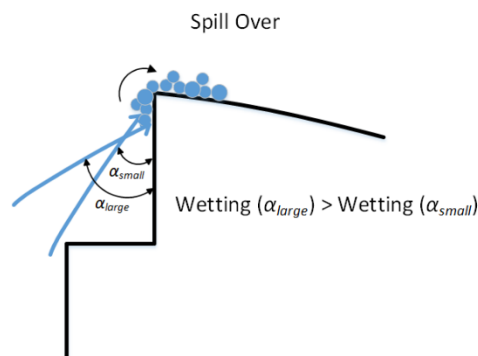


Figure 4.2: Schematic of the wide-plume tip-wetting process caused by fuel impingement on the edge of the pre-hole. Wider plumes ( $\alpha_{large}$ ) lead to increased wetting compared with narrower plumes ( $\alpha_{small}$ ). [17]

The second process that leads to fuel films on the nozzle during fuel injection is caused by recirculation of the flow as it exits the orifice. During the injection process, a shear layer is formed between the ambient gases in the combustion chamber and the injected fuel. The shear layer is formed by a complex mixing process that is responsible for air-entrainment and mixing of the liquid and vapor phases of fuel with air. As part of the fluid mixing, vortices of fuel droplets and vapor are formed. The vortices re-entrain some of the fuel and air mixture back into the bulk flow, but some of the mixture escapes from the bulk flow. Fluid that escapes the vortices in the form of fuel droplets can be deposited on the injector tip due to the low-pressure zones formed near the nozzle exit. Droplets can deposit and stay on the injector tip due to the

Coandă effect, i.e. the tendency for fluid to stay attached to a convex surface due to low pressure. A schematic of this vortex-droplet wetting process is shown in Figure 4.3.

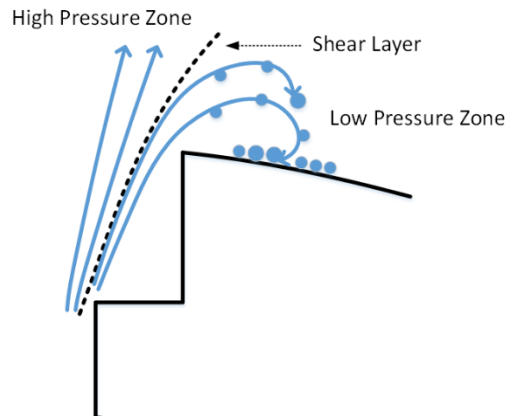


Figure 4.3: Schematic of the vortex-droplet tip-wetting process where droplets that escape from the shear layer of the fuel spray in the low-pressure zone near the nozzle exit can be deposited on the injector tip. [17]

Injector tip wetting also occurs at the end of the injection event. During needle closing, the fuel flow rate decreases, which leads to lower flow velocities and lower momentum flow. The low flow rate results in ‘fuel dribble’ i.e. ligaments and large droplets formed at the end of injection [29–31]. Previous work on diesel injectors has focused mostly on identifying the end-of-injection needle effects on bubble ingestion inside the nozzle and total mass ejected from fuel dribble. Eagle and Musculus [23] provide a comprehensive categorization of dribble events for diesel fuel and heavy duty fuel injectors. They identified three dribble behaviors that occurred during one engine cycle as well as proposed five potential physical processes that contributed to diesel fuel dribble. The effect of fuel dribble on tip wetting has been recorded and reported by Peterson et al. [22] for gasoline in GDI engines. Some large droplets and ligaments are likely to deposit onto the injector tip, because the liquid parcels do not have enough momentum to separate from the nozzle. A schematic of fuel-dribble tip wetting is shown in Figure 4.4. Very few studies to date have investigated connections between fuel dribble and injector tip wetting.

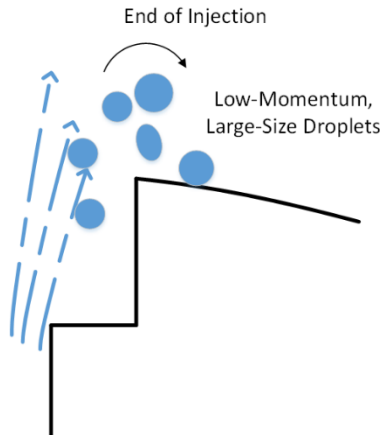


Figure 4.4: Schematic of the fuel-dribble tip-wetting process that occurs due to low-momentum, large-size droplets and ligaments depositing on the tip at the end of the fuel injection event. [17]

The last mechanism to affect tip wetting considered in this work is attributed to the liquid and gas mixture inside the nozzle or sac volume. During the expansion stroke of the engine cycle, the fuel mixture inside the sac volume is syphoned out of the injector. For diesel injectors, Eagle and Musculus [23] refer to this as late-cycle dribble, but made no connection to tip wetting. Tip wetting can occur during this process because the fuel mixture can condense onto the injector tip due to changing state conditions. The effects of this fuel-condensation tip wetting mechanism are also not well studied or understood.

The tip drying mechanisms are controlled by heat (or thermal) and mass transfer. Thermal evaporation of the liquid film on the injector tip is dependent upon several parameters including tip temperature, ambient pressure and temperature, total deposited fuel mass, and time. Fundamentally, the physics of liquid film thermal evaporation on an injector tip is analogous to sessile droplet evaporation on a hot plate. A droplet at steady-state conditions can go through two vaporization regimes: *single-phase evaporation* for tip temperatures below the liquid boiling point, and *boiling evaporation* for tip temperatures much higher than the boiling point. As described earlier, Stanglmaier et al. [26] studied the evaporation behavior for Howell EEE certification gasoline at different system pressures, and the results indicated that at engine-like conditions, vaporization of multi-component fuels was best represented as single-phase evaporation.

Tip drying also occurs due to mass convection. Piston motion induces charge motion that contributes to fuel film evaporation through mass convection, and importantly, the effects of airflow are only significant during single-phase evaporation[24]. As a consequence, tip drying is

attributed to single-phase evaporation and mass convection which are shown schematically in Figure 4.5. Both tip drying mechanisms are a function of the bulk fluid temperature,  $T_g$ , and local gas velocity,  $u_g$ , the fuel film or droplet temperature,  $T_L$  and the nozzle tip or wall temperature,  $T_w$ .

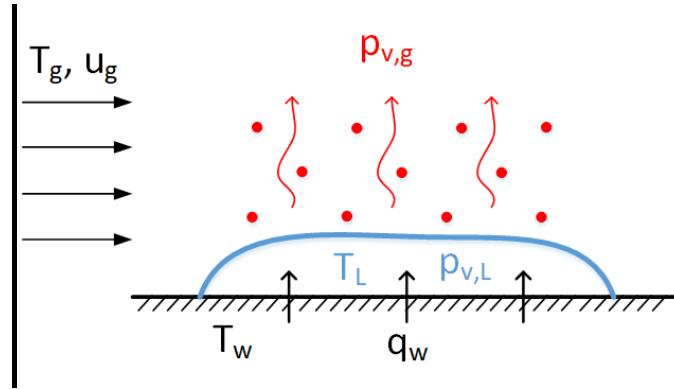


Figure 4.5: Schematic of the tip drying mechanisms based on single-phase evaporation which is a function of the liquid and gas phase fuel pressures ( $p_{v,L}$  and  $p_{v,g}$ , respectively) and the fluid, wall and film temperatures ( $T_g$ ,  $T_w$  and  $T_L$ , respectively) and forced convection which is a function of the local fluid velocity  $u_g$ . [17]

### 4.3 Experimental Methodology

#### 4.3.1 Engines Specifications

The experimental approach used a broad range of physical hardware and operating conditions to develop a strong statistical understanding of the effects on engine-out PN emissions. Three multi-cylinder, turbocharged engine architectures by different car manufacturers were used to consider the effects of combustion chamber and differences in side- and centrally- mounted fuel injection. The major attributes of the three engines used are summarized in Table 4.1. All engines were turbocharged, used direct injection, and had two exhaust valves and two intake valves. Additionally, the same reference grade gasoline (EPA Tier 3 Premium Certification Gasoline) was used for all experiments. Engine 1 and 2 had side-mounted injectors, while the injectors were centrally mounted in Engine 3.

Table 4.1: General features of the engines used in the study

Engine	1	2	3
Number of Cylinders	4	6	4
Injector Mounting Position	Side Mount	Side Mount	Central Mount

The engine parameters varied in the study were engine speed, engine load (characterized by brake mean effective pressure), start of fuel injection timing, fuel rail pressure and engine coolant temperature, which are summarized in Table 4.2. The fixed parameters for all experiments included air intake temperature (30 °C), spark timing (set based on maximum brake torque (MBT) timing, until the onset of knocking, where the spark is retarded to mitigate knock), intake and exhaust valves timing, air to fuel ratio ( $\lambda = 1$ ) and injection mode (single injection). The start of injection (SOI) timing is provided in crank angle degrees before top dead center (CAD bTDC) with reference to the power stroke; meaning that lower SOI values indicate late injection timing, while increased SOI values indicate early injection timing. Brake mean effective pressure (BMEP) of up to 8 bar was set by natural aspiration of intake air. At 10 bar BMEP or more, boosted intake air pressure was used. The required load was achieved by varying the injection duration for the single injection strategy at the given injection pressure.

Table 4.2: Category and range of engine operating parameters studied

<b>Parameter</b>	<b>Abbreviation</b>	<b>Unit</b>	<b>Range</b>
Engine Speed	N	RPM	1000, 2000, 3000
Start of Injection Timing	SOI	CAD bTDC	250, 260, 270, 280
Brake Mean Effective Pressure	BMEP	bar	2, 4, 6, 8, 10, 12, 14, 16, 18
Fuel Rail Pressure	$p_f$	bar	100, 200, 300
Coolant Temperature	$T_c$	°C	40, 65, 90

#### 4.3.2. Injector Specifications

A large number of injectors were tested in all three engine architectures. The internal geometry of the injectors was varied systematically. The three parameters considered were hole length, conicity, and pre-hole diameter. Table 4.3 provides a summary of the injectors used in the study including the engine each injector was tested in and the values of geometric parameters of each injector. Hole length was normalized to the largest hole length of the injectors. Similarly, the pre-hole diameter was normalized to the largest pre-hole diameter. The conicity of the injectors varied between converging and diverging. Comparisons made between injectors in the results section only exhibit one geometrical change that is listed in the table. For example, injectors E and F only differ by hole length whereas F and G may appear the same but have other geometrical differences not listed in the table such as spray targeting, number of holes, and tip design. Each injector is unique and data should not be compared across figures.

Fuel mass deposited on the injector tip was not measured directly, as there was no physical or optical access to the injector tip. The effects of coked or fouled injectors were also not considered. However, it is known that coked injectors amplify the deposition of fuel on the injector tip [4,18]. This is not considered a limitation as the study focuses on trends, and the test procedure (described below) ensured a consistent deposit layer for all engine experiments. Importantly, the SOI range for engine operating conditions were selected at conditions where PN emissions were associated with fuel injector tip wetting and where other sources of PN, like fuel spray impingement on the piston or chamber walls, were expected to be less important.

Table 4.3: Injector parameters used in the experimental study

<b>Injector</b>	<b>Engine</b>	<b>Normalized Hole Length</b>	<b>Conicity*</b>	<b>Normalized Pre-hole Diameter</b>
A	1	0.67	+	0.65
B	1	0.67	+	0.70
C	1	0.67	-	0.70
D	1	0.67	+	0.70
E	2	0.67	+	0.65
F	2	0.57	+	0.65
G	2	0.57	+	0.65
H	2	0.93	+	0.65
I	3	0.73	+	0.70
J	3	0.73	-	0.70
K	1	1.00	+	1.00
L	2	0.67	+	0.70

\*Positive signs indicate diverging and negative signs indicate converging.

Tip temperature was measured in Engine 3 by instrumenting one GDI injector (Injector J) with a K-type thermocouple. For consistency, the injector was installed in the same cylinder (cylinder 1, located farthest from the flywheel) for all Engine 3 experiments. The exact location of the temperature sensor is shown in Figure 4.6. The tip temperature sensor was placed 0.4 mm below the tip surface and 1.13 mm away from the external sidewall of the injector tip.

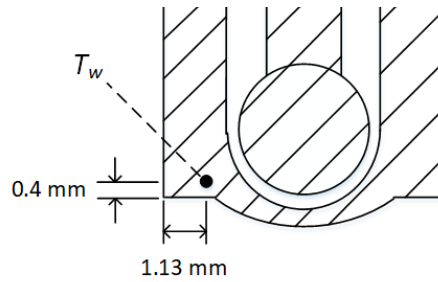


Figure 4.6: Location of the tip temperature sensor in the instrumented GDI injector tip (Injector J in Table 4.3) [17]

#### 4.3.3. Particulate Emissions

A sample of engine exhaust (post-turbocharger) was directed into a laser scattering condensation particle counting system (Horiba MEXA-2100SPCS) to measure engine-out PN using a 1 Hz data acquisition rate. The measured PN is reported as number of particles per cubic centimeter ( $\#/cm^3$ ) and each reported PN measurement represents a 30-second time average. The exhaust sample fluid was diluted with air for all engine experiments using a dilution ratio of 1500 for Engine 1 and 3 and a dilution ratio of 7500 for Engine 2. The temperature of the exhaust at the sampling location was dependent on the operating point for each engine. The diluted sample had a temperature of 190 °C for all engine experiments.

#### 4.3.4 Test Procedure

A 20-hour test procedure was established for all engines, and the procedure timeline is shown in Figure 4.7. The general procedure included three phases: the engine warmup phase, the injector coking phase (to simulate injector aging), and the SOI-BMEP testing phase. Before the start of the testing procedure, a set of clean multi-hole GDI injectors were installed in the engine at room temperature. The engine was then fired and allowed to thermally equilibrate for 10-12 minutes at an engine load of 4 bar and 1000 RPM. After the engine warmup phase, (when the engine-out coolant temperature was stabilized at 90 °C), the engine was set at the coking operating point of 10 bar load, 2000 RPM, and 200 bar injection pressure. The engine operated at this point steadily for 16 hours. The injector tip formed a stabilized carbon deposit layer during the steady state operation. The SOI-BMEP testing was started after the end of the coking procedure. For each SOI-BMEP operating point, the engine was allowed to thermally equilibrate for 1-2 minutes before PN measurements were made. As listed in Table 2, the SOI-BMEP tests were performed at different engine speeds, coolant temperatures and injection pressures. The complete test procedure was repeated for each new or clean set of injectors. The injectors were

cleaned using an ultrasonic bath. Consequently, the PN values reported in this study reflect values for coked injectors with stabilized deposit layers on the fuel injectors.

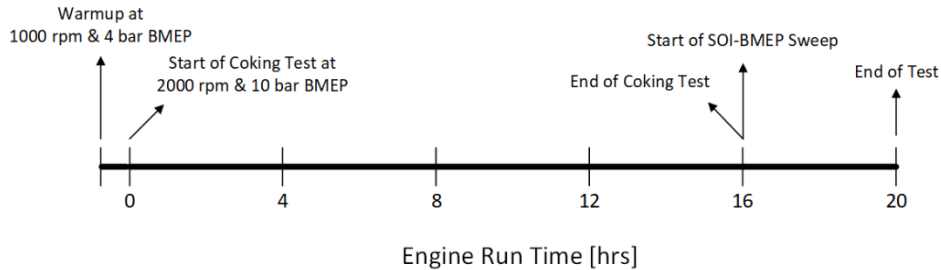


Figure 4.7: Timeline of engine test procedure

#### 4.3.5 Repeatability and Uncertainty Analysis

To ensure the consistency and integrity of the experimental setup and measurement systems, repeatability and uncertainty analysis was conducted. The complete test procedure was repeated three times for coolant temperature of 90 °C, injection pressure of 200 bar, BMEP of 10 bar and 2000 RPM. Sample results of the repeatability tests are shown in Figure 4.8 for Engine 3 and Injector J. Figure 4.8a shows the measured PN as a function of engine-out coolant temperature for the three warmup trials starting at time equal to 0 hrs (clean injector tip). Good repeatability is observed, both for the peak PN values, the transient behavior and the steady-state behavior when the engine-out coolant temperature exceeded 70 °C. The PN measurements in the last 60 seconds of the engine warmup phase was repeatable within 20%, based on one standard deviation for each PN measurement. Figure 4.8b shows the measured PN for the three trials of the coking phase. The tests were also repeatable within 20%, where the uncertainty was calculated using measurements taken during the 16-hour test procedure. Measurements taken for other experimental conditions often has lower standard deviations and lower uncertainties. However, a conservative uncertainty of 20% was applied to all PN measurements performed in this study. The error bars in all fi of PN data represent this  $\pm 20\%$  uncertainty. The repeatability of the fuel injector tip temperature measurement was also investigated and was found to be repeatable within 5%, calculated using one standard deviation. This uncertainty was extended to all tip temperature measurements for all other conditions tested in Engine 3.



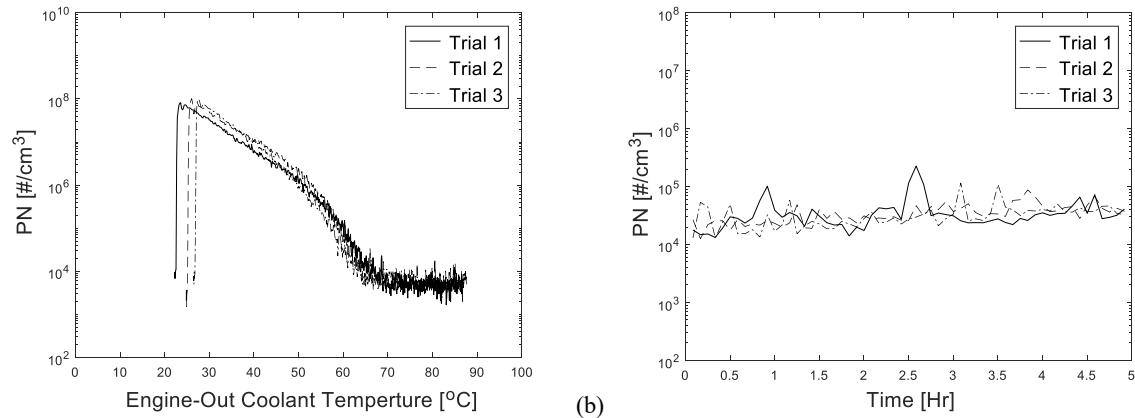


Figure 4.8: Repeatability of PN measurement for (a) the warmup procedure, and (b) the first five hours of the coking procedure, performed using Engine 3 and Injector J for coolant temperature of 90  $^{\circ}\text{C}$ , injection pressure of 200 bar, BMEP of 10 bar and engine speed of 2000 RPM.

## 4.4 Results

### 4.4.1. Effects of Engine Operating Conditions

#### 4.4.1.1. Engine Load

In this study, it was important to isolate (as much as possible) injector tip wetting as the dominant PN formation mechanism. Typical results for PN from the SOI-BMEP tests are provided in the form of a heat map in Figure 4.9. The figure shows two distinct regions of high (dark red) and low (light yellow) PN emissions, separated by SOI timing of approximately 290-300 CAD bTDC. In the SOI region between 300 and 320 CAD bTDC, injection was early in the engine cycle producing high PN emissions. Advanced injection timing leads to higher amounts of fuel impingement on the piston crown. Lower PN emissions (by 1 to 3 orders of magnitude) are observed in the SOI region of 250 to 290 CAD bTDC. These later fuel injection conditions have been identified as conditions where tip wetting is the dominant PN formation mechanism. The effects of SOI timing on the different fuel wetting mechanisms have been confirmed using in-situ high speed imaging and the images are reported in Fatouraie et al. [32]. All engine architectures and operating conditions yielded similar trends, although the borderline between high and low PN emissions would sometimes vary slightly (e.g., SOI = 300-310 or 310-320 CAD bTDC). Based on these results, the focus of this study was on SOI timing between 250 to 280 CAD bTDC, where tip-wetting is expected to be the dominant source of PN emissions.

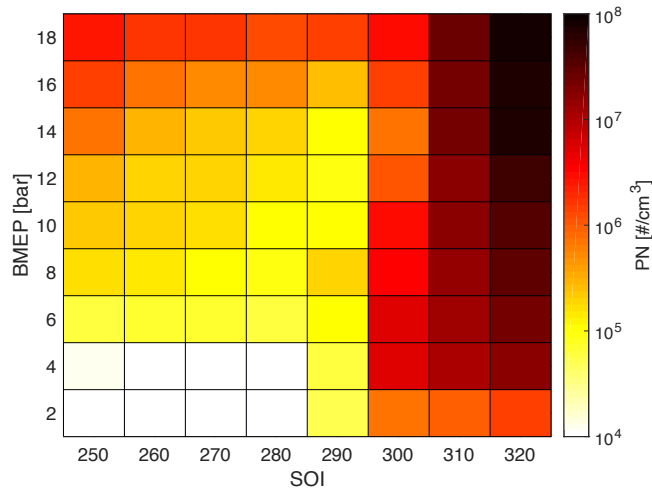


Figure 4.9: Typical particulate number (PN) results as a function of load (BMEP) and start of injection (SOI [CAD bTDC]) for Engine 1 (see Table 1) injector B, engine speed of 2000 RPM, fuel rail pressure of 200 bar and coolant temperature of 90 °C

Figure 4.10 presents the results for PN as a function of BMEP and SOI for Engine 2 for three engine speeds and fixed fuel rail pressure and coolant temperature. The PN emissions show higher sensitivity to load at lower engine speed for all SOIs with higher PN at higher loads. At the highest engine speed studied, 3000 RPM, the PN emissions became almost insensitive to load, and systematically higher PN emissions were observed at 3000 RPM for all SOIs compared with the lower engine speeds. At the lower engine speeds, the PN emissions decreased as injection timing was advanced from 250 to 280 CAD bTDC for all loads.

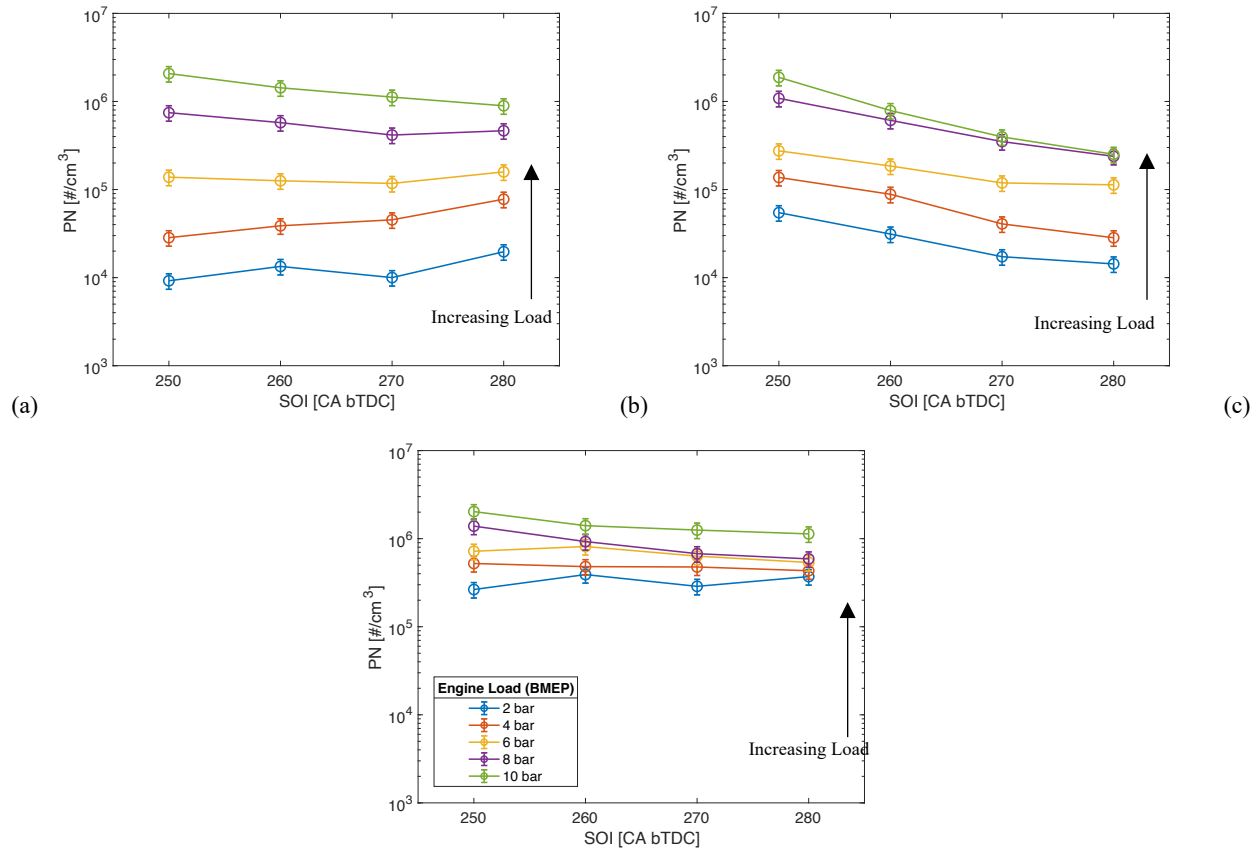


Figure 4.10: PN measurements for injector L and engine 2 as a function of load and injection timing for  $T_c = 90^\circ\text{C}$ ,  $p_f = 200\text{ bar}$  and engine speeds of (a) 1000 RPM (b) 2000 RPM and (c) 3000 RPM for Engine 2. The error bars represent 20% error from the mean.

Figure 4.11 presents the results for the fuel injector tip temperature and PN emissions as a function of BMEP for Engine 3 and Injector J for three engine speeds and fixed SOI, injection pressure and coolant temperature. The injector tip temperature increased with increasing load for all engine speeds except the highest load conditions at 2000 RPM (BMEP > 8 bar). The injector tip temperature did not increase after 10 bar BMEP due to the knock controller, which retarded the spark timing causing the combustion phasing to change. For 1000 and 3000 RPM, the PN emissions also generally increased with increasing engine load. However, for 2000 RPM, PN emissions decreased slightly from 2 bar to 8 bar BMEP, i.e., the load conditions where combustion phasing was retarded.

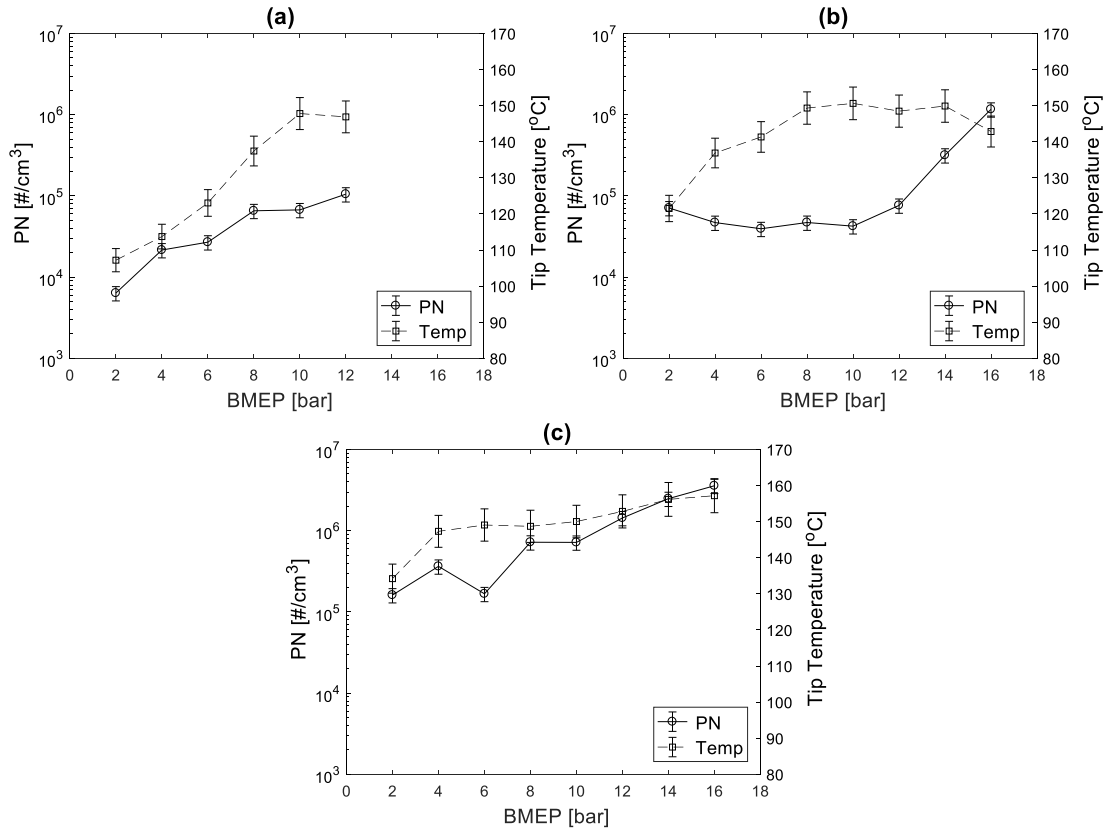


Figure 4.11: Tip temperature and PN emissions as a function of engine load for Engine 3 and Injector J for (a) 1000 RPM, (b) 2000 RPM and (c) 3000 RPM, and a coolant temperature of 90°C,  $p_f = 200$  bar, and SOI = 290 CAD bTDC.

#### 4.4.1.2. Fuel Rail Pressure

Figure 4.12 shows the effects of injection pressure on PN for fixed coolant temperature of 90 °C, fixed SOI of 260 CAD bTDC and three engine speeds. The results show that higher injection pressure consistently yields lower PN at all engine loads. The benefits for reducing PN with higher injection pressure are less for the increase from 200 bar to 300 bar compared with the increase from 100 bar to 200 bar. The results show increasing fuel rail pressure decreases particulate emissions which is consistent with previous studies. For example, Eitel et al. [33] performed engine experiments with gasoline injectors and measured particle concentration for different injection pressures. Their results showed increasing injection pressure reduced overall particle concentration, which they attributed to better mixture preparation and fewer flames on the injector tip.

For lower coolant temperature, the effects for fuel injection pressure were similar to the results presented in Figure 4.12. Increasing injection pressure lowered PN at all engine speeds.

An example for one The results for the effects of injection pressure and engine load on PN for lower coolant temperature are provided in the Appendix.

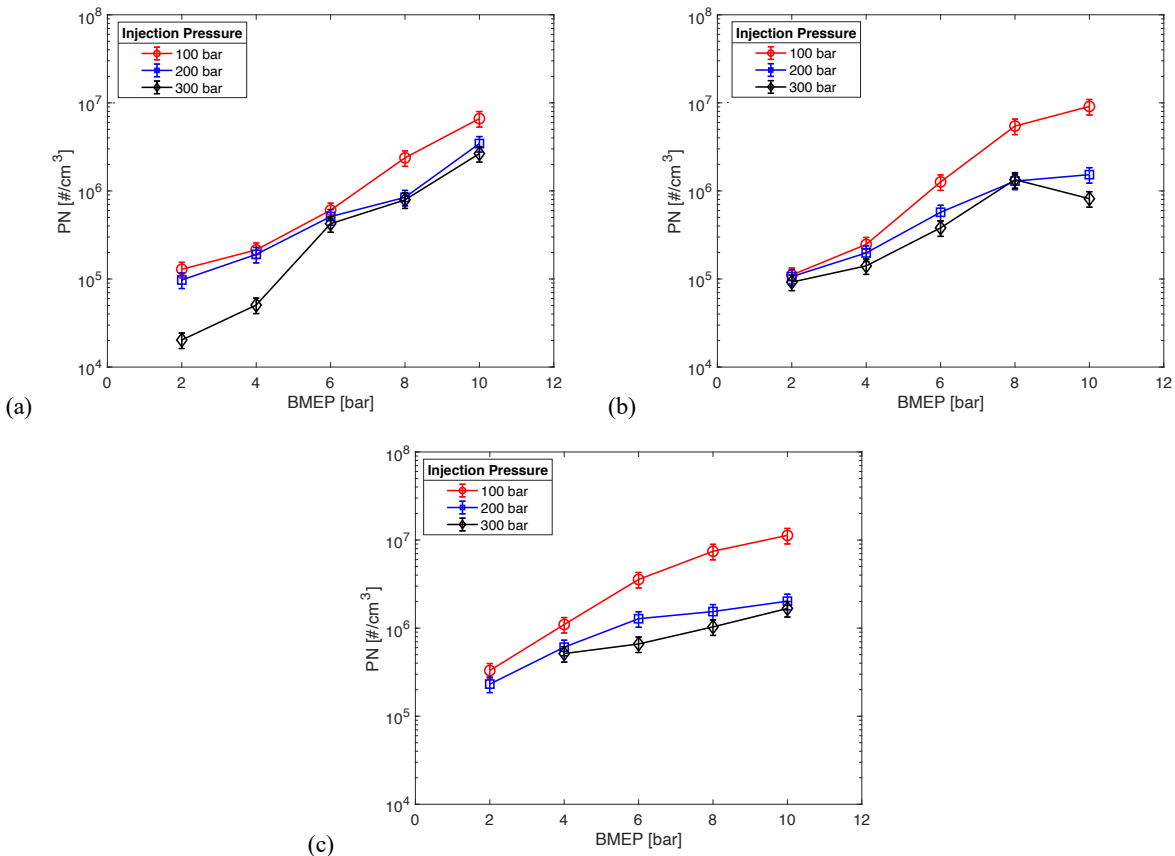


Figure 4.12: Injection pressure effects on PN for Injector L, Engine 2, coolant temperature of  $90^\circ\text{C}$ , and engine speed of (a) 1000 RPM (b) 2000 RPM and (c) 3000 RPM. PN results are for a fixed SOI in the tip wetting dominant regime of 260 CAD bTDC

#### 4.4.1.3. Engine Speed and SOI Timing

To compare the effects of engine speed, the SOI timing was converted to absolute time [ms]. Figure 4.13 shows the results for PN for fixed injection pressure of 200 bar, and coolant temperature of  $90^\circ\text{C}$  for Injector L and Injector D at 10 bar BMEP, both tested in Engine 1. The time scale represents the time available for tip drying, i.e., the time from the end of injection ( $t = 0$ ) to time of spark. The results in Figure 4.13a show an increase in PN as engine speed increased for fixed load conditions. The results may appear counter-intuitive since turbulence increases with higher engine speeds improving mixing and promoting a homogenous mixture, which would reduce PN emissions. However, in the tip wetting dominant region, higher engine speeds provide less time for tip drying, subsequently resulting in higher PN emissions. Similar trends for the effects of engine speed were observed for the other injectors and engines tested.

Figure 4.13 also shows that PN increased with later SOI timing. Earlier injection timings translate to longer time scales and later injection timings translate to shorter time scales for drying at a fixed injection duration and spark timing. Injecting later in the intake stroke reduces the total time for tip drying, resulting in increased PN emissions. Similar trends for the effects of SOI were observed for most of the 1000 RPM and 2000 RPM cases for different load conditions. However, for engine speeds of 3000 RPM, for some load conditions, the effects of SOI were less consistent than the data shown in Figure 4.13a (see Figure 4.13b and the Appendix for detailed results). The change in PN behavior at the highest engine speed indicates other PN formation mechanisms (in addition to tip wetting and drying) could be playing a role, such as under-mixing or other wetting mechanisms.

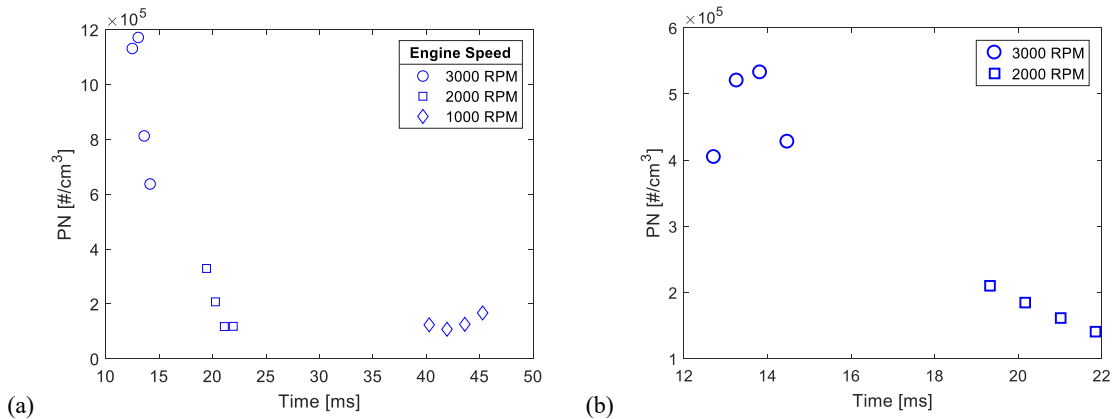


Figure 4.13: Effect of engine speed and SOI timing on PN emission for Engine 1 for fixed  $T_c = 90 \text{ }^\circ\text{C}$  and  $p_r = 200 \text{ bar}$  and (a) Injector L and (b) Injector D at BMEP = 10 bar tested. Time is the absolute time from the end of injection to the time of spark. So, for fixed injection duration and spark timing, shorter times correspond to later SOI and longer times correspond to earlier SOI

The results for the fuel injector tip temperature in Figure 4.14 provide additional insight into the trends for PN as a function of engine speed. The figure shows PN and tip temperature as a function of engine speed for Engine 3 and Injector J at a fixed SOI timing, injection pressure and coolant temperature for two different loads. In general, tip temperature was observed to increase with engine speed. Increased injector tip temperature would seem to cause better tip drying for decreased PN emissions. However, the reduced time available for evaporation by increasing the engine speed outweighs the increase in fuel injector tip temperature, leading to overall increase in PN. Tip drying is more sensitive to time scales and tip temperature.

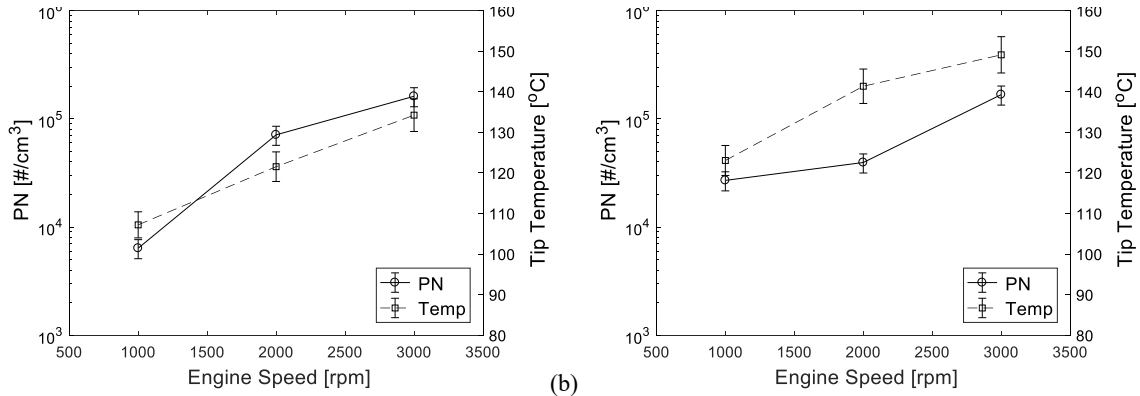


Figure 4.14: Tip temperature and PN emissions as a function of engine speed for Engine 3 and Injector J at and  $T_c = 90^\circ\text{C}$ ,  $p_r = 200\text{ bar}$ , and  $\text{SOI} = 290\text{ CAD bTDC}$  for (a)  $\text{BMEP} = 2\text{ bar}$  and (b)  $\text{BMEP} = 6\text{ bar}$

#### 4.4.1.4. Coolant Temperature

Figure 4.15 shows the effects of coolant temperature on PN for a fixed engine speed of 2000 RPM, fixed SOI of 260 CAD bTDC and two injection pressures of 100 bar and 300 bar for Engine 2 and Injector L. Higher coolant temperatures systematically lowered PN emissions. This trend was observed for all engine speeds, injection pressures, and SOI timings. Coolant temperature influences the engine head temperature, subsequently influencing the injector body and tip temperatures. Higher tip temperatures are expected to increase the evaporation rate of the liquid film on the injector tip, reducing tip wetting PN. Additionally, low coolant temperatures decrease fuel-air mixture evaporation in the cylinder increasing PN contribution due to lower homogeneity. Figure 4.16 shows PN emissions and tip temperature as a function of engine-out coolant temperature for Engine 3 and Injector J for SOI of 290 CAD bTDC, engine speed of 1000 RPM, BMEP of 4 bar, and injection pressure of 200 bar. As expected, increasing coolant temperature increased tip temperature and consequently reduced PN emissions.

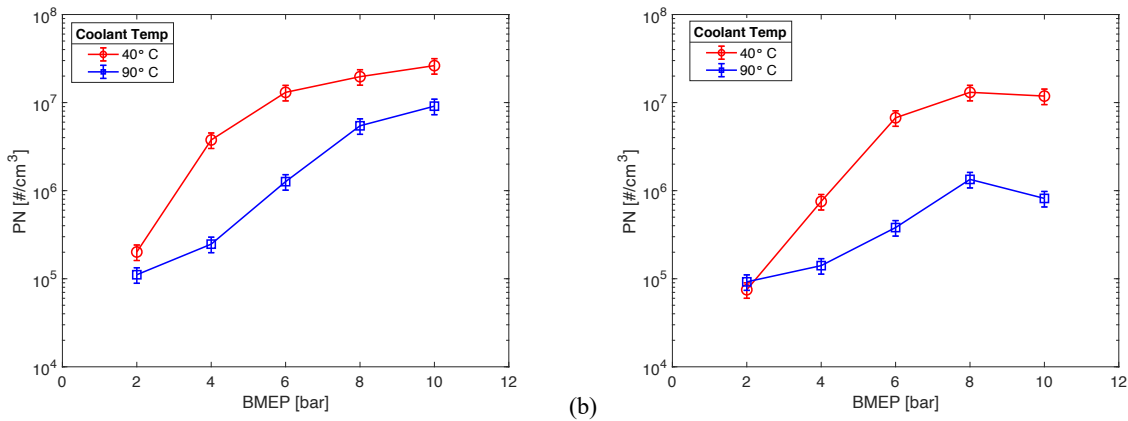


Figure 4.15: Coolant temperature effects on PN for Engine 2 and Injector L for an engine speed of 2000 RPM,  $\text{SOI} = 260\text{ CAD bTDC}$ , and (a)  $p_r = 100\text{ bar}$  and (b)  $p_r = 300\text{ bar}$

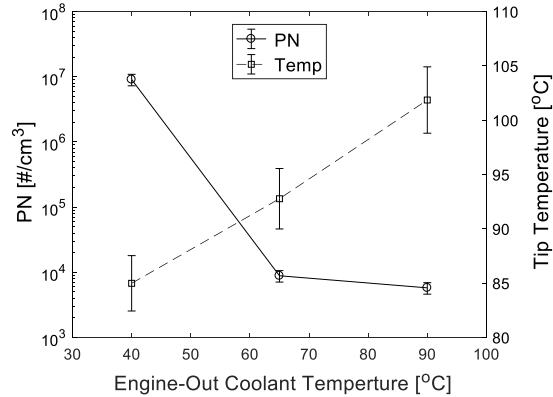


Figure 4.16: Tip temperature and PN emissions as a function of engine-out coolant temperature for Engine 3 and Injector J for 1000 RPM, BMEP = 4 bar,  $p_f = 200$  bar, and SOI = 290 CAD bTDC

#### 4.4.2. Effects of Injector Geometry

Throughout this section, the effects of fuel injector internal geometry on tip wetting PN are presented for fixed engine speed of 2000 RPM,  $T_c = 90$  °C,  $p_f = 200$  bar, and SOI = 260 CAD bTDC. Similar trends were observed as a function of fuel injector geometry for the other operating conditions. A summary of the injector geometry variations is presented in Table 4.3. Comparisons made between injectors only exhibit one geometrical change that is listed in the table. For example, in Figure 4.17 the only difference between injector E and F is hole length whereas injectors F and G may appear the same but have other differences not listed. Therefore, data should not be compared across figures.

##### 4.4.2.1. Hole Length

Figure 4.17 shows the results for PN of two different sets of injectors (E, F, G and H in Table 4.3) with varying hole lengths tested in the same engine architecture (Engine 2). The results as a function of normalized hole length show PN increases for longer hole lengths at almost all engine loads. While the effects are small at some conditions (within the uncertainty limits of the data), the log scale used in the figure, also makes the effects appear smaller when there are clear differences in the data. The trends are generally the same for other SOI timings and engine speeds.



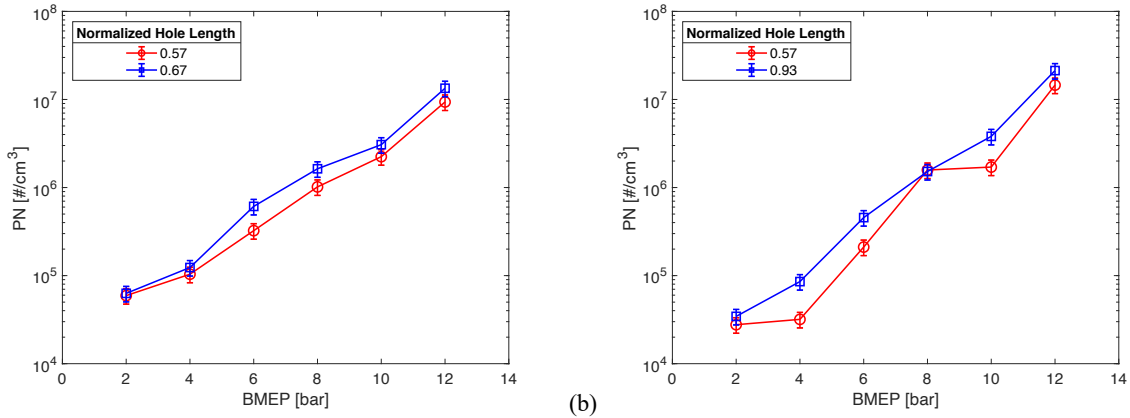


Figure 4.17: Effects of hole length on PN at 2000 RPM, 200 bar injection pressure, SOI timing of 260 CAD bTDC for the same engine architecture. (a) Effects are shown for injectors E (blue squares) and F (red circles) with varying hole length (b) Effects are shown for injectors G (red circles) and H (blue squares) with varying hole length

#### 4.4.2.2. Hole Conicity

Figure 4.18 compares the effects of orifice conicity on PN emissions as a function of load using the diverging and converging nozzles in two different engine architectures (Engines 1 and 3). In the figure, diverging nozzle data are represented by a positive sign and converging nozzle data are represented by a negative sign. The PN emissions were higher for the converging nozzle for most of the engine loads tested for both side and centrally mounted injector architectures. Converging nozzles may lead to faster penetration, potentially leading to higher fuel impingement on the piston and combustion chamber walls; whereas a diverging nozzle may result in a wider spray plume that could enhance mixing and decrease fuel impingement. Given the conditions of the experiments were selected to emphasize tip wetting mechanisms, and not fuel impingement, enhanced mixing seems a more likely explanation for the observed trends.

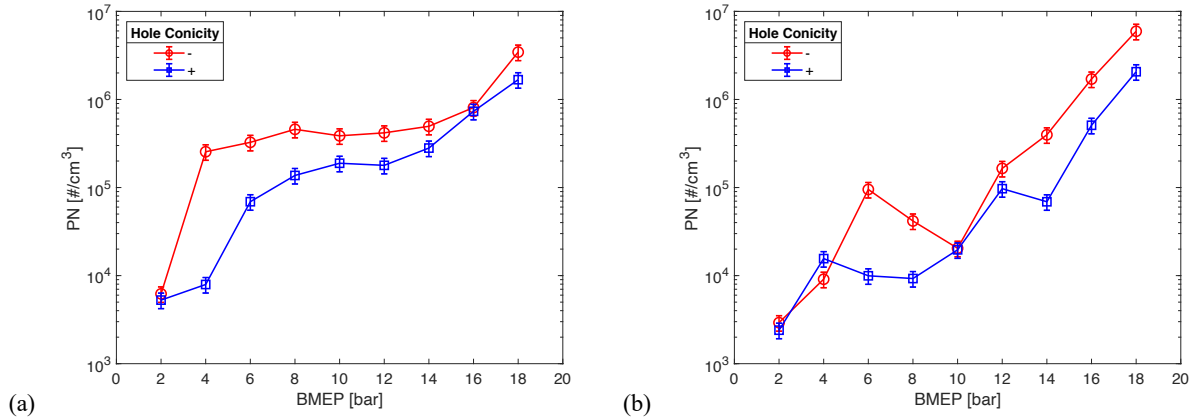


Figure 4.18: Effects of hole conicity on PN at 2000 RPM, 200 bar injection pressure, SOI timing of 260 CAD bTDC for two engine architectures. (a) Effects are shown for injectors B (blue squares) and C (red circles) with varying hole conicity in Engine 1. (b) Effects are shown for injectors I (blue squares) and J (red circles) with varying hole conicity in Engine 3. The negative sign indicates converging nozzle data and the positive sign indicates diverging nozzle data.

#### 4.4.2.3. Pre-hole Diameter

The effects of pre-hole diameter were considered for a single engine architecture, Engine 1, and the results are presented in Figure 4.19 as a function of engine load. The larger pre-hole diameter yielded higher PN emissions for low to mid loads (2 to 8 bar BMEP). However, at high loads the trend inverted and the larger pre-hole diameter yielded lower PN emissions. The effects of nozzle pre-hole diameter on PN emissions have been investigated previously in GDI engines with contradictory observations. Dagef rde et al. [19] found that coked injectors with larger pre-holes resulted in higher engine-out PN levels. The researchers attributed the increase in PN directly to the increase in injector pre-hole diameter which was also verified by long distance microscopy images in a spray chamber. They hypothesized that larger pre-hole diameters would increase the transverse flow at the outlet of the injector hole thereby increasing the injector tip wetting. Leick et al. [21] found no discernable difference in the film area and height between larger and smaller pre-hole diameter injectors using laser-induced fluorescence (LIF). However, when tested in an engine, higher PN emissions were observed for larger pre-holes at all engine loads, although the researchers attributed the increase in PN to flash boiling rather than the increase in injector pre-hole diameter. Lastly, Gawlica et al. [14] stated in their modeling study that tip wetting is more likely at lower loads and late SOI which agrees with the data presented here. The results of the current work and these other studies indicate there is an optimal pre-hole diameter for different load/operating conditions.

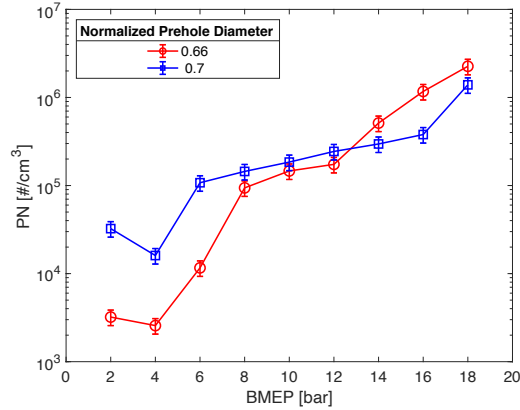


Figure 4.19: Effects of pre-hole bore diameter size on PN at 2000 RPM, 200 bar injection pressure, SOI timing of 260 CAD bTDC for Engine 1 using injectors A (red circles) and D (blue squares)

#### 4.5 Discussion - Correlation of PN with Tip Wetting and Tip Drying Mechanisms

A summary of the trends observed for the PN emissions is presented in Table 4 in terms of the effects of the different operating conditions and fuel injector tip characteristics on the engine-out PN emissions. The trends are further discussed here in terms of the effects of the parameters in Table 4 on the conceptual understanding of the different tip-wetting and tip-drying mechanisms described previously.

Table 4.4. Summary of the effects of the different operating conditions and fuel injector tip characteristics on engine-out PN emissions

Parameter	Increasing engine operating parameters					Increasing fuel injector tip geometry		
	N	SOI*	p <sub>f</sub>	T <sub>c</sub>	BMEP	L	Diverging* *	d
PN	↑↑	↓	↓	↓↓	↑↑	↑	↓↓	↑↓
Wide plume wetting			↓	↑↑	↑	↓	↑	↑
Vortex droplet wetting			↓	↑	↑	↑		↑
Fuel dribble wetting	↓		↓	↓		↑	↑	
Fuel condensation wetting	↑	↑		↓	↑			
Tip drying (single-phase evaporation)	↓↓	↑		↑↑	↓			

SOI\*= more advanced or earlier start of injection timing

L = hole length, d = pre-hole diameter, Diverging\*\* = when a diverging nozzle

↑↑&↓↓ = order of magnitude effects, ↑&↓ = smaller scale effects, blank space = no effect

The parameters that had the most significant effects on PN were engine speed, engine load, coolant temperature, and hole conicity. Injection timing, fuel rail pressure, hole conicity, hole length and pre-hole diameter also impacted the PN emissions, but to a lesser degree. Each of these parameters is expected to have direct correlation with at least one of the tip-wetting and tip-drying mechanisms presented earlier. Although the effects of injector hole length were smaller on PN, there was a fairly consistent trend where slightly higher PN emissions were produced with longer hole lengths. Two major effects occur with longer hole lengths. First, a longer hole length would produce a narrower spray. The narrower spray is less likely to cause fuel deposition via the *wide plume wetting* mechanism. Second, a narrow spray is likely to form larger droplets because of reduced levels of air entrainment. The larger droplets could result in higher tip wetting via the *vortex droplet wetting* and *fuel dribble wetting* mechanisms. Studies performed by Moon et al. [34] and Tu et al. [35] demonstrated that increasing the L/D ratio in a GDI injector from 2.5 to 8.3, by increasing the hole length, would increase the Sauter mean diameter (SMD) by a factor of two. This trend in larger droplets caused by longer hole lengths supports the conclusion that longer hole lengths would increase *vortex droplet wetting*, and *fuel dribble wetting*.

Figure 4.19 shows the more complex response of the PN emission to pre-hole size, where lower PN was observed for low to mid loads, while at high loads the smaller pre-hole produced higher PN. Larger pre-hole diameters are expected to increase the lateral flow at the outlet of the orifice, thereby increasing the tip wetting via the *wide plume wetting* mechanism. The results partly agree with this analysis, indicating other mechanisms are contributing to PN emissions at higher loads. The results are also partly in agreement with the literature described previously [14,19,21]. In the other studies, the size difference between the main- and pre-holes was much greater than for the injector variants used in this study. This would indicate there is an optimal difference in diameters that can result in lower tip wetting PN.

The results in Figure 4.18 show converging nozzles produced higher PN emissions. However, a diverging nozzle would be expected to produce more tip wetting via *wide plume wetting* and *fuel dribble wetting* mechanisms. Specifically, a diverging nozzle will generate higher dispersion angles at the exit of the hole and into the pre-hole thus increasing tip wetting via the *wide plume wetting mechanism*. Additionally, a diverging nozzle has lower energy due to flow deceleration. The *fuel dribble mechanism* would therefore increase due to lower momentum

from the decelerated flow; thereby increasing tip wetting. The results of the current work were opposite to the trends expected, indicating other tip wetting factors may be present. Bergstrand [36] conducted engine experiments using diesel injectors with five different orifice shapes including converging and diverging nozzles. The study also found diverging nozzles resulted in lower soot emissions attributed to enhanced mixing processes but did not propose tip wetting mechanism as the cause of the effects. There are almost no studies that discuss the effects of nozzle geometry of GDI injectors on emissions.

Increasing engine load showed an increase in PN emissions as seen in Figure 4.10. Increasing load is achieved by increasing injection duration which increases *wide plume wetting* and *vortex droplet wetting* due to longer exposure time. The other two wetting mechanism, *fuel dribble wetting* and *fuel condensation wetting* are not expected to be a function of engine load. Injection duration is also affected by fuel rail pressure. Decreasing fuel rail pressure increased PN emissions as shown in Figure 4.12. Similar to engine load, decreasing fuel rail pressure would increase the required injection duration for a fixed load condition resulting in more tip wetting via both the *wide plume wetting* and the *vortex droplet wetting* mechanisms. Interestingly, fuel rail pressure also has implications on droplet size. Increasing fuel rail pressure would decrease the droplet size via enhanced atomization and better mixing [33]. The smaller droplets would decrease the contribution of wetting caused by the *vortex droplet wetting* mechanism and *fuel dribble wetting* mechanism. Both smaller droplets and decreased injection duration caused by increased injection pressure result in less tip wetting via *wide plume wetting*, *vortex droplet wetting*, and *fuel dribble wetting*.

The effects of engine speed and coolant temperature on the tip wetting and drying mechanisms can be better understood by examining the trends in fuel injector tip temperature presented in figures 14 and 16. The liquid fuel vapor pressure is a property of the liquid and depends only on liquid temperature. The liquid film deposited on the injector tip has a thickness on the micrometer scale [21,25], and any fuel on the tip therefore reaches the tip temperature instantly. This suggests the liquid vapor pressure is a strong function of the tip temperature, and the most critical factors affecting the tip drying process are the tip temperature and the residence time of the liquid fuel film on the tip, which are affected by the different engine operating conditions. Note that tip temperatures might affect the droplet size, flash boiling, and spray-wall interactions thereby affecting tip wetting.

In GDI engines, tip temperature is most likely influenced by three main factors: (1) peak in-cylinder gas temperature (which is a function of load/injected fuel mass, engine speed, and combustion phasing), (2) injector location (side mounted versus central mounted) and (3) engine coolant temperature. An increase in injected fuel mass leads to an increase in combustion peak temperatures, and eventually raises the tip temperature as seen in Figure 4.11. The increase in injected fuel mass also is expected to increase the initial film mass on the tip after injection. Hence, there is a trade-off at higher loads, where increased fuel mass increases fuel tip wetting while simultaneously increasing injector tip temperature which increases tip drying. Thus, increasing tip temperature does not lead consistently to lower PN, whereas increasing coolant temperature does.

The time for evaporation is restricted by a short operational window from end of fuel injection to spark. Hence, the time scale plays a significant role in the evaporation process. For a fixed engine load and injection pressure, evaporation time is mostly influenced by changes in engine speed as well as SOI timing. It is known that turbulence tends to increase with higher engine speeds thus increasing fuel/air mixing providing a homogenous mixture for higher gas and tip temperatures. However, in the tip wetting dominant region higher engine speeds lead to less time for tip drying which subsequently lead to fuel film mass remaining at the time of spark. This effect can be observed in Figure 4.14, which shows the measured tip temperature as a function of engine speed for two different loads. Figure 4.14 shows at 2 bar BMEP, tip temperature increased from 110 °C at 1000 RPM to 135 °C at 3000 RPM. At 6 bar BMEP, the tip temperature increased from 125 °C at 1000 RPM to 150 °C at 3000 RPM. Nonetheless, this increase in tip temperature had negligible effect on PN emissions due to the reduced timescale with engine speed.

Similarly, injecting late in the intake stroke reduces the time for tip drying, resulting in increased film mass on the tip. Additionally, increasing dry time substantially does not reach zero PN emissions. For example, in Figure 4.13a the PN levels reaches an asymptotical limit beyond 22 ms. This suggests that either evaporation remains constant or the fuel has fully evaporated. The constant PN level also suggests that other mechanisms may contribute to the emissions, such as fuel condensation wetting, under-mixing in the gas phase, or engine oil particulates.

## 4.6 Conclusions

The reported particulate number levels for vehicles equipped with gasoline direct-injection engines in many studies between 2009 and 2017 were within  $6 \times 10^{11}$  and  $2 \times 10^{13}$  particles/km. Current particulate number standards in Europe limits the PN to  $6 \times 10^{11}$  particles/km, and the same limit must be met by 2020 in China. Identifying and mitigating the sources of PN emissions for gasoline direct-injection engines is therefore critical to meet the challenging future emissions targets. Among the different sources, injector tip wetting has been identified as a significant source of particulate number emissions in regions where tip wetting is the dominant PN formation mechanism. Thus, eliminating tip wetting as a source of particulates would contribute significantly to meeting future limits.

In the present work the physical mechanisms that are suspected to control tip wetting and tip drying are studied. The tip wetting mechanisms include wide plume wetting, vortex droplet wetting due to recirculation/air entrainment, fuel dribble wetting, and fuel condensation wetting. In the wide plume wetting mechanism, the liquid fuel physically hits the corner edge of the hole outlet and due to surface roughness, wide plume and adhesive forces the liquid forms a film around the outlet. The vortex droplet wetting mechanism occurs when droplets break off from the spray and splash onto the tip, which has been seen more dominantly during the end of injection, which is referred to as fuel dribble wetting. The thermal tip drying mechanism considered in this work is single-phase evaporation.

The tip wetting mechanisms are a function of both engine operating conditions and injector design parameters, which include injection pressure, chamber temperature and pressure (i.e. flash boiling), engine load, injector hole length, hole angle and pre-hole size. The correlation of decreasing PN with increasing fuel injection pressure was due to lower injector tip wetting. This was suspected to be caused by the wide plume wetting, vortex droplet wetting and fuel dribble wetting mechanisms. Increasing engine load by increasing the injection duration was found to increase tip wetting PN. The tip wetting mechanisms suspected to be responsible for this trend were wide plume wetting and vortex droplet wetting mechanisms. Changes in internal geometry revealed that increasing hole length resulted in a net increase in tip wetting PN. The mechanisms attributed for this were increasing vortex droplet wetting and fuel dribble wetting mechanisms. Divergent nozzle resulted in lower PN, however a divergent nozzle was suspected to increase tip wetting via wide plume and fuel dribble mechanisms. Similarly, increasing pre-

hole size resulted in an inconclusive PN trend but was believed to increased wide plume wetting and vortex droplet wetting.

The effects of operating conditions on the tip drying mechanism were also investigated. It was found that the time scale (affected by engine speed and start of injection timing) and injector tip temperature are the most important parameters affecting tip drying. More than an order of magnitude change in PN emissions was observed by changing the drying timescale. Furthermore, injector tip temperature was found to correlate with PN emissions for the case where the coolant temperature was changed. Increasing the coolant temperature increased the injector tip temperature, resulting in increased tip drying rate.

#### 4.7 Acknowledgements

We thank BOSCH Group for providing financial and technical resources for this work.

#### References

1. Commission Regulation (EU) 2017/1151 of 1 June 2017 supplementing Regulation (EC) No 715/2007 of the European Parliament and of the Council on type-approval of motor vehicles with respect to emissions from light passenger and commercial vehicles (Euro 5 a, *Off. J. Eur. Union* (692):1–643, 2017.
2. He, H. and Yang, L., “China’s Stage 6 Emission Standard for New Light-Duty Vehicles,” *Int. Counc. Clean Transp.* (March):13, 2017.
3. CARB, “Final Regulation Order, LEV III Amendments,” *Calif. Code Regul. Title 13, Sect. 1900, 1956.8, 1960.1, 1961, 1961.2, 1961.3, 1962.1, 1962.2, 1976, As Amend.* December 6, 2012.
4. Boger, T. and Cutler, W., “Reducing Particulate Emissions in Gasoline Engines,” SAE International, Warrendale, ISBN 9780768094176, 2018, doi:10.4271/0768094186.
5. Braisher, M., Stone, R., and Price, P., “Particle number emissions from a range of European vehicles,” *SAE Tech. Pap.* (Ci), 2010, doi:10.4271/2010-01-0786.
6. Steimle, F., Kulzer, A., Richter, H., Schwarzenthal, D., and Romberg, C., “Systematic analysis and particle emission reduction of homogeneous direct injection SI engines,” *SAE Tech. Pap.* 2, 2013, doi:10.4271/2013-01-0248.
7. Adamczyk, A.A., Kaiser, E.W., Cavolowsky, J.A., and Lavoie, G.A., “An Experimental



- Study of Hydrocarbon Emissions from Closed Vessel Explosions,” *18th Int. Symp. Combust. Combust. Inst.*, 1981.
8. Stevens, E. and Steeper, R., “Piston Wetting in an Optical DISI Engine : Fuel Films , Pool Fires , and Soot Generation,” *SAE Tech. Pap.* (2001-01–1203), 2001, doi:10.4271/2001-01-1203.
  9. Chen, L., Braisher, M., Crossley, A., Stone, R., and Richardson, D., “The Influence of Ethanol Blends on Particulate Matter Emissions from Gasoline Direct Injection Engines,” *SAE Int.* (2010-01–0793), 2010.
  10. Westbrook, C.K., Pitz, W.J., and Curran, H.J., “Chemical kinetic modeling study of the effects of oxygenated hydrocarbons on soot emissions from diesel engines,” *J. Phys. Chem. A* 110(21):6912–6922, 2006, doi:10.1021/jp056362g.
  11. Fatouraie, M., Wooldridge, M., and Wooldridge, S., “In-Cylinder Particulate Matter and Spray Imaging of Ethanol / Gasoline Blends in a Direct Injection Spark Ignition Engine,” *SAE Int. J. Fuels Lubr.* 6(1), 2013, doi:10.4271/2013-01-0259.
  12. Singh, R., Burch, T., Lavoie, G., and Wooldridge, M., “Effects of Fuel Injection Events of Ethanol and Gasoline Blends on Boosted Direct-Injection Engine Performance Experimental Set-up,” *SAE Int. J. Fuels Lubr.*, 2017, doi:10.4271/2017-01-2238.Copyright.
  13. Arsuaga, L.G.G., “Advanced Diagnostics for Spray Behavior, Fuel Impingement, and Soot Processes in Direct Injection Spark Ignition Engines,” University of Michigan, 2019.
  14. Gawlica, T., Samenfink, W., Schünemann, E., and Koch, T., “Model-based optimization of multi-hole injector spray targeting for gasoline direct injection,” *Tagung Einspritzung und Kraftstoffe*, ISBN 1861346433: 271–289, 2019, doi:10.1007/978-3-658-23181-1\_14.
  15. Singh, R., Han, T., Fatouraie, M., Mansfield, A., Wooldridge, M., and Boehman, A., “Influence of fuel injection strategies on efficiency and particulate emissions of gasoline and ethanol blends in a turbocharged multi-cylinder direct injection engine,” *Int. J. Engine Res.* 1–13, 2019, doi:10.1177/1468087419838393.
  16. Knorsch, T., Rogler, P., Miller, M., and Wiese, W., “On the Evaluation Methods for Systematic Further Development of Direct-Injection Nozzles,” *SAE Tech. Pap.* 01, 2016, doi:10.4271/2016-01-2200.
  17. Medina, M., Alzahrani, F., Fatouraie, M., Wooldridge, M.S., and Sick, V., “Mechanisms

- of Fuel Injector Tip Wetting and Tip Drying Based on Experimental Measurements of Engine-Out Particulate Emissions from Gasoline Direct Injection Engines,” *Int. J. Engine Res.*, 2020.
18. Berndorfer, A., Breuer, S., Piock, W., and Bacho, P. Von, “Diffusion Combustion Phenomena in GDi Engines caused by Injection Process,” *SAE International*, 2013, doi:10.4271/2013-01-0261.
  19. Dageförde, H., Kiefer, A., Samenfink, W., Wiese, W., and Kufferath, A., “Requirements for Spray and Tip Design of a Multi-hole Injector for DISI Engines,” *ICLASS Conf.* 1–8, 2015.
  20. Leick, P., Schmitt, M., Kubis, T., Stapf, K.G., and Gawlica, T., “Impact of flash-boiling on gasoline sprays : From fundamental physical insights to engine-measured PN emissions,” *13th AVL Symposium*, 2018.
  21. Leick, P., Bork, B., and Geiler, J.N., “Experimental characterization of tip wetting in gasoline DI injectors,” *ICLASS Conf.* (July):1–9, 2018.
  22. Peterson, K., Grover, R., and Mitcham, C., “Application of optical diagnostics and simulation to fuel injector tip wetting and soot production,” *11th International Symposium on Combustion Diagnostics*, 2014.
  23. Eagle, E.W. and Musculus, M.P.B., “Cinema - Stereo Imaging of Fuel Dribble after the End of Injection in an Optical Heavy - Duty Diesel Engine,” *Thiesel*, 1–20, 2014.
  24. Karwa, N., Stephan, P., Wiese, W., and Lejsek, D., “Gasoline Direct Injection Engine Injector Tip Drying,” *19th Australasian Fluid Mechanics Conference*, ISBN 9780646596952: 5–8, 2014.
  25. Fischer, A. and Thelliez, M., “Methodology and Tools to Predict GDI Injector Tip Wetting as Predecessor of Tip Sooting,” *SAE Tech. Pap.* (2018-01–0286):1–10, 2018, doi:10.4271/2018-01-0286.
  26. Stanglmaier, R.H., Roberts, C.E., and Moses, C.A., “Vaporization of Individual Fuel Drops on a Heated Surface: A Study of Fuel-Wall Interactions within Direct-Injected Gasoline (DIG) Engines,” *SAE Tech. Pap. Ser.* 1(724), 2010, doi:10.4271/2002-01-0838.
  27. Wu, S., Yang, S., Wooldridge, M., and Xu, M., “Experimental study of the spray collapse process of multi-hole gasoline fuel injection at flash boiling conditions,” *Fuel* 242(January):109–123, 2019, doi:10.1016/j.fuel.2019.01.027.

28. Moulai, M., Grover, R., Parrish, S., and Schmidt, D., "Internal and Near-Nozzle Flow in a Multi-Hole Gasoline Injector Under Flashing and Non-Flashing Conditions," *SAE Tech. Pap. Ser. 1*, 2015, doi:10.4271/2015-01-0944.
29. Han, J.-S., Lai, M.-C., Henein, N.A., Wang, T.C., Xie, X.B., Miles, P.C., Harrington, D.L., and Pinson, J., "Dynamics of Multiple-Injection Fuel Sprays in a Small-bore HSDI Diesel Engine," *SAE Tech. Pap. Ser. 1(724)*, 2000, doi:10.4271/2000-01-1256.
30. Swantek, A.B., Duke, D.J., Tilocco, F.Z., Sovis, N., and Powell, C.F., "End of Injection, Mass Expulsion Behaviors in Single Hole Diesel Fuel Injectors," *ILASS Am. 26th Annu. Conf. Liq. At. Spray Syst.* (May), 2014.
31. Moon, S., Huang, W., Li, Z., and Wang, J., "End-of-injection fuel dribble of multi-hole diesel injector: Comprehensive investigation of phenomenon and discussion on control strategy," *Appl. Energy* 179, 2016, doi:10.1016/j.apenergy.2016.06.116.
32. Fatouraie, M., Peterson, K., Biddappa, B., Livshiz, N., Larimore, J., and Mosburger, M., "Advanced Gasoline Combustion and Engine Controls," *Reducing Particulate Emissions in Gasoline Engines*, SAE International, Warrendale: 103–114, 2018.
33. Eitel, F., Schäfer, J., Redante, E., Nolte, R., Königstein, A., and Heeger, C., "Potential and Challenges of Fuel Injection Pressure up to 50 MPa for Gasoline Direct Injection Engines," *26th Aachen Colloq. Automob. Engine Technol. 2017* (Di):489–508, 2017.
34. Moon, S., Li, T., Sato, K., and Yokohata, H., "Governing parameters and dynamics of turbulent spray atomization from modern GDI injectors," *Energy* 127, 2017, doi:10.1016/j.energy.2017.03.099.
35. Tu, P.-W., Weall, A., Jing, D., Venus, J.K., Dean, K., Srivastava, D.K., Xu, H., and Cao, L., "Numerical Investigation of GDI Injector Nozzle Geometry on Spray Characteristics," *SAE Tech. Pap. Ser. 1(3)*, 2015, doi:10.4271/2015-01-1906.
36. Bergstrand, P., "The Effects of Orifice Shape on Diesel Combustion," *SAE Technical Paper*, 2004, doi:10.4271/2004-01-2920.

## Chapter 5

### Conclusions and Future Outlook

#### 5.1 Conclusions

Fuel spray improvements offer benefits to efficiency and emissions in internal combustion engines. This dissertation provides new data and understanding for gasoline sprays at conditions relevant to both current and proposed advanced combustion strategies, including information on fundamental spray behavior and studies of particulate emissions that originate from nozzle wetting. Experiments were completed using several facilities: a constant volume chamber (CVC) at the University of Michigan; a high-temperature, high-pressure combustion chamber, a mass flow rate tester, and a momentum flux measurement facility at the Universitat Politècnica de Valencia, and three gasoline direct injection (GDI) engines and numerous fuel injectors at Bosch Group, LLC. The results represent quantitative and qualitative characterization of gasoline sprays providing insight into the physical mechanisms that govern fuel mixing and emissions. The data also provide direct measurements of spray development and inform fundamental theory and empirical models. Specifically, topics on high-pressure spray development of non-evaporating and evaporating sprays and effects of injector geometry and operating conditions on tip wetting were considered. The key conclusions from this dissertation include:

- The high-pressure gasoline spray development (quantified in terms of spray tip penetration distance, spray tip penetration rate, spray break-up time and spray angle) in non-evaporative conditions was a strong function of chamber pressure, and a weaker function of fuel injection pressure for all injector geometries tested. For example, spray angles differed by up to  $2^\circ$  for changes in chamber pressure, but were identical for changes in injection pressure. Unexpectedly (given the fuel properties of gasoline compared with diesel fuel), the high-pressure gasoline sprays demonstrated similar quantitative development for penetration distance as diesel sprays in regards to trends

with injection and chamber pressure. With regard to injector geometry, the nozzle with the smallest diameter consistently resulted in the lowest spray angle for all conditions tested, suggesting that the entrainment rates are lower and could lead to poor combustion. The diverging nozzle consistently produced the highest spray angle for all conditions tested, suggesting the opposite effect.

- Two unusual spray features were identified during the high-pressure gasoline fuel injection studies. The features were quantified with respect to the frequency of occurrence and the associated operating conditions. Specifically, vapor pre-jets were observed at the start of injection before the dense liquid spray exited the nozzle. The vapor pre-jets were observed with high frequency at the highest chamber pressures studied and no vapor pre-jets were observed at the lowest chamber pressures. The dependence on chamber pressure indicates the vapor pre-jet may be due to the injector ingesting chamber gases from the previous injection cycle. The vapor pre-jet may have implications on fuel mixing for strategies that use multiple injection events per cycle. Another irregular spray feature identified during the study was the occasional transient observation of asymmetric spray angle, described here as spray flutter. Spray flutter was quantified using the mean squared difference between the spray angle of an instantaneous fuel injection cycle with the cycle average. Highest spray flutter was observed for the diverging nozzle, and the lowest flutter was observed for a converging nozzle with inlet nozzle rounding. Spray flutter may be a good metric for identifying and quantifying the effects of cavitation in the nozzle.
- Rate of injection measurements showed injector geometry played a major role in injector performance with 20% mass flow rate increase for nozzles with hydroerosion rounding and conicity compared with the cylindrical nozzles studied. Momentum flux measurements indicated increasing outlet diameter (by a factor of about 1.25) increased momentum flux to a similar degree compared with rounded inlet nozzles. Momentum coefficients showed a negative trend with higher pressure differential (between the fuel injection pressure and the chamber pressure) for all injector geometries and conditions tested, which indicates some degree of cavitation was occurring with all nozzles although external spray development indicated few characteristics of cavitation.

- High-speed schlieren images at vaporizing conditions showed high-pressure gasoline spray development (e.g., spray penetration distance) was a strong function of chamber pressure. Generally, vapor phase penetration distance had the highest sensitivity to chamber pressure, followed by injection pressure, then chamber temperature, and injector coolant temperature had little to no effect in most cases. The effects of chamber pressure resulted in distinct groupings of the penetration distance data for all the densities tested. Penetration distance was also impacted by the different injector geometries. The largest cylindrical nozzle had the highest penetration distance and momentum flux at all conditions tested, and the smallest cylindrical nozzle had the lowest penetration distance and momentum flux. This trend suggests that fuel impingement (and therefore particulate emissions) could be higher for a cylindrical geometry large diameter nozzle during engine operation.
- For conditions where tip wetting was a significant source of engine-out particulate emissions, increasing fuel injection pressure, decreasing engine load (i.e., decreasing injection duration), increasing time scale, and increasing injector temperature correlated with decreased engine-out particulate number (PN). Similarly, certain changes in injector geometry such as decreasing hole length and divergent nozzle holes correlated with decreasing PN. Physical mechanisms were conceptualized to interpret the trends observed in PN in terms of mechanisms expected to be important for tip wetting and tip drying. Five mechanisms were proposed: *wide plume wetting*, *vortex droplet wetting*, *fuel dribble wetting*, *fuel condensation wetting*, and *single-phase evaporation*. The observed trends in the PN emissions were interpreted in terms of the different tip wetting and drying mechanisms. All the mechanisms were identified as sensitive to coolant/injector temperature, and the wide-plume wetting mechanism was conjectured to have the largest range of sensitivity to different engine operating parameters and fuel injector tip geometry.

The work presented here offers new insights on gasoline sprays and associated phenomenon that are difficult to capture with computational studies due to lack of fidelity and accuracy of many fuel spray models, particularly for high fuel injection pressures. Although the data presented here were tested for applications in internal combustion engines, the experimental

techniques can be used to inform other physical experiments and models for internal flow, and spray development, as well as expanded to other spray applications.

## 5.2 Future Work Recommendations

In this study, conceptual mechanisms were introduced to describe tip wetting/drying processes associated with fuel injectors. Alzahrani et al. [1] developed a theoretical model using first principles to predict tip drying rates. The model was shown to reasonably predict tip drying rates based on an assumed initial mass, injector temperature and other operating conditions. Although the model was demonstrated to predict tip-drying trends reasonably well, the tunable parameters to increase the drying rate are difficult to control with physical hardware. For example, one tunable parameter is the injector temperature, which is controlled (in part) indirectly in an engine by varying the amount of injector surface area exposed to the combustion gases. Coolant temperature can be controlled but is limited to temperatures below 90°C, and controlling fuel temperature is not considered practically feasible. A second model input parameter was residence time, which is predefined by engine speed and injection timing (which is set by the engine calibration to achieve optimum performance). Without a clear method to modify or control residence time or fuel temperature, the tip drying model can only predict evaporation for a fraction of the fuel film. A potential approach to mitigate tip wetting emissions is to develop a model to predict tip wetting using the four wetting mechanisms discussed in Chapter 4. The model would be useful from a design perspective and to interpret experimental results. Such a model would allow engine manufactures to predict total mass in tip wetting films and provide the means to develop strategies to reduce fuel film mass. Overall costs may be reduced as the need for expensive experiments and costly simulations can be reduced by improving the accuracy of the tip film model predictions. Even a semi-empirical model could decrease the number of experiments needed to quantify injector behavior and performance.

Experimental methods can help advance theory and test tip wetting sub models. Preliminary work showed some model parameters correlated well with engine-out PN. Particularly, injection pressure, engine load, and certain nozzle geometries tended to increase tip wetting PN. Next steps could investigate each wetting mechanism outside the context of an engine and determine the parameters that dictate fuel deposition and wetting rates. Parameters of interest include flash boiling conditions, other injector geometries, fuel properties, surface

roughness, and droplet sizes. Experiments of this nature would provide insight into wetting rates and provide a foundation of deeper understanding which could be used to improve injector design and reduce particulate emissions from tip wetting.

Applying data analytics such as model reduction techniques to the spray images is another area that can advance understanding how stochastic spray behavior may be impacting engine performance. Some methods include space-only proper orthogonal decomposition (POD), space-time POD, and dynamic mode decomposition (DMD). POD and DMD methods have been used to identify coherent fluid structures in fluid flows [2,3]. However, there is no consensus on which methods are more useful and how to interpret the data. The potential benefits to applying these techniques to sprays is the ability to model atomization and other phenomenon using simplified equations as well as quantifying cycle-to-cycle variability in the spray behavior [4,5]. While these techniques have been available for decades and are well implemented in other disciplines, the engine community has not explored the full potential of these methods, particularly in conjunction with data learning analytics. With the dramatic advances in time-resolved, non-intrusive spray measurements, and the ability to apply sophisticated mathematical analysis to the resulting images, there is significant opportunity to advance the understanding of spray physics and engine in-cylinder flows.

## References

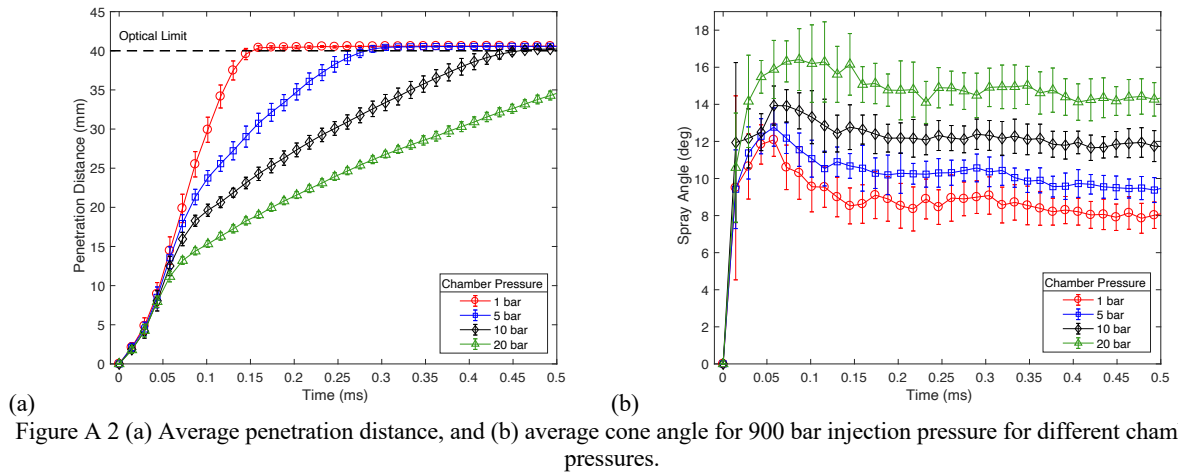
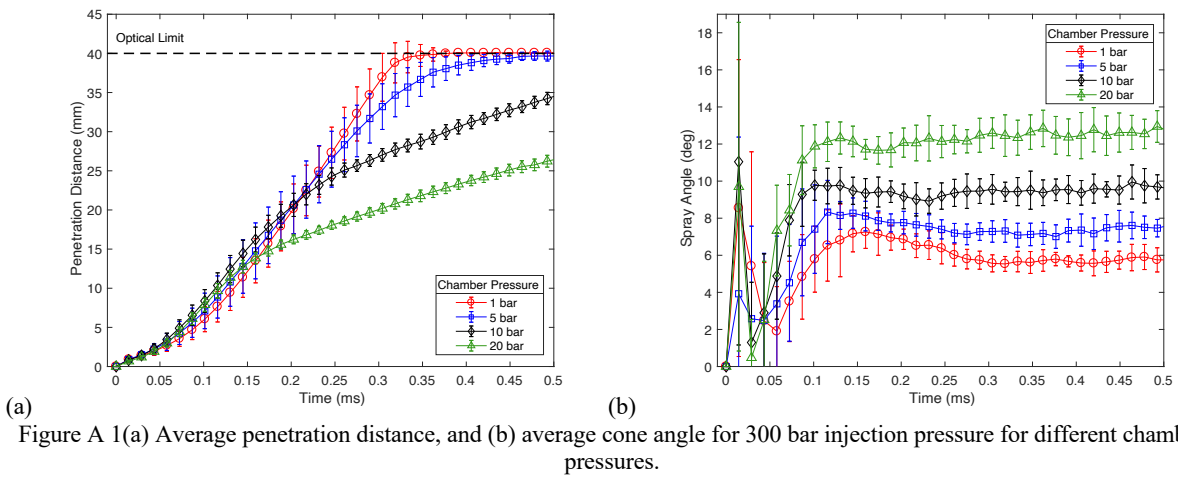
1. Alzahrani, F., “Theoretical and Experimental Study of Fuel Injector Tip Wetting as a Source of Particulate Emissions in Gasoline Direct-Injection Engines,” University of Michigan, 2020.
2. Towne, A., Schmidt, O.T., and Colonius, T., “Spectral proper orthogonal decomposition and its relationship to dynamic mode decomposition and resolvent analysis,” *J. Fluid Mech.* 847:821–867, 2018, doi:10.1017/jfm.2018.283.
3. Rowley, C.W., “Model reduction for fluids, using balanced proper orthogonal decomposition,” *Int. J. Bifurcat. Chaos* 15(3):997–1013, 2005, doi:10.1142/S0218127405012429.
4. Bizon, K., Continillo, G., Mancaruso, E., Merola, S.S., and Vaglieco, B.M., “POD-based analysis of combustion images in optically accessible engines,” *Combust. Flame* 157(4):632–640, 2010, doi:10.1016/j.combustflame.2009.12.013.

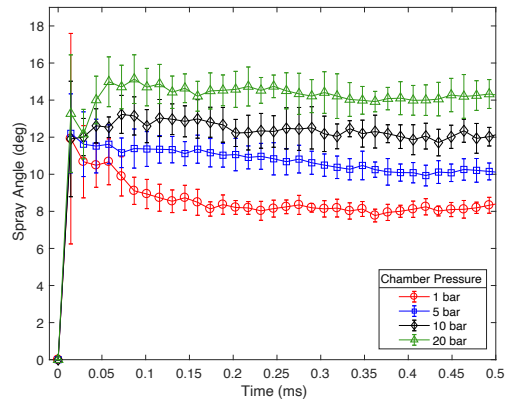
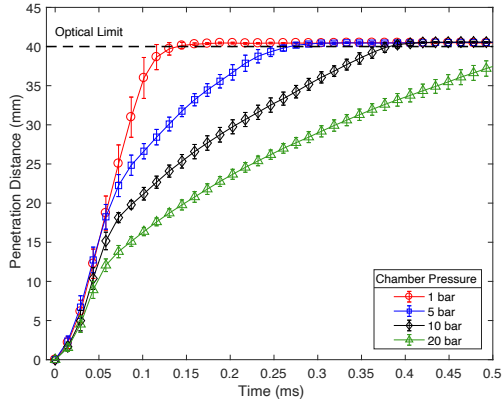


5. Chen, H., Hung, D.L.S., Xu, M., and Zhong, J., “Analyzing the Cycle-To-Cycle Variations of Pulsing Spray Characteristics By Means of the Proper Orthogonal Decomposition,” *At. Sprays* 23(7):623–641, 2013, doi:10.1615/AtomizSpr.2013007851.

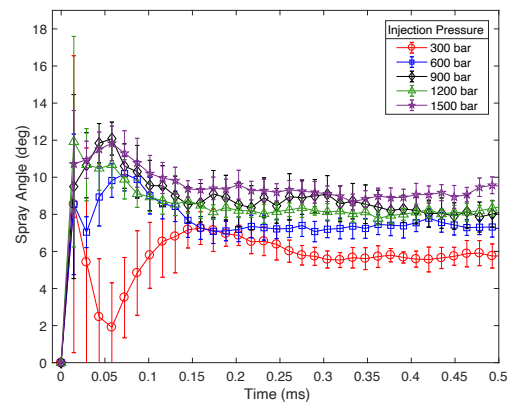
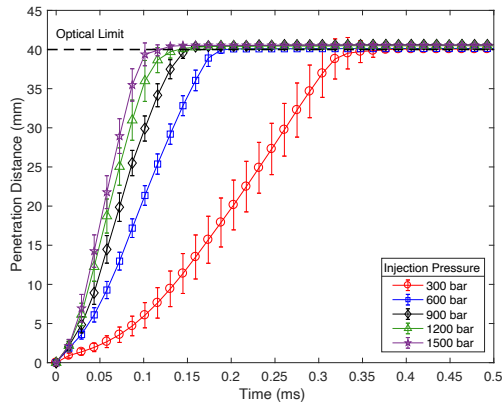
## Appendix 1

### Supplemental Material for Non-evaporative Study of High-pressure Sprays

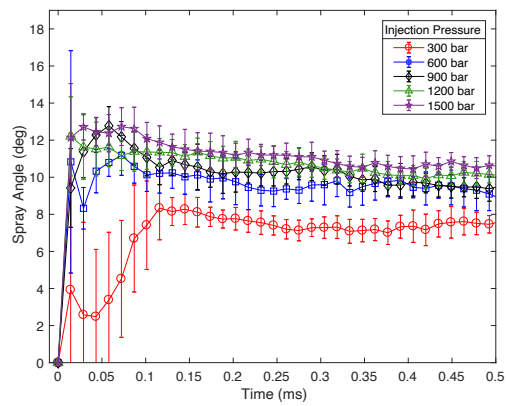
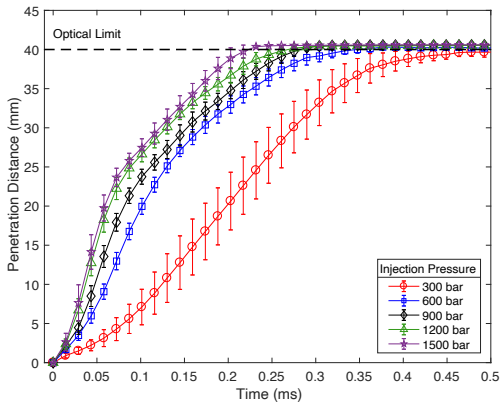




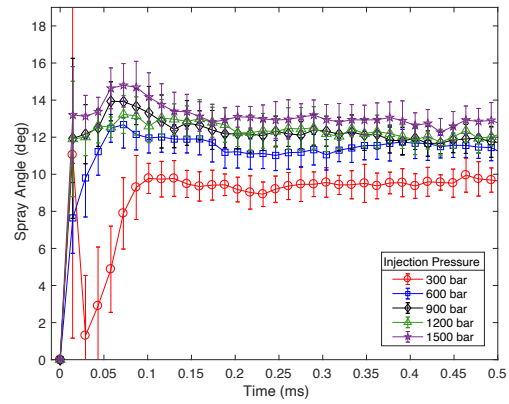
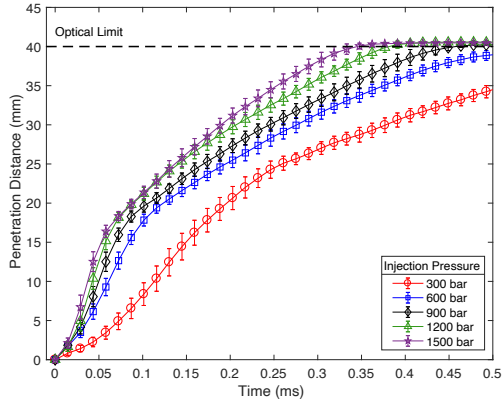
(a) Figure A 3 (a) Average penetration distance, and (b) average cone angle for 1200 bar injection pressure for different chamber pressures.



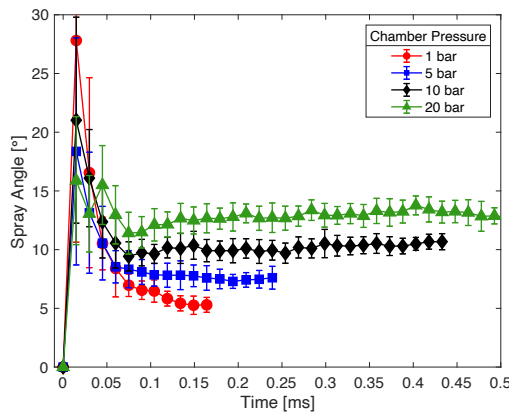
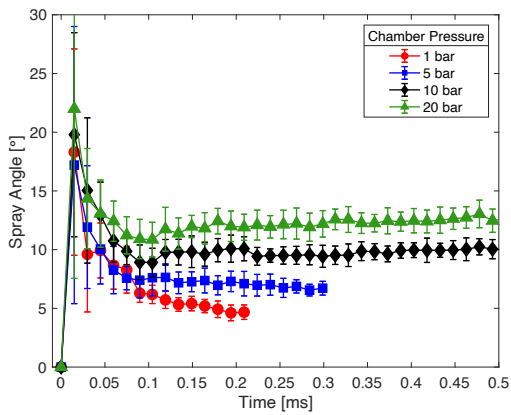
(a) Figure A 4 (a) Average penetration distance, and (b) average cone angle for 1 bar chamber pressure for different fuel injection pressures.



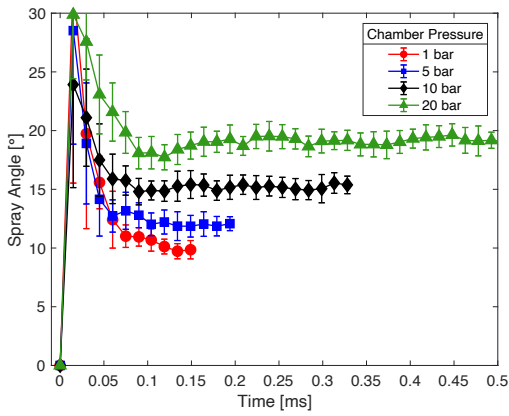
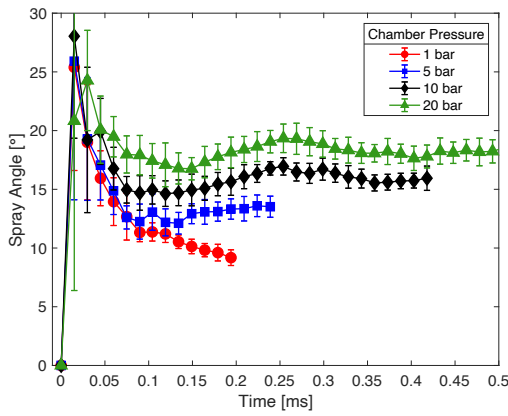
(a) Figure A 5 (a) Average penetration distance, and (b) average cone angle for 5 bar chamber pressure for different fuel injection pressures.



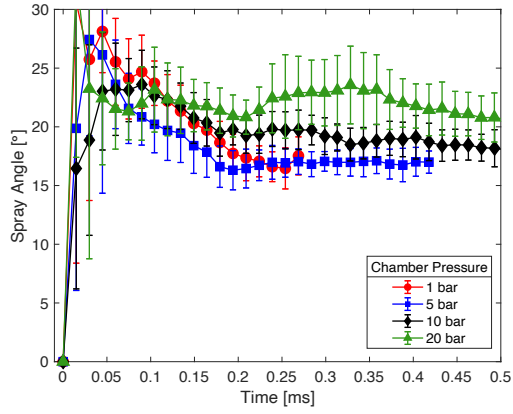
(a) (b)  
 Figure A 6 (a) Average penetration distance, and (b) average cone angle for 10 bar chamber pressure for different fuel injection pressures.



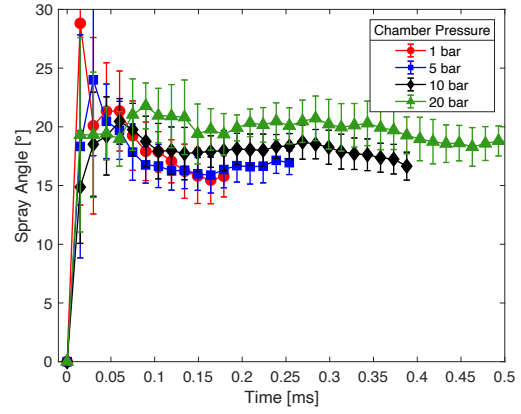
(a) (b)  
 Figure A 7. Average spray angle for Injector B hole 1 for fixed injection pressure of (a) 600 bar and (b) 900 bar



(a) (b)  
 Figure A 8. Average spray angle for Injector B hole 2 for fixed injection pressure of (a) 600 bar and (b) 900 bar

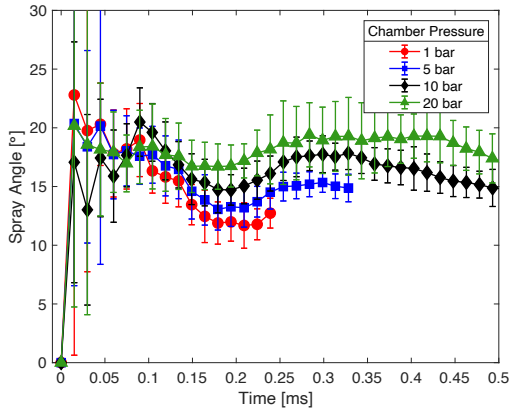


(a)

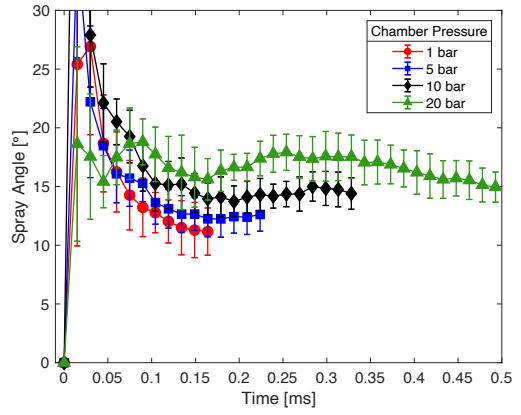


(b)

Figure A 9. Average spray angle for Injector C hole 1 for fixed injection pressure of (a) 600 bar and (b) 900 bar



(a)



(b)

Figure A 10. Average spray angle for Injector C hole 2 for fixed injection pressure of (a) 600 bar and (b) 900 bar

## Appendix 2

### Supplemental Material for Particulate Emissions Study

Sample results of the 2000 RPM and 3000 RPM data for engine-out PN as a function of drying time are shown in this appendix for engine loads 2 bar, 6 bar, 10 bar, 14 bar and 18 bar BMEP. For each load, plots are shown for Injectors I, J, A, B, and C (left to right) respectively.

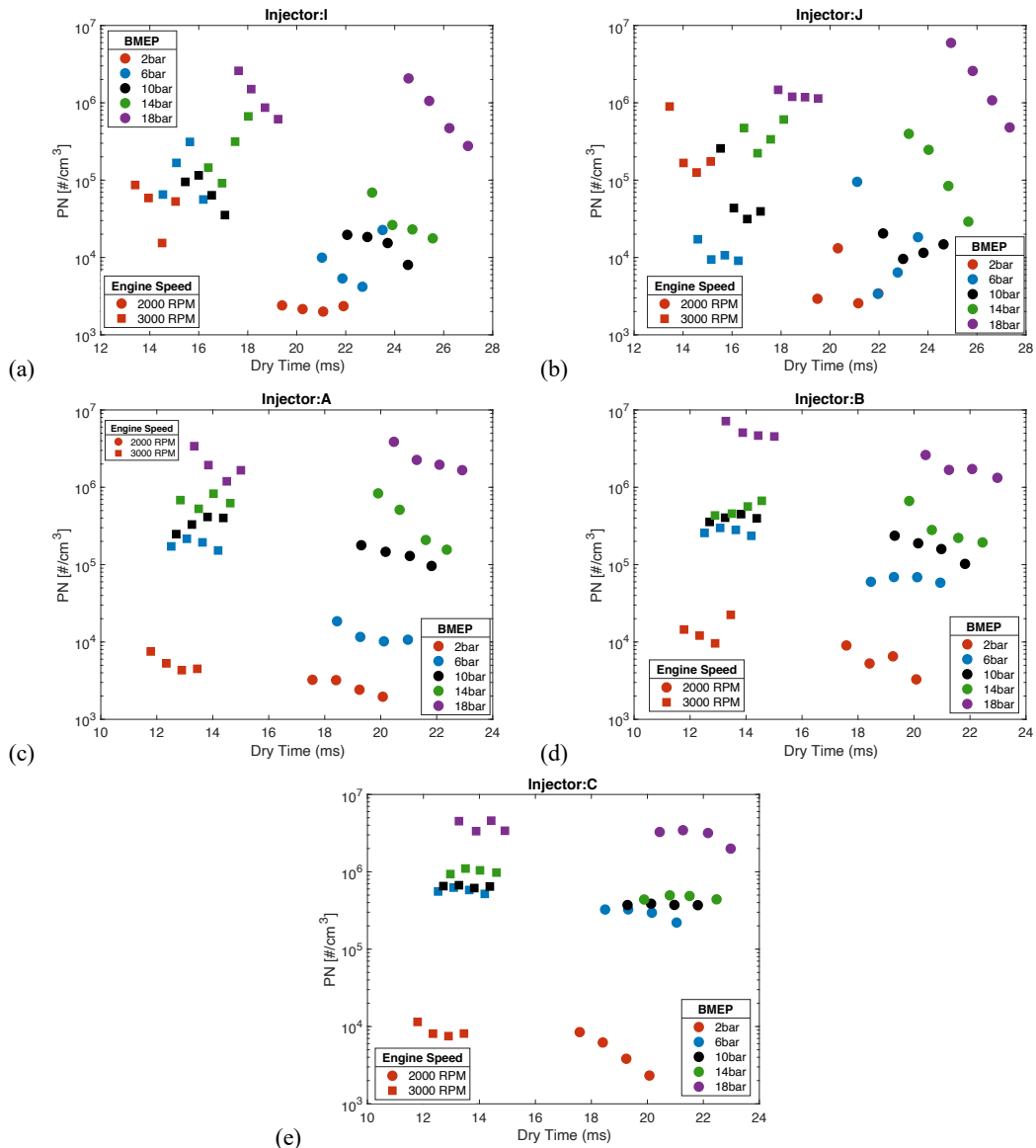


Figure A 11. Effect of engine speed and SOI timing on PN emission for Engine 1 for fixed  $T_c = 90\text{ }^\circ\text{C}$  and  $p_f = 200\text{ bar}$  and five load conditions for (a) Injector I, (b) Injector J, (c) Injector A, (d) Injector B and (e) Injector C. Time is the absolute time from the end of injection to the time of spark. So, for fixed injection duration and spark timing, shorter times correspond to later SOI and longer times correspond to earlier SOI

For lower coolant temperature, the effects for fuel injection pressure were similar to the results presented in Figure 4.12. Increasing injection pressure lowered PN at all engine speeds. The results for the effects of injection pressure and engine load on PN for lower coolant temperature are provided here.

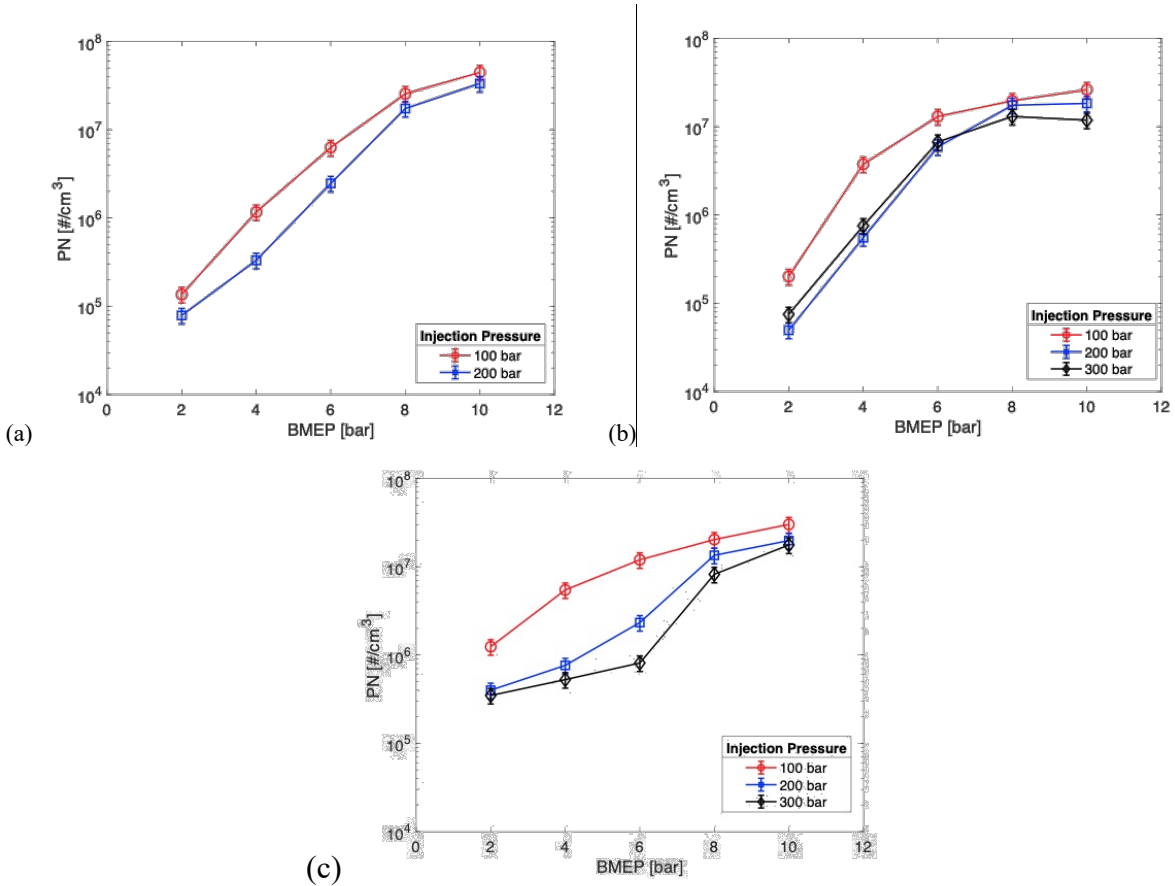


Figure A 12 Injection pressure effects on PN for Injector L, Engine 2, coolant temperature of  $40\text{ }^\circ\text{C}$ , and engine speed of (a) 1000 RPM (b) 2000 RPM and (c) 3000 RPM. PN results are for a fixed SOI in the tip wetting dominant regime of 260 CAD bTDC